

Muon Analysis with the AMANDA-B Four-String Detector

Thesis submitted for the degree of
Doctor of Philosophy in Physics
by

Adam Bouchta



Doctoral Dissertation 1998
Fysikum
Stockholm University
Vanadisvägen 9
S - 113 85 Stockholm

Abstract

The AMANDA neutrino telescope consists of an array of photomultiplier tubes buried deep in the South Pole glacier ice. The ice acts as a Cherenkov medium for muons produced by neutrino interactions with the matter in and around the detector. Mapping of the Cherenkov cone using hit time information makes it possible to achieve precise track reconstruction. Calibration results are presented and the optical properties of the ice are reviewed.

A track reconstruction program was developed to analyze data taken during 1996 and its performance assessed with Monte Carlo simulations. Coincidence events taken with the SPASE-2 extensive air-shower array were also reconstructed, yielding results confirming the SPASE analysis.

A search for atmospheric neutrinos using six months of live data was performed and the first two up-going candidate events are presented. This analysis allowed to set limits on the neutrino-induced muon flux from neutralino annihilation in the center of the Earth. Upper limits at the 90% confidence level on the resulting muon flux were calculated, yielding $1.8 \cdot 10^{-14} - 10^{-13} \text{cm}^{-2}\text{s}^{-1}$ for neutralino masses $150 \text{ GeV}/c^2 < m_\chi < 500 \text{ GeV}/c^2$.

The systematic error on the limits is shown to come mainly from the current uncertainty in the time calibration.

Contents

1	Dissertation description	1
2	Introduction	1
3	Neutrino astrophysics	3
3.1	Physics background	3
3.1.1	Neutrino production	3
3.1.2	Acceleration mechanisms	5
3.1.3	Candidate point sources of neutrinos	7
3.1.4	Neutrino cascades	9
3.1.5	Neutralino annihilation	10
3.1.6	Background	11
3.2	Muon neutrino detection	11
4	Detector description	21
4.1	String description	21
4.2	Deployment	23
4.3	Optical modules	26
4.4	Electronics and DAQ	29
5	Optical properties of the South Polar ice	37
5.1	Diffusive scattering in AMANDA-A	37
5.2	The ice at AMANDA-B depths	40
6	Calibration	44
6.1	Time calibration	44
6.2	Position calibration	46
6.2.1	Laser positioning	46
6.2.2	Drill positioning	55
6.2.3	Conclusions	57
7	Data filters	63
7.1	Data cleaning	63
7.2	Pre-filtering of events	66
8	Reconstruction of muons-tracks	69
8.1	Introduction	69
8.2	Time probability distribution functions	72
8.3	Reconstruction method	79
9	Analysis of 1996 data	87
9.1	Description of the data sample	87
9.2	Atmospheric muons	88
9.2.1	The atmospheric muon spectrum	88
9.2.2	SPASE coincidences	95
9.3	Search for atmospheric neutrinos	99

9.4 Search for neutralinos from the center of the Earth	104
10 Conclusions	111
Acknowledgments	112
References	113
Appendix	117

1 Dissertation description

This dissertation describes the work done between the summer of 1993 and the summer of 1997. It includes:

- a summary of the physics goals of AMANDA.
- a description of the hardware used in the detector.
- a summary of our present knowledge about the optical properties of the glacier ice at the South Pole.
- results of the position and time calibration of the AMANDA-B array.
- a description of the data preparation prior to reconstruction.
- a description of the muon-track reconstruction methods used and a discussion upon the detector response to different classes of events.
- studies of atmospheric muon coincidences between SPASE-2 and AMANDA-B.
- a search for up-going atmospheric neutrinos.
- the results of a search for muons induced by neutralino annihilation from the center of the Earth, resulting in a limit on the expected flux.

My main activities in the AMANDA collaboration were the development of the Swedish event reconstruction program STREC. I have also worked with the position calibration of the four-string array, especially using laser data, with the data-handling and with the analysis of the AMANDA-SPASE events. I also applied the reconstruction program in the search for atmospheric neutrinos, using the whole 1996 data sample. This served as a basis for the neutralino analysis, resulting in limits set on the neutrino-induced muon flux coming from neutralino annihilation in the center of the Earth.

2 Introduction

AMANDA is a European-American collaboration to build a neutrino telescope located at the geographical South Pole, a project started in 1992. Such a telescope will open a new observation window on the Universe, complementary to the electromagnetic observations already in use. Its basic principle is to detect the Cherenkov wavefront emitted by muons passing through a clear medium, which are produced when highly energetic neutrinos (greater than a few GeV) interact with matter in a region close to the detector. This light is detected by an array of photo-multipliers (PMs) buried in deep glacier ice. The time distribution of hits then provides the necessary information for reconstructing the straight-line track of the muon. One can infer the direction of incoming neutrinos from the direction of their muon tracks since the two are parallel within about one degree at about 1 TeV (and improving with energy). Thus the telescope is able to search for point sources of neutrinos with an angular resolution of order one degree or better. The general aim is to observe high energy cosmic neutrinos from different possible sources such as Active Galactic Nuclei (AGNs), X-ray binary systems, young supernova remnants, Gamma Ray Bursters (GRBs) and neutralino annihilation in the center of our Sun and Earth.

An important background to these events are atmospheric muons produced by cosmic rays interacting in the atmosphere. As a result, the telescope has to be buried deeply, so that the overburden of ice reduces the rate of downward muons to manageable levels. Atmospheric muons cannot traverse the Earth and so they do not produce a background of upward muons. The telescope is then designed to search for upward (or near-horizontal) muons and must be able to reject the background of downward muons by a factor of order (10^6) which depends on the detector's depth and the optical properties of the surrounding ice. Atmospheric neutrinos produce an irreducible and isotropic background of upward muons. Fortunately, the energy spectrum of these neutrinos falls off much more steeply than the anticipated neutrino spectra of the above cosmic sources, and thus the atmospheric background should be low (relative to the source) above an energy of 1- 10 TeV, which depends on the source.

A three-dimensional array of optical modules (OMs) has already been successfully deployed in several stages during the past few years, at depths between 800 and 2400 meters. An OM consists of a large (20 cm in diameter) PM housed in a glass sphere and linked to the data-taking surface electronics and power supply by a long cable. At this stage, 13 strings supporting between 20 and 42 OMs each have been deployed and are taking data. The first stage (AMANDA-A) was the deployment in 1993-94 of four strings between ~ 800 – 1000 m, where the air bubble density yielded a short scattering length of the Cherenkov light, but increasing with depth. It was followed by the deployment of four more strings at ~ 1500 – 2000 m in 1995-96 (AMANDA-B4), assessing the better optical qualities of the ice at those depths. The size of this array was increased by the addition of six strings in 1996-97 (AMANDA-B10) and three more strings in 1997-98 (AMANDA-B13), reaching down to 2400 m. This thesis will mainly concentrate on AMANDA-B4.

AMANDA-B is operated in coincidence with the previously deployed detector at shallower depth, AMANDA-A, and also with an extensive air shower detector, SPASE. This provides AMANDA with a unique opportunity to compare analysis results with those from a different experiment. A Monte Carlo simulation program, LOLITA [1], has been developed at Stockholm University, to simulate the propagation of muons in ice and the detector response to their Cherenkov light. It has been used both in the development of the analysis tools and to verify results yielded by the data analysis presented here.

Other detectors The pioneer project in this field was DUMAND [2, 3], which planned the deployment of an undersea array at 4.8 km depth outside Hawaii. A lot of their I+D and experience has been used in the design and construction of the present generation of neutrino telescopes. The project has recently been terminated.

Among other similar projects already taking data is BAIKAL [4]. It consists of 6 strings with 144 OMs installed in Lake Baikal at about 1100 m depth. A plan for an extension to 200 OMs is underway. Baikal has demonstrated the feasibility of doing neutrino astronomy with an array of OMs and the capability of reconstructing up and down going muons. In order to suppress a background rate of tens of kHz, they pair optical modules and use only coincidences, lowering the background to a few hundred Hz. With their present array they should identify 1-2 events/week.

Currently under heavy I+D is ANTARES [5]. Their plans are to deploy an array deep in the Mediterranean, connected to the shore by an electro-optical cable. They are presently building a 'demonstrator', a single string to study the feasibility of such a detector in the sea. Site studies and the characterization of the optical properties of deep sea water have been started in the Mediterranean.

NESTOR [6] is planned to be installed at 3.8 km depth in the Mediterranean. The mechanical

structure of NESTOR is a 12 floor tower, each floor composed of a titanium star supporting a hexagonal array of OMs at the ends. The electronics is housed in a central titanium sphere on each floor. The digitized OM signals are transmitted to shore via a 12 fibre electro-optical cable. Since 1989, many tests have been performed. The first tower is expected in the near future.

3 Neutrino astrophysics

3.1 Physics background

3.1.1 Neutrino production

High energy cosmic neutrinos are produced in the interaction of cosmic rays with target matter which can be located close to the source of acceleration (companion of a pulsar in a X-ray binary), on their way towards the observer (interstellar medium) or at the observation point (Earth's atmosphere). In all cases, the mechanism is reminiscent of a beam dump experiment.

Neutrino production occurs when pions, produced in collisions between cosmic rays and the target matter, decay according to [7]:

$$N + A \rightarrow \pi^\pm + X \quad (1)$$

$$\begin{array}{l} \longleftarrow \mu^\pm + \nu_\mu(\bar{\nu}_\mu) \\ \longleftarrow e^\pm + \nu_e(\bar{\nu}_e) + \bar{\nu}_\mu(\nu_\mu) \end{array}$$

and a similar decay chain describes the production of neutrinos from kaons. In this latter case, however, about 38.7% of the K_L^0 kaons decay through the K_{e3}^0 channel [8]:

$$K_L^0 \rightarrow \pi^\pm + e^\mp + \bar{\nu}_e(\nu_e) \quad (2)$$

and 27% decay through the $K_{\mu 3}^0$ channel:

$$K_L^0 \rightarrow \pi^\pm + \mu^\mp + \bar{\nu}_\mu(\nu_\mu) \quad (3)$$

For kinematical reasons, all neutrinos in Eq. 1 have roughly the same energy. Thus, assuming that all particles (pions, kaons and muons) decay before they can interact with matter, the following ratios can be deduced from Eq. 1 [7]:

- $\nu_e(\bar{\nu}_e)/\nu_\mu(\bar{\nu}_\mu) \approx 1/2$
- $\nu_\mu/\bar{\nu}_\mu \approx 1$
- $\nu_e/\bar{\nu}_e \approx \mu^+/\mu^-$

The assumption is valid for astrophysical targets with low densities compared to the decay length of the muon, but not for the denser atmosphere of Earth. In that case, high energy muons of more than ~ 2.5 GeV will interact with air molecules high up in the atmosphere before they can decay to $e \nu_e \nu_\mu$, leading to a decrease in the ν_e/ν_μ ratio observed at sea level [7]. The main contribution of atmospheric $\nu_e(\bar{\nu}_e)$ with energies greater than a few GeV will thus come from the K_{e3}^0 channel (Eq. 2) [7].

At yet higher energies (greater than $5 \cdot 10^4$ GeV for ν_e and greater than 10^6 GeV for ν_μ [9, 10, 11]) atmospheric neutrinos are produced mainly as prompt decay products of charmed particles with very short life times.

For primaries in the lower part of the cosmic ray energy spectrum, yielding leptons of a few GeV at most, a ratio value of 1/2 is expected for ν_e/ν_μ . However, this is not reflected in measurements made by some experiments – the so-called ‘atmospheric anomaly’ [7]. Measurements made by IMB [12], SOUDAN2 [13] and Kamiokande [14] yielded a value closer to 1, whereas NUSEX [15] and Frejus [16] get results more in agreement with the predicted ratio of 1/2 [10].

When E_μ is greater than several GeV and ν_μ production from muon decay can be neglected, the muon neutrino spectrum via pion and kaon decay is approximately given by [7]:

$$\frac{dN_\nu}{dE_\nu} = \frac{N_0(E_\nu)}{1 - Z_{NN}} \left(\frac{A_{\pi\nu}}{1 + B_{\pi\nu} \cos\theta E_\nu/\epsilon_\pi} + 0.635 \frac{A_{K\nu}}{1 + B_{K\nu} \cos\theta E_\nu/\epsilon_K} \right) \quad (4)$$

where $A_{\pi\nu} = Z_{N\pi}(1 - r_\pi)^\gamma/(\gamma + 1)$, $r_\pi = (m_\mu/m_\pi)^2$ and $B_{\pi\nu}$ is a constant that depends on the spectral index γ and on nucleon and pion attenuation lengths. The first term inside the parentheses represents neutrinos from the decay of pions. At energies $E_\nu < \epsilon_\pi$, all the pions decay and the neutrino spectrum from pions follows the primary cosmic ray spectrum $\propto E^{-2.7}$, whereas at higher energies, pions can interact before decaying and the spectrum steepens to $\propto E^{-3.7}$. For cascade development in the Earth’s atmosphere $\epsilon_\pi \approx 115$ GeV.

Similar considerations apply for kaons, but since $\epsilon_K \approx 850$ GeV, kaon induced neutrinos will dominate over pion induced ones at high energies. Further terms can be added to Eq. 4 for charmed particles (see [10]) which, due to their high critical energy, will dominate for E_ν greater than 100 TeV.

Since the contribution from muon decay to the production of atmospheric electron-(anti)neutrinos is inhibited by muon interaction, they have an energy spectrum steeper by one power (with a maximum around 30-40 MeV).

The declination distribution of neutrinos is given by Eq. 4, i.e. is fundamentally $\propto \sec\theta$. For low energies however, the flux is strongly suppressed towards the horizon, since the slant depth then becomes large and interactions of parent particles are more likely [11].

As for cosmic neutrinos, they can be produced with the spectral index of the source if produced there, or with that of the diffusive cosmic ray spectrum if produced by particle collision with ISM (interstellar matter). They will retain their original spectrum in both cases, if we suppose that the matter densities they travel through are low.

Atmospheric neutrinos have an energy distribution suppressed at energies high enough for their parent particles to interact with the atmosphere. Thus, sources of cosmic neutrinos should be detectable above the atmospheric background, given that their flux is large enough.

Cosmic rays interacting with ISM will produce a flux of neutrinos which can be estimated to be 10^{-5} of the cosmic-ray flux in the PeV range [10]. It would be a diffuse flux, but originating mainly from regions with higher matter densities such as the spiral arms of our galaxy and molecular clouds and thus concentrated to the galactic plane (yielding some 5 events/year above 10 TeV in a 10^5m^2 detector, well below the atmospheric neutrino background [10]). Another source is the Sun which has a critical energy $\epsilon_\pi \sim 2$ TeV, i.e. much higher than in the Earth’s atmosphere, and is more efficient at neutrino production. However, due to the limited angular size of the Sun, the predicted rates are very low (less than 2 events/year above 10 GeV in a 10^5m^2 detector [10]).

3.1.2 Acceleration mechanisms

In production sources with relatively low matter-densities, the amount of neutrinos produced as a result of cosmic rays collisions is proportional to the CR-flux even up to high energies. Thus, measurements of galactic cosmic rays are important for predicting the neutrino flux.

Observations at hand give that the energy spectrum of primary cosmic rays follows a power law:

$$\frac{dN}{dE} \propto E^{-(\gamma+1)} \quad (5)$$

where the spectral index $\gamma = 1.7$ up to ~ 100 TeV a region called the *knee* after which the spectrum steepens to $\gamma = 2$. That kink might reflect the inability of our galaxy to retain very high energy protons. Above 10^6 TeV (the region of the *ankle*), the spectral index decreases again.

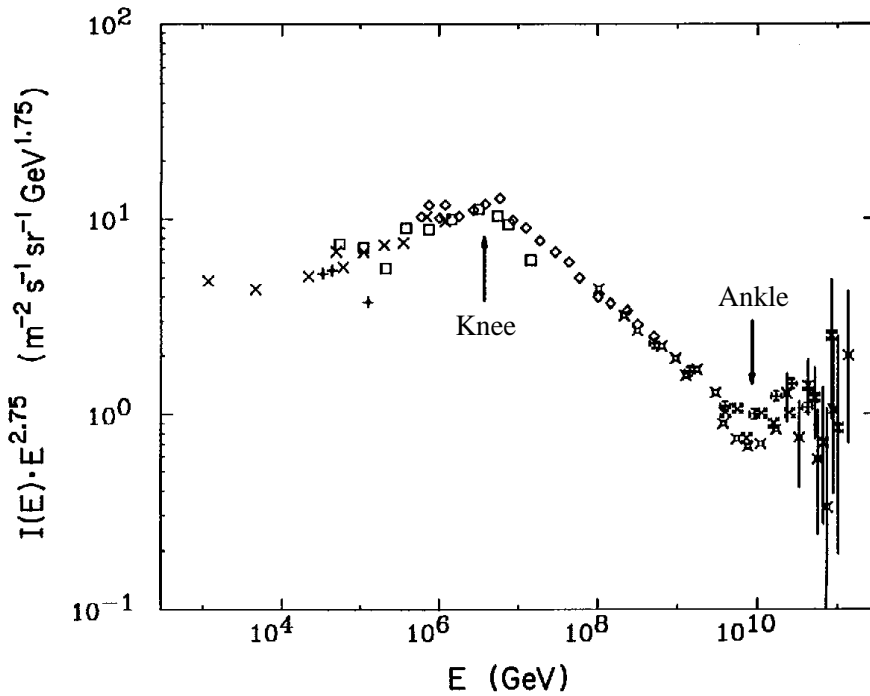


Figure 1: Cosmic ray energy spectrum

Direct measurements of the spectrum have been made up to energies of ~ 10 TeV with satellites or balloon borne apparatus and verified from secondary cosmic ray spectra. The range has been extended up to ~ 100 TeV, using single muon spectra at sea level. Air shower data have explored the spectrum from ~ 2 TeV. The Fermi mechanism [7] provides a convincing explanation for cosmic ray acceleration, leading to a power law spectrum. Fermi acceleration can also explain how protons of ~ 100 GeV are observed in solar flare eruptions, although nuclear processes in the Sun can at most produce particle energies of ~ 10 MeV.

The basic process behind this mechanism is that particles gain a fraction f more energy in a process of multiple encounters:

$$E = E_0 \cdot (1 + f) \quad (6)$$

Thus the number of collisions to reach energy E is

$$N = \ln(E/E_0)/\ln(1 + f) \quad (7)$$

The probability of a particle remaining in the acceleration region for N encounters is $P_N = (1 - P_{esc})^N$. Here P_{esc} is the probability of escape per interaction, given approximately by $P_{esc} \approx T_{acc}/T_{esc}$, where T_{acc} is the mean time between accelerating encounters, and T_{esc} is the mean time for escape from the accelerating region. Therefore the fraction of particles with energy greater than E_N is given by $F(> E) \approx \sum_{i=N}^{\infty} (1 - P_{esc})^i = (1 - P_{esc})^N / P_{esc}$, i.e., using Eq. 7:

$$F(> E) \approx \frac{1}{P_{esc}} \left(\frac{E}{E_0} \right)^{-\gamma} \quad (8)$$

where $\gamma = \ln(1/1 - P_{esc})/\ln(1 + f) \approx P_{esc}/f = T_{acc}/T_{esc} \cdot 1/f$, reproducing the expected form of the probability distribution. Replacing the number of encounters N in Eq. 6 by the total time spent divided by T_{acc} we get $E < E_0 \cdot (1 + f)^{t/T_{acc}}$, from which we can draw two conclusions: firstly, that the maximum energy that can be reached is depending on the lifetime of the accelerator and secondly, that particles with high energies take longer time to get accelerated than those with low energies.

Charged particles can gain energy in the stochastic way sketched above when encountering localized magnetic fields carried by blobs of interstellar plasma. Yet another possibility is encounters with a steadily moving plane shock front. In the first case, called second order mechanism, the particle can be accelerated in any direction at each encounter. The designation 'first order Fermi mechanism' applies for the second case, where the particle gets sent out away from the shock at each encounter. First order acceleration is the more efficient, yielding a gain per encounter $\approx 4/3\beta$, whereas second order yields $f \approx 4/3\beta^2$, where β is the speed of the shock front the cloud, respectively.

A value of $\gamma = 1 + \epsilon$, where ϵ is a small number, is reached in the case of first order acceleration by a strong shock of monoatomic gas, smaller than the value of 1.7 given by spectral index measurements. Note however that this value is not taking propagation into account and is thus valid for the spectrum at the source. An improvement can be made by modelling our galaxy as a leaky box from which cosmic rays eventually escape by diffusion and using measurements of relative abundances of spallation products. A characteristic escape time $\tau(E) \propto E^{-\delta}$ can then be derived, with $\delta \approx 0.6$ (see [7]) for energies less than 100 TeV. The energy spectrum then becomes $\propto E^{-(2+0.6+\epsilon)}$, consistent with observations.

Plausible candidates for particle acceleration up to energies of 100 TeV are supernovae. It can be shown (see [7]) that first order Fermi acceleration by the shocked gas of a supernova shell can at most yield an energy $E_{max} \leq \frac{3}{20} \frac{u^2}{c} Z e B T$ where the factor $3/20$ depends on the diffusion model, u is the shock front velocity and T is the lifetime of the shock ~ 1000 years. This gives a maximum energy compatible with 100 TeV but does leave open the question about how the more energetic particles are accelerated.

3.1.3 Candidate point sources of neutrinos

Young supernovae remnants (YSN)

Energy for the acceleration of particles inside the shell of a young supernova could be provided by its rotational energy. A pulsar would lose energy as magnetic dipole radiation, driving a wind of electrons which would create a shock front inside the shell, on which particles can be accelerated by first order Fermi mechanism, reaching energies up to 10^5 TeV [7]. The power released is localized in a region close to the pulsar and can be estimated by

$$L = 4 \cdot 10^{43} B^2 P^{-4} \text{ erg/s} \quad (9)$$

where B is the surface magnetic field strength in 10^{12} G and P its period in ms. With $P = 10$ ms and $B = 10^{12}$ G and 25% efficiency for particle acceleration, we get $L = 10^{39}$ erg/s.

A supernova distant by 10 kpc would produce ~ 100 neutrino induced muons per year in a 10^5 m² detector, but the acceleration process of protons goes over fast, typically within a few years, making the number of interesting objects very rare [10]. Another source of acceleration than the pulsar wind could be accretion of matter from the inside of the shell to the neutron star. Photons with energies of one TeV coming from the Crab Nebula have been observed [17] with the Whipple Cherenkov detector. The Crab Nebula is a young supernova remnant, with a pulsar (PSR 0531) near its center. The only recently observed supernova explosion, SN-1987A at 50 kpc, has not yet yielded a convincing signal of TeV photons or neutrinos [10].

X-ray binaries

The accretion of matter from a massive non-compact companion by a neutron star accompanied by X-ray release could provide the means of acceleration of cosmic rays. The luminosity of such an object is limited by the infalling flow of matter (the Eddington limit):

$$L_{Edd} = 4\pi GMm_p/\sigma_T \text{ erg/s} \quad (10)$$

where M is the mass of the neutron star, m_p the proton mass and σ_T the Thomson cross-section.

Another possible mechanism that could occur would be the interaction with shock-front creation of a pulsar wind with the atmosphere or the wind of its companion.

Active Galaxy Nuclei (AGN)

Active galactic nuclei are a generic name for a range of objects with different properties. A common feature for them all is that they are the most luminous objects in the Universe and that half their luminous output is concentrated in their central region, within a volume the size of the solar system. That small size supports the idea that the energy output comes from accretion of matter on a massive black hole. In much the same way as for X-rays binaries, but on larger scales, a shock front is formed on which first order Fermi acceleration of protons can occur. A prominent feature is a UV-bump with a mean photon energy of 40 eV consistent with thermal emission from an accretion disk [18].

About 10% of all AGN are classified as *radio-loud* compared to the rest. One possible reason for this difference is that they are observed from a small angle relative to their jets, from which a large fraction of the luminosity is emitted.

Along with pp collisions in the infalling gas, producing π^\pm according to Eq. 1, photoproduction of pions can take place in the optically thick photon field around the core according to:

$$p + \gamma \rightarrow n + \pi^+ \quad (11)$$

$$p + \gamma \rightarrow p + \pi^0$$

followed by neutrino production from π^+ decay. If the photon density is very high relative to the proton density, these processes will dominate over pp collisions. Also, if the radiation is strong enough in the disk, all photons will lose energy in $\gamma + \gamma \rightarrow e^+ + e^-$ interactions and all electrons and photons cascade down to energies around 100 GeV by inverse Compton scattering and pair production [19]. Neutrons with energies high enough from Eq. 11 can also produce mesons via interactions with photons: $n + \gamma \rightarrow p + \pi^-$, contributing further down to neutrino (both ν_μ and ν_e) production.

Proton energy loss by interaction with photons (Eq. 11) starts at a threshold γ -energy $\epsilon \approx (m_\Delta^2 - m_p^2)/(2E_p)$ which yields a proton energy of $\sim 10^7$ TeV for the UV bump [18]. The lack of strong X-ray absorption [18] could indicate that the energy loss by $p + p$ reactions is smaller, due to a lower proton density compared to photons. Energy loss by pair production $p + \gamma \rightarrow p + e^+ + e^-$ is also small, because of the low mass of the electron. It is however the dominant process at proton energies between 30-3000 TeV [10]. Below a certain energy, the proton interaction length with photons is larger than the radius of the optically thick region and they can escape. Thus, neutrinos are expected to follow the proton energy spectrum down to that energy, estimated to $\sim 5 \cdot 10^5$ GeV [10].

Several AGN have been reported to emit GeV photons with a variability of the order of days (flares), all of them radio-loud. Markarian 421 has even been observed to emit TeV photons [21]. These high photon energies could be explained by inverse Compton scattering of accelerated electrons in the jets [10]. If the magnetic energy density above the disk is larger than the radiation density, the photons produced in $p + \gamma \rightarrow \pi^0 + X \rightarrow \gamma + \gamma + X$ can produce e^+e^- pairs via interaction with the magnetic field. A cascade of such pair production and synchrotron radiation would develop and could provide a spectrum extending up to 100 TeV [19]. Yet another possibility is that those very high energy photons could have a hadronic origin, from $p + \gamma \rightarrow \pi^0 \rightarrow \gamma\gamma$ decay in the jets, with subsequent electromagnetic cascading of the photons down to energies for which the accelerating region is transparent. Since this process would be accompanied by $p + \gamma \rightarrow n + \pi^+$, this model would be favored by the detection of high energy neutrino observations from AGN [10]. pp interactions could accompany $p\gamma$, if the proton density is high enough in the jets, and still be compatible with the time variability of the observations [20]. Predictions for a $5 \cdot 10^4$ m² detector with a threshold energy of 1 TeV vary between a few up to several hundreds of events/year integrated over all AGN, depending on the production model (a compilation can be found in [20]).

The large uncertainty is due to the difficulty to put constraints on the model in order to produce the observed photon fluxes at various wavelengths, the unknown fraction of luminosity participating in nucleon interaction [10] and also to how strong the attenuation of photons by $\gamma\gamma$ reactions with extragalactic photons really is [21]. It is believed that only close AGN can be observed at very high gamma energies [22], whereas observations of neutrinos could be made at much higher energies. This prediction is based on the fact that the cross section for pair-production in γ interactions off intergalactic infrared light is maximized at 1 TeV.

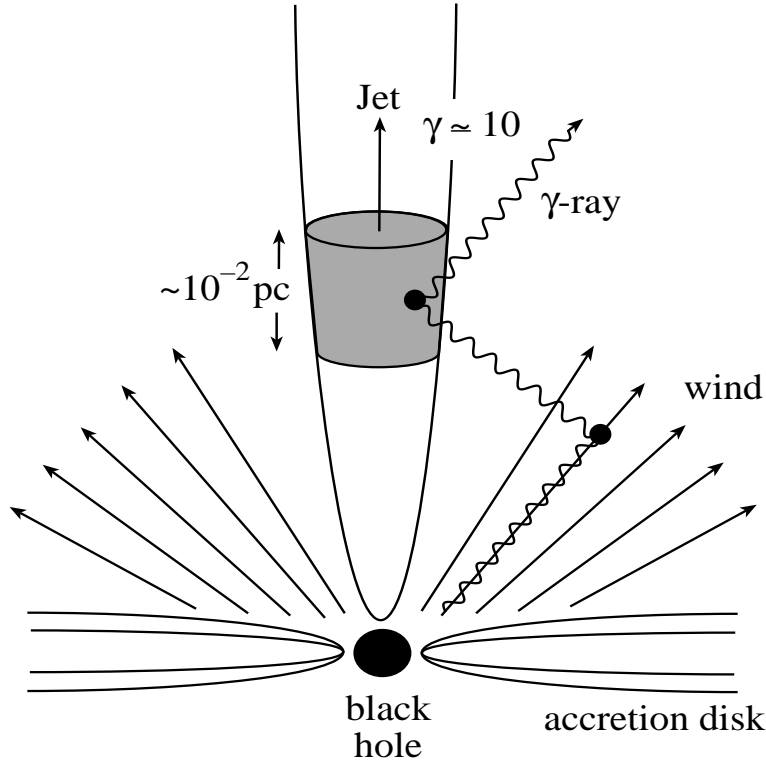


Figure 2: An illustration of the different features of an AGN.

3.1.4 Neutrino cascades

Charged current interaction of high energy (anti-)electron neutrinos emitted from point sources can be detected as electromagnetic cascades in the detector. The signal-to-noise value will be greater than one for lower energies than for ν_μ since the predicted atmospheric spectrum of ν_e is steeper than ν_μ .

Both $\nu_\mu + \bar{\nu}_\mu$ and $\nu_e + \bar{\nu}_e$ can interact with matter through neutral current deep inelastic scattering $\nu + N \rightarrow \nu + X$, yielding a cascade with roughly half the neutrino energy [20, 23].

Glashow resonances at 6.4 PeV are interesting events that could occur [24], producing W bosons through the reaction:

$$\bar{\nu}_e + e^- \rightarrow W^- \quad (12)$$

with a cross-section width of only 2.3 GeV. If a source existed, which would produce electron antineutrinos around this energy, an excess of cascade events would be clearly seen at 6.4 PeV above the background of neutrino-nucleon induced cascades (see Fig. 3 for a comparison of cross-sections).

Such a source could be made up by AGN which, if optically thick to neutrons, could produce antineutrinos via $n + \gamma \rightarrow p + \pi^+$ followed by pion decay [22]. The neutrons's origin would be from proton-photon interactions (see Eq. 11).

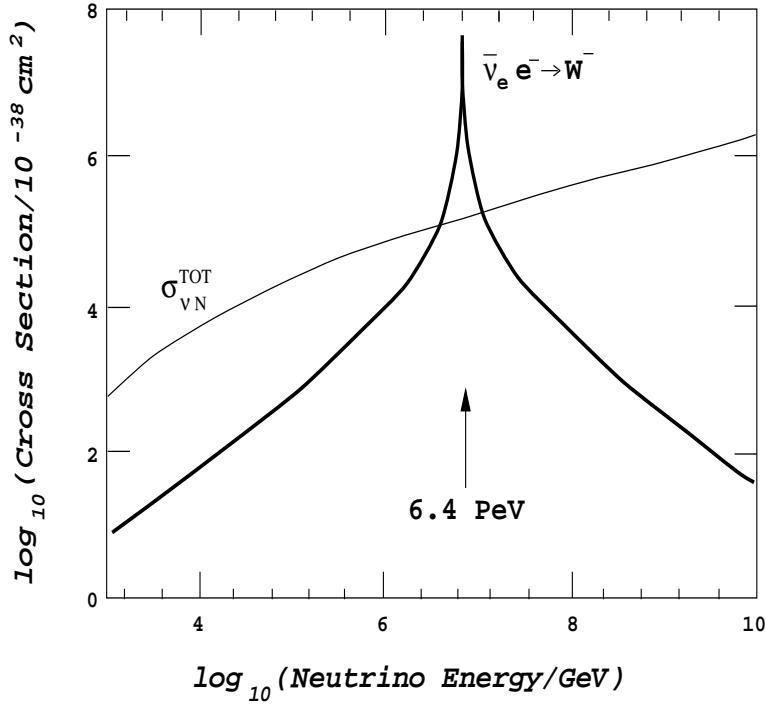


Figure 3: Cross section at the Glashow resonance and total cross section for neutrino-nucleon interaction.

3.1.5 Neutralino annihilation

Weakly interacting massive particles (WIMPs) could constitute the cold component of the dark matter in the Universe. Massive supersymmetric neutralinos in the GeV-TeV range are promising candidates for these particles, and could e.g. be indirectly detected by the observation of their annihilation products.

Neutralinos accumulated in the galactic halo can lose energy by elastic scattering off nuclei and get trapped gravitationally in heavy objects, like the Sun or the Earth. Their density then increases as well as their annihilation rate, until a reservoir is formed. Equilibrium is achieved in the case of the Sun. Neutralinos can annihilate to normal particles (leptons, quarks, gluons) and to gauge and Higgs bosons, for the heavier masses. Hadronization or decay of these annihilation products then produce high-energy neutrinos [25]. These neutrinos can in turn produce muons by charge current interaction with matter and be detected with a neutrino telescope. Neutralinos could thus be detected by observing an excess of events coming from the center of the Sun or the Earth above a background of atmospheric neutrinos. The non-observation of such an excess would then make it possible to rule out some theoretical models predicting it [25].

3.1.6 Background

The first source of background to the detection of muon neutrinos are atmospheric muons with energies large enough to penetrate deeply in the ice, down to the depth of the detector. An estimate of their minimum energy is given by [7]:

$$E_0^{min} = \epsilon(e^{Xb} - 1) \quad (13)$$

where ϵ is the energy at which bremsstrahlung, e^+e^- production and hadronization overtake ionization as the most important energy loss processes, X is the slant depth and b the coefficient for linear energy loss (see section 3.2). This gives a minimum energy of ~ 390 GeV for straight down-going muons in AMANDA-B4 to make it to the center of the AMANDA-B detector. Muons will get more absorbed as their declination angle increases, but since the rate of absorption is exponential with the thickness of matter they have to pass through, this background ceases to be a problem a few degrees above the horizon. As for the remaining events, a large fraction can be filtered away as the time-pattern they leave in the detector is strongly indicative of down-going events. However, the rate of events is large enough for many of them to give *fakes*, i.e. events reconstructed as up-going tracks, although they were produced by down-going muons. One obvious reason for this is the optical scattering in the ice which can degrade the muon's Cherenkov wave-front. This should be especially damaging to near-horizon events and tracks passing outside the detector or far away from the optical modules, since the scattering gets more severe for larger distances.

Air shower induced muons come in bundles and the combination of hits from different particles could also produce fakes

3.2 Muon neutrino detection

Since they only interact weakly with matter, a large volume detector is needed to see neutrinos, in order to compensate for their small cross-section.

The deep inelastic charged current scattering

$$\nu_\mu + N \rightarrow \mu^- + X \quad (14)$$

where N is a nucleon, produces a muon which can be detected and reconstructed to infer the parent neutrino's direction (see Fig. 4). It is thus the main reaction to be detected in order for AMANDA to achieve its primary goal as a telescope able to map the sky with neutrinos. Similarly, one can have

$$\bar{\nu}_\mu + N \rightarrow \mu^+ + X \quad (15)$$

The resulting muon passing through a transparent medium such as ice emits Cherenkov photons at a fixed angle, forming a wavefront going through the detector. A reconstruction of the track is thus made possible by registering the hit pattern produced as the PMs of the array get hit (see section 8.1).

For optimization reasons, a large detector implies a sparse array with typically tens of meters between OMs. Demanding that a few of them should be hit by a photon sets a high energy threshold for the muon. Under these conditions, taking into account only ionization loss of \sim

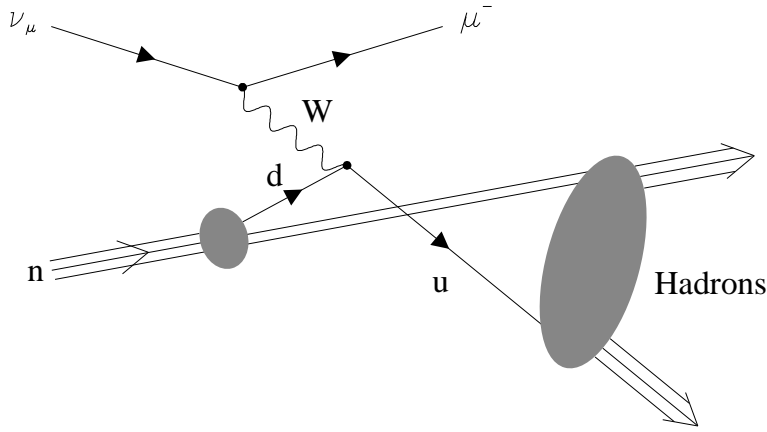


Figure 4: Charged current neutrino-quark deep inelastic scattering.

0.2 GeV/m, a minimum muon energy (and hence neutrino energy) of at least a few GeV can be deduced. With a mass of just 105.7 MeV/ c^2 , this means that a detected muon in that type of detector is highly relativistic. Furthermore, the mean deviation between the neutrino and the muon is

$$\sqrt{\langle \theta_{\mu\nu}^2 \rangle} \approx \sqrt{m_p/E_\nu} [\text{rad}] \quad (16)$$

with E_ν and m_p in TeV and yielding about 1° at 3 TeV [7].

These two facts imply that the path of the muon is a straight track prolonging the neutrino track with a deviation of a few degrees, decreasing with energy.

The inaccuracy due to recoiling effects and to multiple scattering have been estimated for water to be less than 1° after the half mean range of an initial 50 GeV muon and decreasing with energy (see [26], also [27]).

That the minimum energy of a detectable and reconstructible neutrino is of the order of GeV's does not mean that it is the threshold of the detector. Other considerations have to be taken into account in its determination, such as what kind of physics one wants to achieve; what effective area, energy resolution or signal-to-noise is aimed at; if the array is to be used as a telescope or as a particle-detector, etc.

Cross section

The cross-section for the reaction $\nu_\mu + N \rightarrow \mu + \text{anything}$ is given by [28]:

$$\frac{d^2\sigma}{dx dy} = \frac{2G_F^2 M E_\nu}{\pi} \left(\frac{M_W^2}{Q^2 + M_W^2} \right) [xq(x, Q^2) + x\bar{q}(x, Q^2)(1-y)^2] \quad (17)$$

where $-Q^2$ is the invariant momentum transfer between the incident neutrino and outgoing muon, M and M_W are the nucleon and W-boson masses, G_F is the Fermi constant and q and \bar{q} are quark and antiquark distribution functions.

Introduced here also are the Bjorken scaling variables

$$x = \frac{Q^2}{2M(E_\nu - E_\mu)} \quad (18)$$

which is the fraction of the nucleon's four-momentum carried by the interacting quark, and

$$y = 1 - \frac{E_\mu}{E_\nu} \quad (19)$$

At low energies E_ν , the momentum transfer $-Q^2$ in the denominator of Eq. 17 is small compared to M_W^2 and the cross section increases almost linearly with the neutrino energy. At neutrino energies above 3600 GeV, $-Q^2$ becomes comparable with M_W^2 and increases at a rate comparable with E_ν , so the growth of σ becomes much slower (see [7]). A similar behaviour is noted for anti-neutrinos. The energy carried away by the muon is a substantial fraction of the neutrino's: 52% (66% for $\bar{\nu}$) at $E_\nu = 1$ GeV, raising fast to 73% (same for $\bar{\nu}$) at 10^6 GeV, after which the increase is slower [28] (see Fig. 5). The remaining energy is released in a hadronic shower and it is significant, but localized at the vertex.

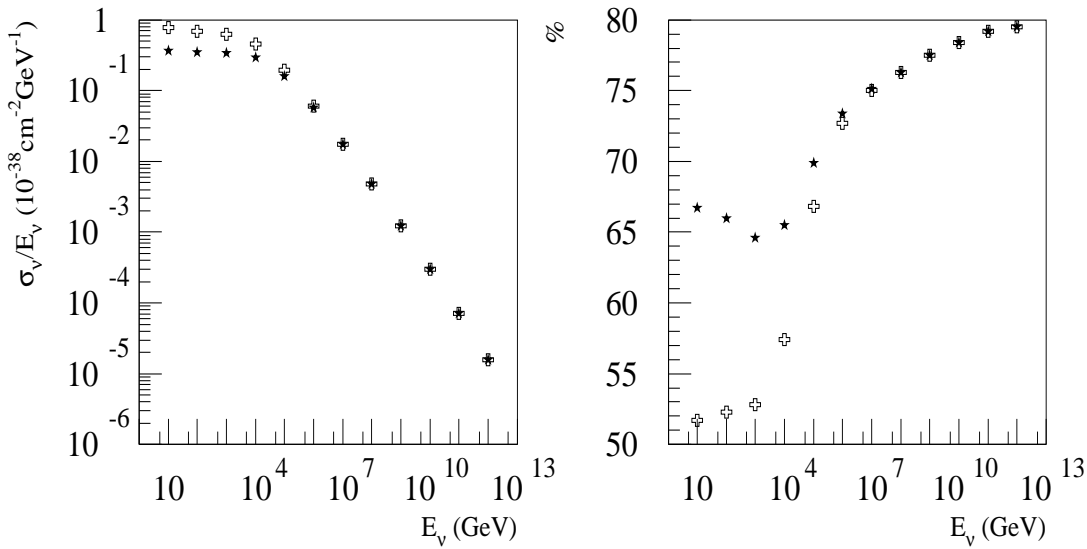


Figure 5: Left: the cross section per energy of the inclusive deep inelastic charged current (anti)neutrino-nucleon scattering $\nu_\mu(\bar{\nu}_\mu) + N \rightarrow \mu + X$ as a function of the neutrino energy. Right: the average fraction $(1 - y)$ (in %) of neutrino energy carried away by the muon. Stars are for antineutrinos and crosses for neutrinos. (From [28]).

Detection efficiency

An important concept when discussing neutrino detectors is that of effective area. It is measured with Monte Carlo simulation techniques and defined as:

$$A_{eff} = \frac{N_{trig}}{N_0} \cdot A \quad (20)$$

where A is the area perpendicular to the direction along which muons are produced, N_0 is the number of muons originating at the area A and N_{trig} is the number of particles which actually trigger the detector (see Fig. 6). A_{eff} approaches an asymptotic value as its size increases.

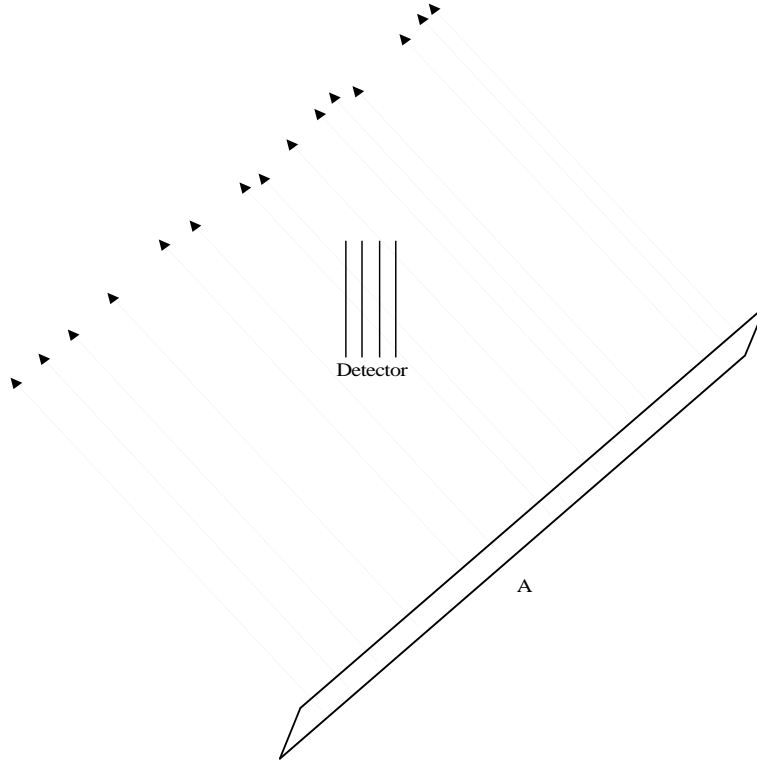


Figure 6: Definition of effective area with infinite tracks

The range of the muons is much larger than the distance between the detector and the emission plane. Note that in this definition A_{eff} is angular dependent. In the same way, an effective volume (see Fig. 7) can be defined as:

$$V_{eff} = \frac{N_{trig}}{N_0} \cdot V \quad (21)$$

where N_0 again is the number of muons generated and V is a volume whose dimensions are much larger than the range of the muons generated in it. The muons' point of production is randomly distributed in the volume and their range follows a distribution upon which the effective volume is dependent. We can thus generalize the definition of an effective area to take into account the finite range of the muons in the following way:

$$A_{eff} = \frac{N_{trig}}{N_0 \cdot R_\mu / L} \cdot A = \frac{V_{eff}}{R_\mu} \quad (22)$$

where R_μ is the mean range of the muon and L the length of the side of the volume used parallel to the muons, which yields the mean number of muons crossing A : $N_0 \cdot R_\mu / L$. For a given effective area, a flux of short range muons will yield a smaller effective volume than long range muons.

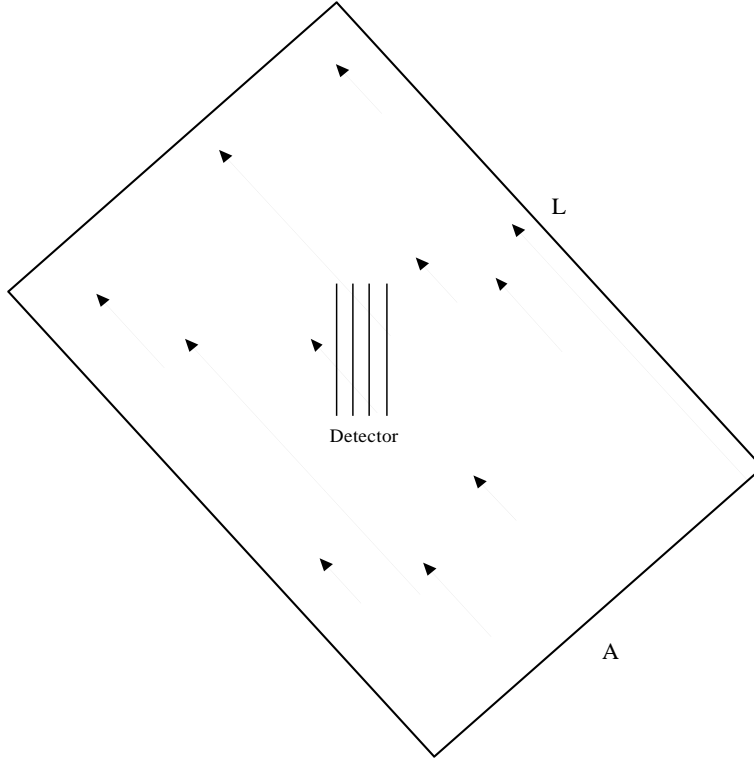


Figure 7: Definition of effective volume with finite-range tracks.

Detection rate

Given a source of muon neutrinos, whatever their origin, how does one estimate its expected rate of detection?

A muon produced with an initial energy E_i will experience energy loss during its passage through matter in the vicinity of the detector and will have an effective range $R(E_i, E_f)$ after which it will decay with energy E_f . Neutrinos with energy E_ν will thus produce muons with various ranges, depending on the fraction of energy transferred. The average range of such muons above a certain detector threshold energy E_μ^{min} is given in [28]:

$$\langle R_{E_\nu}(E_\mu^{min}) \rangle = \frac{1}{\sigma(E_\nu)} \int_0^{1-E_\mu^{min}/E_\nu} R(E_\nu(1-y), E_\mu^{min}) \frac{d\sigma(E_\nu, y)}{dy} dy \quad (23)$$

where $R(E_\nu(1-y), E_\mu^{min})$ is the range of a muon starting with an energy $E_\nu(1-y)$ and decaying with energy E_μ^{min} and σ, y are defined in Eqs. 17, 19. The integral in Eq. 23 averages the muon track lengths over all possible energies transferred from the neutrino.

Thus, the probability that a neutrino with energy E_ν would have produced a muon with an energy $E_\mu > E_\mu^{min}$ is [28]:

$$P_\mu(E_\nu, E_\mu^{min}) = \rho N_A \sigma(E_\nu) \langle R_{E_\nu}(E_\mu^{min}) \rangle \quad (24)$$

where N_A is Avogadro's number and ρ the surrounding medium's density. An useful approxi-

mation found in [10] is:

$$P_\mu(E_\nu, 0) = \begin{cases} 1.3 \cdot 10^{-6} E^{2.2} & \text{for } 1 \text{ GeV} < E_\nu < 1 \text{ TeV} \\ 1.3 \cdot 10^{-6} E^{0.8} & \text{for } 1 \text{ TeV} < E_\nu < 1 \text{ PeV} \end{cases} \quad (25)$$

the neutrino cross-section goes from linear to logarithmic growth in those two energy intervals (see Fig. 5) and the muon range goes from linear to constant behaviour. Then the flux of muons due to incoming neutrinos can be obtained as

$$\Phi_\mu(E_\mu^{min}, \theta) = \int_{E_\mu^{min}}^{\infty} \Phi_\nu(E_\nu, \theta) P_\mu(E_\nu, E_\mu^{min}) e^{-\sigma_{tot}(E_\nu) N_{AX}(\theta)} dE_\nu \quad (26)$$

which is a convolution of the neutrino flux with the probability defined in Eq. 24 and an exponential term taking care of the absorption of neutrinos as they pass through the Earth. Absorption becomes important for $E_\nu \geq 10^7 \text{ GeV}$ [10].

Folding the differential flux given by Eq. 26 with the effective area in an integral over all declinations yields the expected rate of events Γ :

$$\Gamma = \int \Phi_\mu(E_\mu^{min}, \theta) A_{eff}(\theta) d\theta \quad (27)$$

The Cherenkov effect

A high energetic muon passing through the ice will emit Cherenkov light at a fixed angle. The condition for this effect to happen is that a charged particle travels with a speed higher than the speed of light in the medium ($\beta \geq 1/n$), in which case it has an energy greater than the critical Cherenkov energy:

$$E_{Cher}(\lambda) = \frac{m}{\sqrt{1 - \frac{1}{n^2(\lambda)}}} \quad (28)$$

where $n(\lambda)$ is the wavelength-dependent refractive index of the transparent material considered. In the case of AMANDA, where we use ice, $n = n_i = 1.32$ (see Fig. 32) over the range of wavelength the optical modules are sensitive to (between 300 and 600 nm) and if the particle under consideration is a muon, this yields a critical energy in ice of 160 MeV. The Cherenkov angle \check{c} relative to the velocity of the particle at which the photons are emitted is then given by

$$\cos \check{c} = \frac{1}{\beta \cdot n_i} \quad (29)$$

which is simply $1/n_i$ when $E_\mu \gg m_\mu$, yielding $\check{c} = 41^\circ$, in which case the Cherenkov wavefront is just a cone with an opening half-angle of 49° as shown in Fig. 8.

The energy lost in emitted light per unit length and unit frequency is:

$$\frac{dE_\mu}{dx d\nu} = \frac{2\pi\alpha h}{c} \cdot \nu \cdot \left(1 - \frac{1}{\beta^2 \cdot n_i^2(\nu)}\right) \quad (30)$$

with α being the fine structure constant, $\alpha = 1/137$. In our case, with a limited optical window due to the sensitivity of the PM and to the filtering power of the glass-sphere enclosing it, the

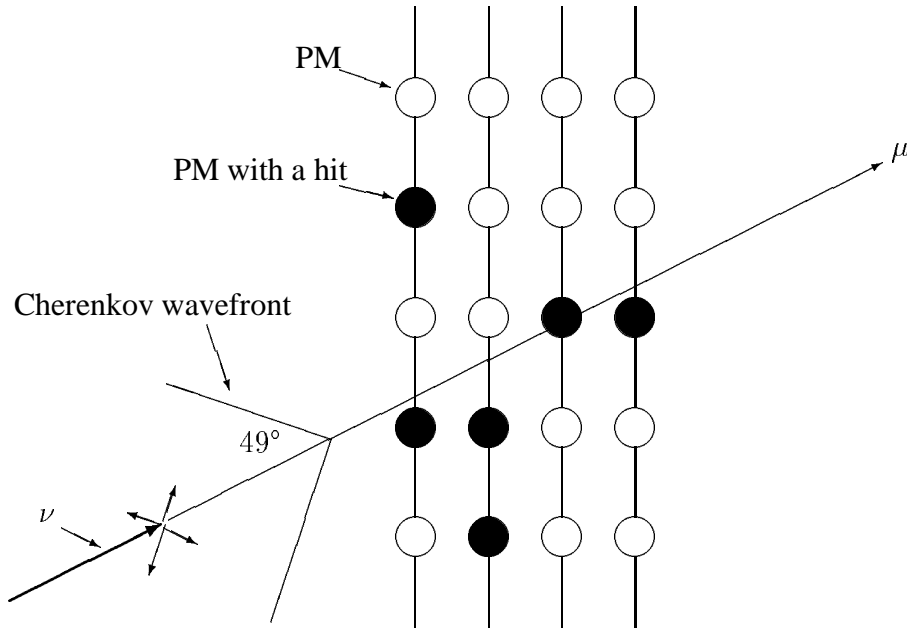


Figure 8: A high-energy muon passing through the detector with an accompanying Cherenkov shock-front

frequency dependence of n_i can be neglected and a value of 1.32 is used. This leads to dN/dx , the number of photons emitted per unit length in the wavelength interval λ_1 to λ_2 :

$$\frac{dN}{dx} = 2\pi\alpha \int_{\lambda_1}^{\lambda_2} \frac{\sin^2 \check{c}}{\lambda^2} d\lambda \quad (31)$$

see [29, 8]. For the wave-length window 300-600 nm of concern to us, we get ~ 330 photons/cm. Since n_i varies little in that interval, the spread in \check{c} is very small, yielding a strongly peaked direction of emission. The energy loss caused by the Cherenkov effect is ~ 0.02 MeV/cm, i.e. very small compared to losses by other processes.

Muon energy loss

In addition to the Cherenkov light, other losses occur along the muon's propagation in ice. They can be subdivided in continuous and discrete processes. The first kind of energy deposition is by ionization and is the dominant part up to ~ 500 GeV, when Bremsstrahlung, direct e^+e^- pair production and muon hadronization become important effects. Production of $\mu^+\mu^-$ also occurs for muon energies above 100 GeV, but contributes less than 0.01% to the total energy loss [8]. Above 1 GeV, the rate of energy loss per length by ionization is constant, whereas it grows roughly linearly for the remaining processes. The following formula can thus be used for muon energy loss:

$$-\frac{dE}{dx} = a(E) + b(E) \cdot E \quad (32)$$

where x is in g cm^{-2} and $a(E)$ is given by the Bethe-Bloch formula [8]:

$$-\frac{dE}{dx} = Kz^2 \frac{Z}{A} \frac{1}{\beta^2} \left(\frac{1}{2} \ln \frac{2m_e c^2 \beta^2 \gamma^2 T_{max}}{I^2} - \beta^2 - \frac{\delta(\gamma)}{2} \right) \quad (33)$$

in which $b(E)$ is the sum of the discrete processes' contributions and the correction term δ (from knock-on electrons) causes the energy loss to become constant for $\beta\gamma > 100$, i.e. upon entering the Fermi plateau [30], which is reached at around 10 GeV for muons. Both $a(E)$ and $b(E)$ can be approximated with constants. Typically $a \approx 2 \text{ MeVg}^{-1}\text{cm}^{-2}$ and $b \approx 3.4 \cdot 10^{-6} \text{ GeVg}^{-1}\text{cm}^{-2}$. By solving Eq. 32, we get the mean range of a muon starting with energy E_i and decaying with

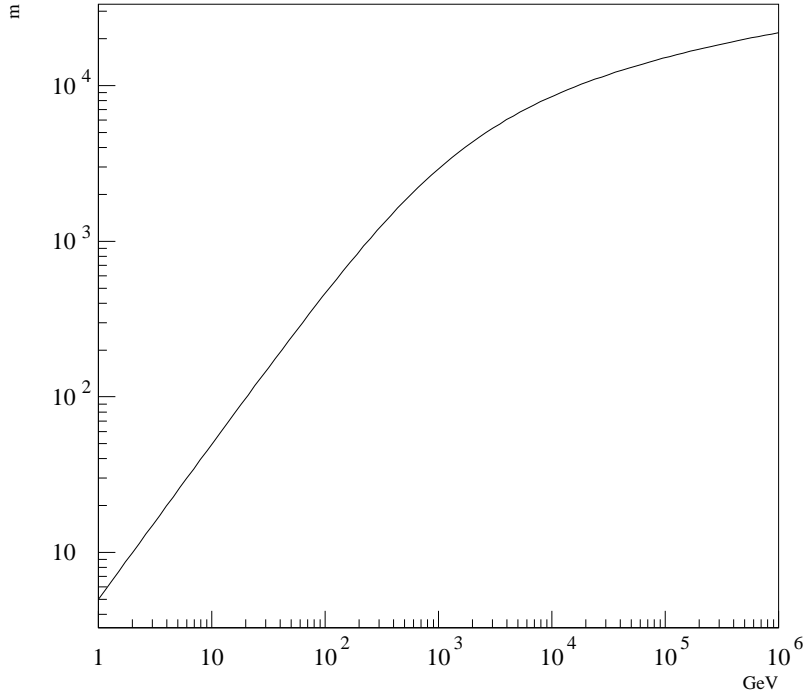


Figure 9: Mean range of a muon in ice as a function of its energy.

energy E_f :

$$R_{eff}(E_i, E_f) = \frac{1}{b} \ln \left(\frac{E_i + E_c}{E_f + E_c} \right) \quad (34)$$

where $E_c \equiv \frac{a}{b}$ is the critical energy above which stochastic processes dominate over ionization. Below E_c , the muon range increases linearly with the muon energy, and above, it is proportional to $\ln(E_\mu)$. When $E_\mu > E_c$, the fluctuations are large and a Monte Carlo simulation is necessary to take into account the stochastic nature of the energy loss.

Since the muons considered here have high energies, so do the particles they produce during their propagation through ice. As a result, they are boosted in the same direction and the Cherenkov light they emit is sent out at an angle relative to the muon close to 41° as well. The smearing induced is of the order of a few degrees (see [26, 31]).

Electromagnetic showers

Both electrons (positrons) and photons of high energy can initiate electromagnetic cascades. These processes are of interest in muon propagation, since most of the energy losses can be assigned to electromagnetic interaction.

An electron can emit a photon by bremsstrahlung, which will produce an electron-positron pair, in turn radiating, and so on. At each generation, the number of particles is doubled and the energy of the first particle evenly distributed among them. The cascade goes on until the energy per particle is below the critical energy, at which point ionization loss becomes more important. The transition is abrupt and the number of generations is then:

$$\frac{\ln(E_0/E_c)}{\ln(2)} \quad (35)$$

where the critical energy for an electron traveling in ice, $E_c = 92$ MeV [32]. The number of particles with energy greater than E_c is $N(> E_c) = E_0/(E_c \ln 2)$, i.e. it increases linearly with the primary energy.

The radiation length X_0 is defined as the length after which the particle energy decreases to E_0/e :

$$X_0 = \frac{716.4 \text{ [gcm}^{-2}\text{]} A}{Z(Z+1)\ln(287/\sqrt{Z})} \quad (36)$$

which yields $\sim 36 \text{ gcm}^{-2}$ for ice. The mean longitudinal profile of the energy deposition is described by a Gamma distribution:

$$\frac{dE}{dt} = E_0 b \frac{(bt)^{a-1} e^{-bt}}{\Gamma(a)} \quad (37)$$

where

$$t = \frac{x}{X_0} \quad (38)$$

is the number of radiation lengths and $b \approx 0.5$. With these definitions, the maximum of the function in Eq. 37 occurs at:

$$t_{max} = \frac{a-1}{b} = \ln(E/E_c) + C_j, \quad j = e, \gamma \quad (39)$$

where $C_e = -0.5$ for electron cascades and $C_\gamma = 0.5$ for photon cascades [8, 32, 33]. t_{max} increases only logarithmically with energy and is of the order of a few meters. The average spread due to Coulomb scattering is inside a radius of three Moliere lengths R_M [32], with

$$R_M = 21 \text{ [MeV]} \cdot \frac{X_0}{E_c} \quad (40)$$

i.e. a few tens of centimeters. Eventually, after the mean energy per particle of the shower drops, nearly all the energy is deposited by ionization [33].

Hadronic showers

A hadron shower occurs when a hadron scatters inelastically with a nucleus, producing more hadrons and so on. The scale is set by the absorption length λ of the material, which is about 75 cm for ice. The maximum of the shower occurs at

$$\frac{x}{\lambda_I} \equiv t_{max} \approx 0.2 \ln(E/1[\text{GeV}]) + 0.7 \quad (41)$$

As for electromagnetic showers, the length of a hadronic shower grows as the logarithm of the energy. However, the energy fluctuations are larger, since the fraction of π^0 mesons fluctuates greatly. The contribution to the deposited energy of that particle, which decays to two γ s showering electromagnetically, is larger than that of π^\pm and this leads to fluctuations in energy [32]. In a hadron shower, 30% of the energy is lost by the breakup of nuclei, nuclear excitations, protons, neutrons, and is not seen electromagnetically [33].

4 Detector description

4.1 String description

The AMANDA detector consists of several strings buried deeply in the glacier ice, with a typical inter-string distance of ~ 30 m. In the beginning of 1996, four holes were drilled and new strings were deployed in the first stage of the construction of the deeper detector AMANDA-B, which we will refer to here as AMANDA-B4. Each string supported 20 optical modules, numbered accordingly from the shallowest to the deepest, with the exception of the fourth string, which had 26 modules. The modules were all installed facing down, except for a few which were oriented facing up, for checks of their angular efficiency and atmospheric muon studies.

The strings run from the surface of the ice sheet down to depths between 1900 m and 2000 m and were deployed in holes between 2000 m and 2180 m deep. The differences in lengths were intentional, the idea being that they would allow for measurements of the optical parameters of the ice over a larger range.

The main cable of a string is composed of 20 coaxial RG59 YR-cables from Belden bundled together inside a supercable, with breakouts for PM connectors every 20 meters, starting from a depth between 1520 m and 1570 m, depending on string number. The purpose of those cables is to supply the PMs with high voltage and to transmit the PM pulses up to the surface electronics. Because of the thickness of the coaxial cables, their number is limited to at most 20 by the maximum size and weight of the main cable, which has to be carried in by air to the South Pole station and by the dimensions of the equipment (reels and winches) available for deployment.

Separate cables holding optical fibers (one single mode and one multi-mode per OM) were deployed along with the strings. Each optical fiber can lead pulsed laser light from the surface and terminates with a nylon ball used to diffuse the light right below a module. The main purpose of their installation was to have a photon source to calibrate the PMs.

Several other cables were also added for apparatus such as in-situ light sources used for PM time calibration and/or optical studies of the ice and inter-strings distance measurements, and pressure and temperature sensors. These service cables are enclosed in the supercable. Two radio receivers from the RICE (Radio Ice Cherenkov Experiment) were also deployed at shallow depths [34] for feasibility studies of an anticipated PeV neutrino detector.

The four strings were thus equipped with 86 OMs and various light sources distributed as follows:

- String 1: 20 OMs containing a Hamamatsu PM each, all equipped with nylon balls and facing down. The exceptions to this are modules #1 and #10 which are facing up. One RICE detector at 250 m depth, LED modules right above OM #1 and below OMs #7,12 and 19. A nitrogen laser-module (337 nm) 10 meters below OM #16.
- String 2: 20 OMs, all Hamamatsu, all equipped with nylon balls, facing down except for OM#1 and #10. One RICE detector at 140 m depth, LED modules under OMs#1,7,13 and 19 and a DC halogen lamp 10 m below OM#16. A second-harmonic generator was also installed.
- String 3: 20 OM, all Hamamatsu except OM#1 and 2 which are of the type Thorn EMI 9353, all equipped with nylon balls, facing down except for OM#1 and #10, a DC halogen lamp under OM#16.

- String 4: 26 OMs, all Hamamatsu, all equipped with nylon balls, all facing down except OM#1, 10, 19, 20, 21, 23 and 25. LED modules above OM#1 and 10. Anticipating a change of technology in the next stage of AMANDA-B and in order to perform tests on them, twisted-pair cables from Ericsson Cable were incorporated in a separate cable instead of coax for OM#21-26.

In addition, thermistors and pressure sensors were placed near the top, middle and bottom module of each string to monitor it during deployment.

The most important piece of calibration instrumentation are the two optical fibers going from the surface where they are coupled to a dye laser, to a nylon diffuser attached on the main cable ~ 50 cm below each OM. One of them is single mode, with a FWHM time resolution of ~ 7 ns at 530 nm and is used for time-calibration whereas the other is multi-mode with a FWHM time resolution of ~ 15 ns at the same wavelength. The multi-mode fiber can transmit wavelengths of 450 nm and longer and is used for inter-string data collection mainly.

Time-calibration of the PMs is performed by pulsing a laser connected to these fibers at the surface and, knowing the time at which the pulse reached the nylon ball, the time it takes for the PM signal to reach the surface can easily be found. That time is the sum of the PM's transit time and of the travel-time through the cable of the electrical pulse it sent out. A dye-laser was used in 1996 to take such calibration data at a 10 Hz rate.

These measurements were performed on each OM individually, at their 10^9 -gain voltage, so the requirement on the light output for that purpose was not very high. However, the maximum intensity that can be sent out at the diffusers is 10^8 photons/pulse, which makes it possible to reach neighboring strings. This was used to acquire data used in ice analysis and position calibration.

The laser which was installed at a depth of 1830 m on string 1 contains a N_2 -laser, built at UCB [35]. It has a maximum intensity of 10^{10} photons/pulse, which makes it easily detectable by OMs more than 200 m away. The laser emits light isotropically at a single wavelength of 337 nm in a 2π sr up-looking solid angle. It is pulsed at a 6 Hz rate, with a time resolution of ~ 3 ns. The $\sim 2 \cdot 10^{-5}$ fluorescence contamination is taken care of by a filter at the diffuser. Three halogen DC-lamps were also deployed, one broadband with a maximum intensity of 10^{18} photons/second and two with a maximum intensity of 10^{14} photons/second equipped with filters at 350 nm and 380 nm respectively. The main purpose of these light sources was to measure the relative photon flux as a function of distance from the source.

The several LED beacons installed on strings 1, 2 and 4 can either be pulsed at 500 Hz with a maximum intensity of 10^6 photons/pulse or used in DC mode with 10^6 photons/sec. They emit light with a wavelength 380 nm and 450 nm.

A second harmonic generator (SHG) was also installed, which can send pulses of light at 532 nm wavelength (doubling the frequency of 1064 nm light sent down the fiber from the surface) with a time resolution of 7 ns and an intensity of 10^7 photons/pulse.

Six more strings were added during the 96/97 season, which make up the AMANDA-B10 detector, together with AMANDA-B4. The cables composing these added strings were of a different construction than the first four, using twisted-pair instead of coaxial cables for signal transmission allowing for 36 OMs instead of a maximum of 20 OMs per string.

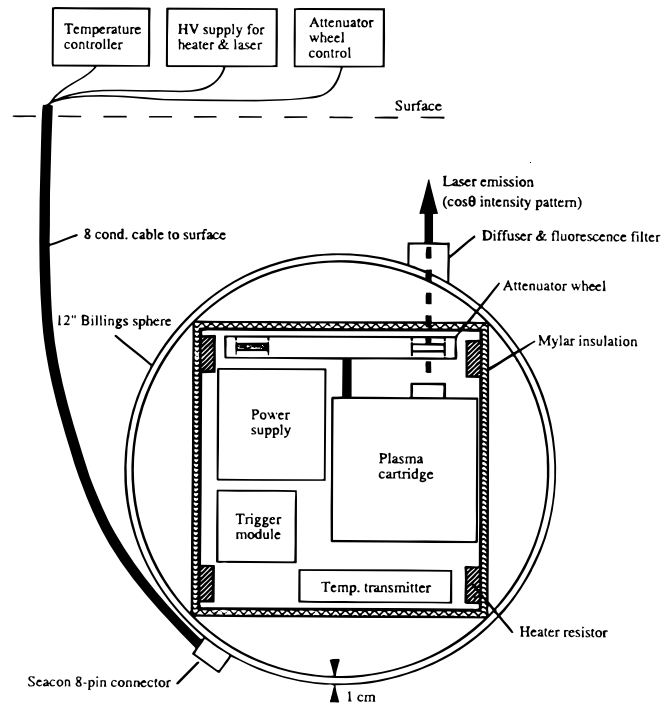


Figure 10: N_2 -laser module installed between OMs#16 and 17 on string 1, enclosed in a Billings sphere. The temperature can be monitored and controlled from the surface, as well as the amount of light emitted

4.2 Deployment

The detector is located at the Amundsen-Scott base at the South Pole, where access is impossible except for the summer season stretching from mid-October to mid-February. During that period, the drilling equipment is set up in a few weeks and the actual drilling of holes proceeds. The Polar Ice Coring Office (PICO) is responsible for this part of deployment. Other parts of the logistics are run by the Antarctic Support Associates (ASA). Testing of OMs and installation of additional and new electronics for the DAQ system are done by the AMANDA collaboration in parallel with the drilling. These activities occur for the main part inside the area of the Martin A. Pomerantz Observatory (MAPO) building assigned to the AMANDA experiment, and temporary buildings are also set up for the summer season. MAPO is the main scientific facility for this project, but the central building of the base is the South Pole dome, located some 800 m from it. Inside, AMANDA shares a portion of a building with SPASE used as a workshop/computer room. It serves also as the working place of the winter-overs.

The ice sheet at the South Pole is 3000 m thick, allowing for drilling to depths ~ 2000 m. Furthermore, the diameter of an OM is 30 cm, so the holes in which the strings are deployed must have a large opening. Since removing a column of ice with these dimensions mechanically would be very costly and difficult, the drilling of the holes is done by melting the ice with a hot-water drill. The resulting holes have a depth of ~ 2000 m and a diameter of 60 cm. The first 50 or so meters are firm ice permeable to water, which means the melted ice can not be reused and hot water must be provided from somewhere else. Deeper than that dry portion of the hole,

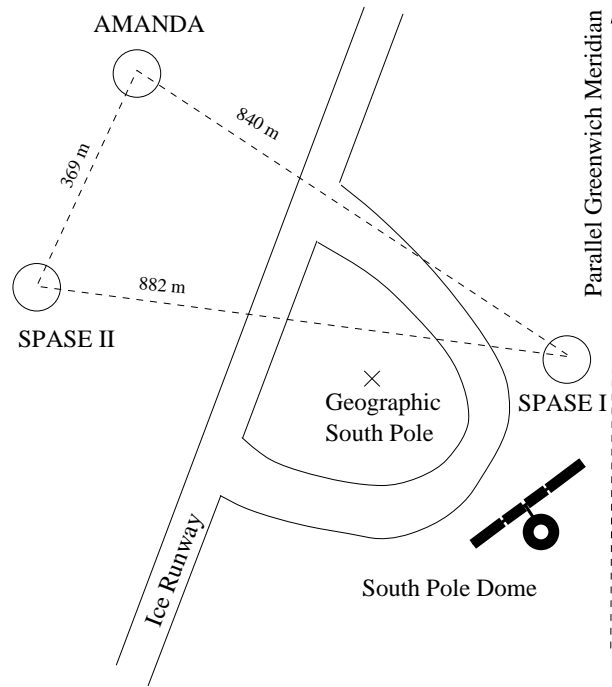


Figure 11: Relative locations of AMANDA and the two sites of SPASE

the melted ice can be recycled and heated up with boilers at the surface. The drill is constituted by a hose the length of a hole, with a drill head eight meters long attached to it, equipped with various instruments monitoring its direction, the water flow and the diameter of the hole. This information is logged constantly and used later to reconstruct the profile of each hole and to calibrate the position of the array. The drill head ends with a nozzle through which 80°C hot water is pumped at a rate of 150 liter/minute, melting and scraping off bits of ice with its turbulent flow. The power requirement for drilling this way with a speed of 1 cm/s is 1.9 MW.

It takes about three and a half days to drill a hole, depending on weather conditions, mechanical problems and sporadic re-freezing of portions of the hole which makes reaming necessary (i.e. taking the drill up to increase the hole diameter). Preparations are time consuming in the beginning of the season and include the unpacking of new tools flown in that year, digging up of old equipment from previous campaigns, setting up of several boilers used to heat up the water flow from and into the hole and many other tasks. Some time is also allocated at the end of the season for the tearing down of temporary installations and packing down most of the equipment to be either stored at the South Pole or flown back home.

The deployment of a new string proceeds immediately after the drilling of each hole, and must be completed within a time limit set by the re-freezing time of the hole which is 35-40 hours. After the drill has been removed, the main cable containing the HV and service cables is lowered into the hole. An optical module is connected to a cable breakout every 20 meters and a nylon ball with its optical fiber is attached below it. The OMs are connected one to the other with sections of steel cable and when all 20 modules are installed, the last module is attached to the main cable with a cable stop. The total mass load on it is large but the total weight it must support is reduced by the buoyancy of the OMs. The main cable and the optical fibers are rolled up on winch operated reels and released very slowly in the beginning, with frequent

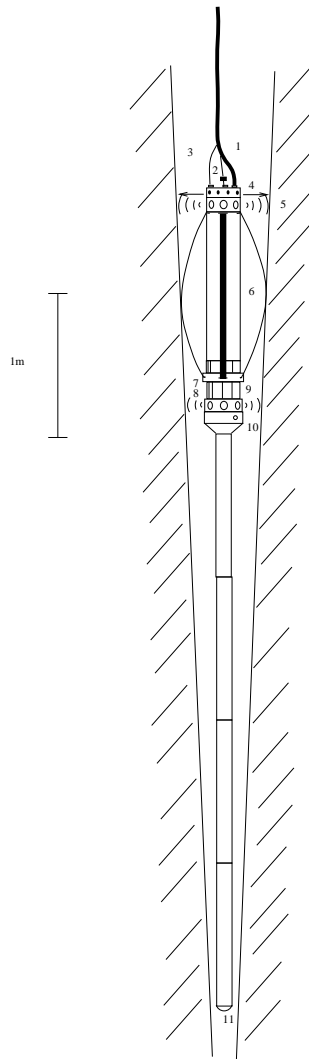


Figure 12: The drill head, equipped with a sonar (5), tiltmeters (7), pressure gauges (10), flow rate meters (8) and calipers (9)

stops during the first 400 meters of so of OM installation. When all the OMs have been attached and connected, the lowering of the string proceeds faster and without interruption until it has reached the depth aimed for. Pressure sensors and cable marks are used to assess the depth and continue recording the conditions in the hole over the refreezing period. A pressure maximum of 460 atm is reached over time, but it decreases down to half that value as the ice gets cooler. A thermodynamical equilibrium is not reached until after several months, when the temperature has dropped to -55°C close to the surface and -30°C at 2000 meters depth, following the temperature vs. depth profile of the surrounding glacier ice (see [48]). The deployment of a string takes 9-18 hours and the high voltages are not applied on any OM before they have frozen in, which takes several days. In the mean time, they are checked by measuring the PM resistances to detect leaking connectors. The failure rate is typically below 10% (3% for the six strings of the 1996-97 season) and failures after refreezing are exceptional, even over a period of a few years. The PMs are chosen so that those calibrated to a higher voltage are deployed high up in the detector and those with lower voltage are put deeper in the array, in order to minimize the

strain put on them.

4.3 Optical modules

An optical module is basically a photomultiplier enclosed in a sphere of thick glass. The photomultiplier is a 20 cm Hamamatsu R5912-02, a 14-stage version of the 12-stage R5912 tube, modified for AMANDA (see Fig. 13). This was done in order to operate it at the gain of 10^9 needed to get PM pulses through 2000 m of cable without further amplification. It has a bialkali photocathode sensitive to photons with wavelengths between 300 nm and 650 nm and a peak quantum efficiency of 23% at 420 nm (see Fig. 19).

This PM was also chosen for its other qualities, such as a large photocathode area, good time resolution, and low dark count. The voltage-divider circuit designed by Hamamatsu is optimized to yield an good sensitivity at the single photo-electron level, which gives a limited dynamic range of typically ten p.e.'s. It is slightly modified in its actual implementation in order to be used either with a coaxial or with a twisted-pair cable [36](see Fig. 14). In order to get a high efficiency and a good time resolution, grids (F) are used to focus the cathode electrons before passing through the 14 dynode stages (D). Seen from the front, the PM- cathode is circular-

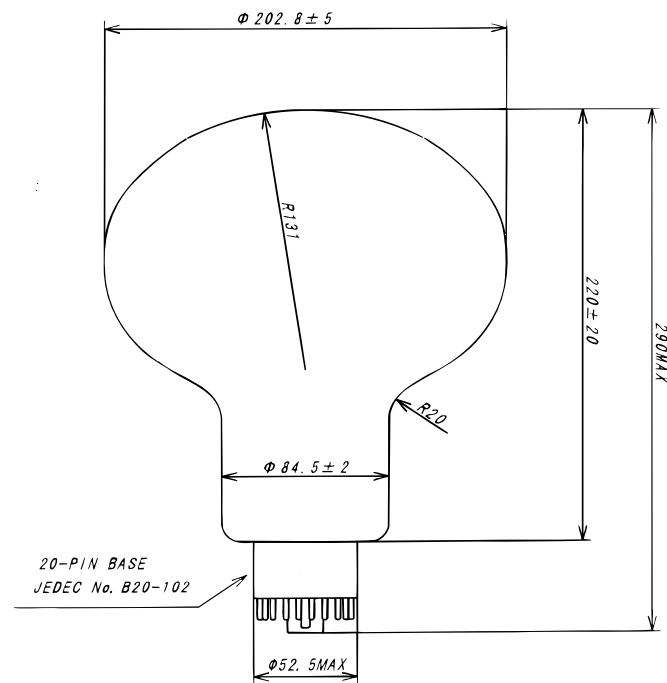


Figure 13: The 14-stage R5912-02 Hamamatsu photomultiplier

shaped, with a radius of 10 cm, but its actual curvature radius is 13.1 cm. The timing properties measured with a short cable in the laboratory yield a time jitter of ~ 3 ns FWHM, with small variations between individual PMs. This value is measured to ~ 7 – 10 ns in-situ, with larger variations between PMs, a degradation largely due to the longer cables, between ~ 1600 and 2100

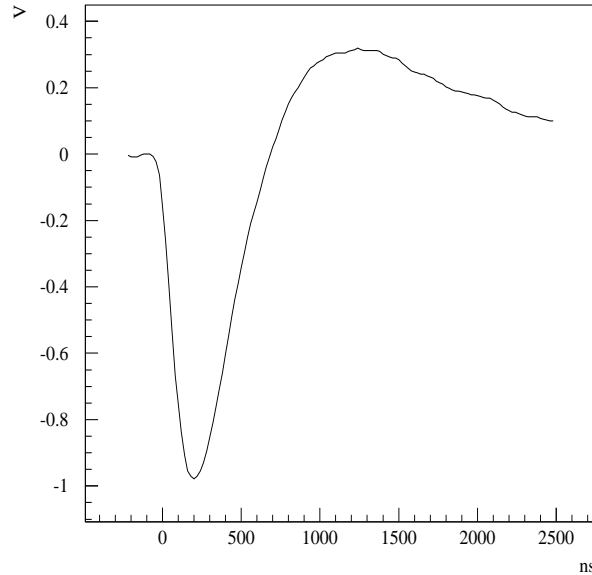


Figure 15: A typical one photo-electron pulse in AMANDA-B4

as such is affected by the presence of air bubbles, isotropizing photons near it. These bubbles could be forming around it during the re-freezing of the melted ice following deployment.

The PM is housed in a 12-inches diameter sphere of 9 mm thick glass from Billings, rated for 660 atm. These spheres have less good optical qualities than the ones from Benthos, previously used for AMANDA-A with EMI PMs. However, the Billings sphere had to be chosen, since Benthos could not manufacture a sphere large enough to house a HAMAMATSU PM. Its transmissivity is 90% from 400 nm and above, in the optical region, but it drops sharply with a 50% cut-off at 364 nm whereas Benthos glass transmits light 30 nm further down (see Fig. 18). This is unfortunate since in this wavelength range, the cathode still has a high quantum efficiency and the Cherenkov light we wish to detect has a $1/\lambda^2$ -spectrum (see Eq. 31). However, studies of various wavelength-shifters are underway to remedy this loss [20, 41] in future OM deployments.

The optical contact between PM and glass is ensured with a ~ 1 cm thick layer of optical silicon gel from General Electrics. The only additional component of an optical module apart from the PM itself is the base card holding the bleeder circuitry. A big advantage of this OM is that all amplifiers, discriminators, ADCs, TDCs, etc. are located at the surface, connected to the modules by 2000 m of cable. Thus, possible failure of the electronics has a higher chance of being reparable and even upgrades are made possible over the years, adding flexibility to the detector. Another advantage is the small need for the design and manufacturing of dedicated electronics which must sit in the OMs. Once the PM has been potted in one of the two Billings half spheres, these are sealed together with rubber tape and a metallic harness for mechanical support is fitted around the OM.

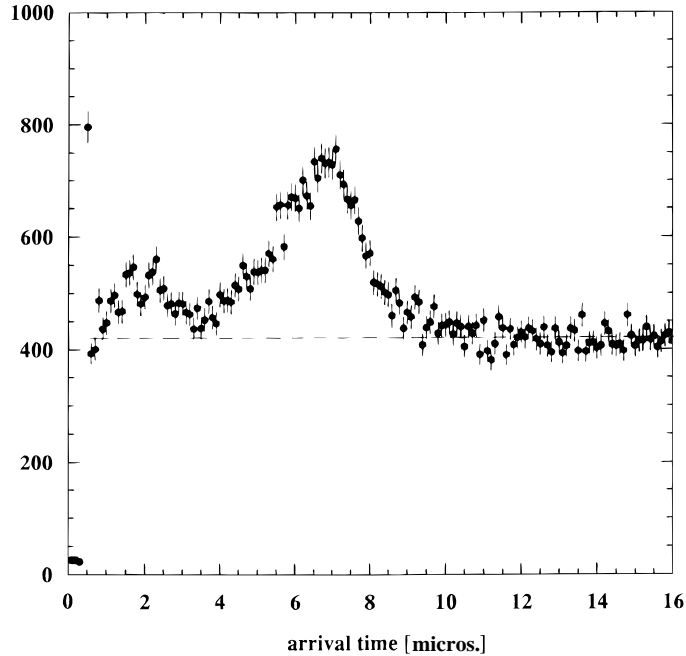


Figure 16: Arrival time distribution of the second leading edge relative to the first leading edge time, with a threshold set at $1/4$ p.e. The first peak, centered around $2 \mu s$, indicates 0.5% after-pulsing, and the second peak at $7 \mu s$ indicates after-pulsing of the order of 2.5%. The amount of after-pulses is relatively low and therefore not representative of a typical PM (see Fig. 17)

4.4 Electronics and DAQ

An event is the outcome of light being produced in or outside the detector and resulting in OMs getting a hit. In a typical AMANDA event, each OM can give a series of pulses which can be resolved, if separated from each other by more than a few hundred nanoseconds. The data recorded consists of the time at which each negative pulse gets below a constant threshold level (leading edge) and when it gets back to that level (trailing edge). This allows for the calculation of the time-over-threshold (in this case the expression time-below-threshold would be more correct), a measure that can be used to reject noise if it does not fit within the typical range of one or several photo-electrons.

The amplitude of a pulse is also measured by a voltage sensitive ADC and that information kept, but only one such value is recorded per OM hit. In case several photo-electrons are produced, the information will thus consist of as many trailing and leading edges as there are resolved pulses, and of the largest amplitude for them all. Also recorded is the GPS time at which the event occurred, useful to match it with possible coincidences in other detectors operating nearby (AMANDA-A, SPASE 1 and 2, GASP), or with astrophysical events (e.g. supernovæ).

In what follows, the multiplicity of an event is defined by the number of OM hit, whereas the string-multiplicity is the number of strings that contain at least one hit OM.

For an event to trigger the detector, it must first produce at least N_{hit} OMs with hit times within a sliding window of $2 \mu s$ and the string multiplicity must be at least N_{str} .

The multiplicity N_{hit} has to be at least 5 for any reconstruction of muon tracks to be possible

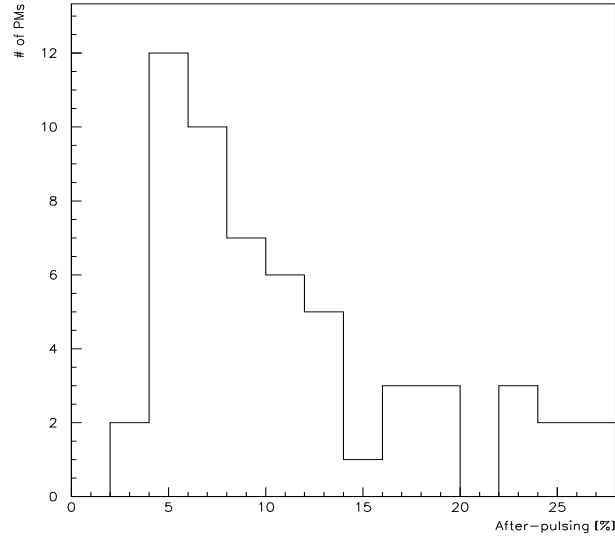


Figure 17: Distribution of the percentage of after-pulsing over PMs.

in the first place and N_{str} has to be at least 3 in order to avoid the symmetry across the plane formed by two parallel strings a value of $N_{str} = 2$ could produce. A string multiplicity of 2 would still allow to discriminate between up- and down-going muons, but would yield an ambiguous azimuthal angle due to that symmetry. These numbers can be set to anything, but for the AMANDA-B4 detector operating during 1996, they were $N_{hit} = 8$ and $N_{str} = 1$, shortened to 8/1. This trigger was decided just after the deployment in the view that with unknown ice-properties, a weak condition would be better since it could always be increased off-line. Having as weak a trigger as possible has proved useful for comparison with Monte-Carlo simulations. The lowest trigger was thus set, which would produce a data-flow the data-acquisition system could accomodate. Triggers can also be sent by other experiments (AMANDA-A, SPASE-1, SPASE-2 or GASP), telling AMANDA-B to record whatever data there is.

The differences in cable-lengths for modules at different depths are not compensated before triggering. Because of the way the trigger condition is set, this has the effect of suppressing the number of events from down-going particles. Ideally, for such events, the time difference between two modules hit is increased by the time it takes for electric signal from the lower OM to travel up to the upper one. On the opposite, the Cherenkov light from an up-going muon will hit the lower module first, when hitting the upper module, the first signal will already have travelled up a bit in the cable. This picture holds in the ideal case of clear ice and straight up- and down-going muons. However, simulation studies show that even for AMANDA-B4, some gain can be made on the signal to noise ratio of up-going events versus atmospheric muons, by extending the delays of deeper modules relative shallower ones [42].

The time difference between signals from the highest and the lowest module for an up-going relativistic muon passing through AMANDA-B4 is ~ 300 ns and $\sim 4 \mu s$ for a down-going muon. The length of the time-window used was set to $2 \mu s$ to include hits caused by scattered photons.

The AMANDA electronics is shown in Fig. 21. The first part is composed of the 86 PMs and

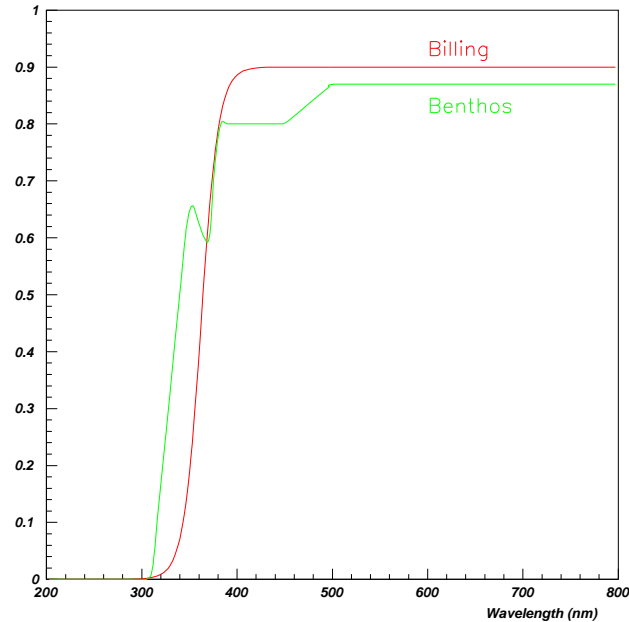


Figure 18: Transmissivity of the Billings sphere as a function of wavelength as compared to the same curve for Benthos glass.

four cables already described. The signal from each cable is fed into one channel of a SWedish AMPlifier module (SWAMPs [36]), consisting of:

- a pick-up, which is a DC-blocking high-pass filter, linear in the frequency range of the pulses when they reach the surface (0.1 MHz - 10 MHz).
- the signal is then split and sent to two independent amplifiers with an amplification range between $\times 2$ and $\times 200$. One of them ('A') is set to $\times 100$ and the other ('B') to $\times 25$.
- a three-fold fan-out for the 'A' signal.
- a $2 \mu\text{s}$ delay for the 'B' signal.

A test input/output was implemented on each channel, allowing to send a common test-pulse to several of them, for calibration purposes. One 9U-Euro crate holds the SWAMP modules needed for AMANDA-B4 and each one of these in turn contains 16 channels.

The second part of the electronics concerns the treatment of the amplified pulses. All data conversion is made by CAMAC modules. The delayed 'B' signal is sent to a Philips 7164 peak sensing ADC with 16 channels. An integrating ADC would have been less adequate, because of the large overshoot of the pulse (see Fig. 15) which was caused by increasing the filtering on lower frequencies to get rid of noise existing at the South Pole.

The 'A' pulse is split in two pulses with the SWAMP fan-out, which are sent to LeCroy4413-discriminators. One of the resulting ECL pulses is fed into a Lecroy3377 TDC channel while the other is going into the trigger electronics system. Since the discriminator thresholds are common to all the 16 input channels of the 4413 module, a value of 100 mV was set, yielding $\sim 90\%$ efficiency. The high-voltage on each PM was then adjusted so that the peak amplitude of a pulse would be around 400 mV. This yielded a gain around 10^9 and voltages ~ 1700 V with an r.m.s.

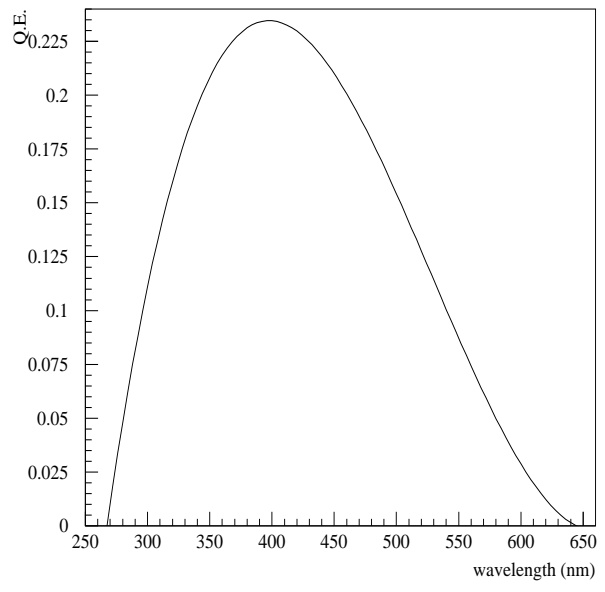


Figure 19: Quantum efficiency of the Hamamatsu tube R5912-02 as a function of wavelength. The maximum is located at 400 nm.

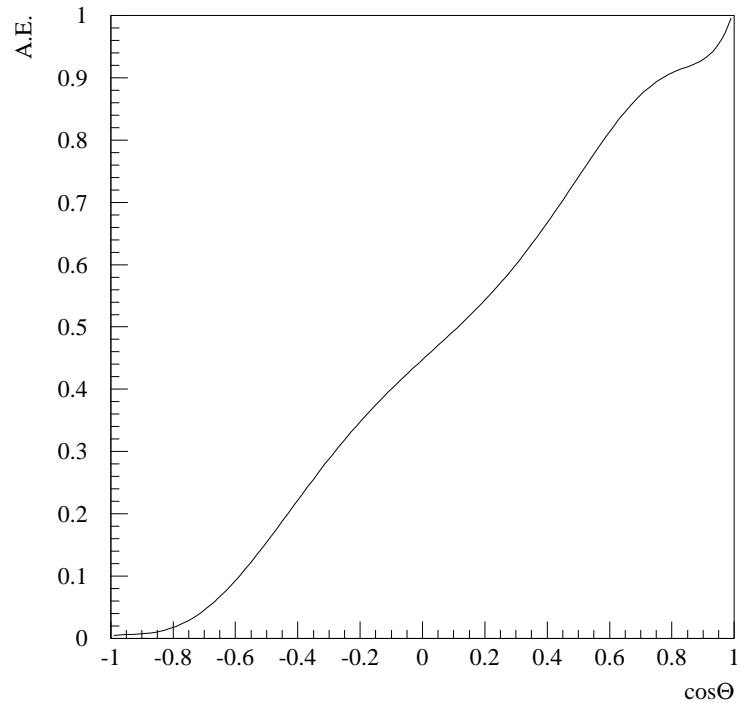


Figure 20: Angular sensitivity of a standard Hamamatsu R5912-02 photomultiplier as a function of incidence angle [40].

of 100 V over PMs. The TDC module used has 32 channels that can record at most 16 leading- (or trailing-) edge times each, with 1/2 ns resolution. It is operated in common-stop mode, registering hits occurring within a 32 μ s time-window. The Multiplicity ADDer (MADD) trigger system which takes one of the 'A' pulses is designed for the AMANDA experiment. It is housed in a 6U-Euro crate and is composed of several MULT20 modules and one ADDER device. The MULT20 makes an ECL/TTL conversion of the signals coming from the 4413 discriminator, stretching the pulse-length to the pre-set trigger window of 2 μ s. These pulses are then added and converted into a binary output which is sent to the ADDER for final adding and comparison with a given threshold. In AMANDA-B4, one MULT20 module is used for each one of the four strings, making the implementation of a majority trigger easy. The adding is made asynchronously in the MULT20 with a tree algorithm. A similar technique is used by the ADDER and the total conversion time (MULT20 + ADDER) is \sim 100 ns, with a time-jitter below 10 ns [43].

The trigger produced by the MADD system is then sent to the NIM trigger logic, which also handles trigger inputs from AMANDA-A, SPASE-1, SPASE-2 and GASP, making AMANDA-B a slave to all these experiments.

The total trigger rate during 1996 was \sim 26 Hz on average, with fluctuations of a few Hz depending on whether the coincidence experiments were on or off, changes in the electronics setup, etc. The coincidences from other experiments contributed some 4 Hz together to the total trigger rate.

Upon triggering, an ADC gate is formed, a stop signal is sent to the TDCs and a readout signal is sent to a Hytec LP1341 list processor with different delays. Then a veto lasting several microseconds is issued to the trigger, inhibiting further issuing of trigger signals. A signal is also sent out to latch a GPS time which will serve to identify coincident events with other detectors.

The noise contents of atmospheric muon events can be seen in Fig. 22, showing that the average number of PMs with a noise hit is 0.9 per muon, using a window of 32 μ s. The simulation of muons was made with the atmospheric shower program Bosiev [44], then they were propagated through the ice with MUDEDX, based on routines from [45] and passed to AMASIM [46], which simulates the detector response. After cleaning up the data, the hits which were not taken away are usually with a window of 2 μ s and the noise being flat (see Fig. 23) in the whole 32 μ s interval is reduced accordingly. The proportion of afterpulses is calculated to be 6% [47], which is lower than the figure measured in the laboratory (10%), but the comparison is not easy, since the conditions are very different (at the South Pole, 2000 m of cable were used, the voltages were set differently and the temperature is \sim -30°C – 40°C – from the deepest to the shallowest module).

The data acquisition software is written in the KMAX language and is running on a MacIntosh PowerPC 7200 communicating through a SCSI bus with the CAMAC crate-controller, a Jorway-73A. Since the access time this way is very long, a list processor LP1341 is used, to which the KMAX writes a DAQ program when starting the data-taking, and which stores the data in a 32 kB buffer after reading out the modules. This buffer is then read out in single block transfers every 600 ms by the MacIntosh. By fitting the distribution of the time Δt between consecutive events with an exponential, and comparing the integral of this fitted function with the integral of the distribution (see Fig. 24), the dead time of the DAQ can be estimated to be \sim 13%. Furthermore, the data is written directly on an NFS mounted disk, inducing further dead time [23].

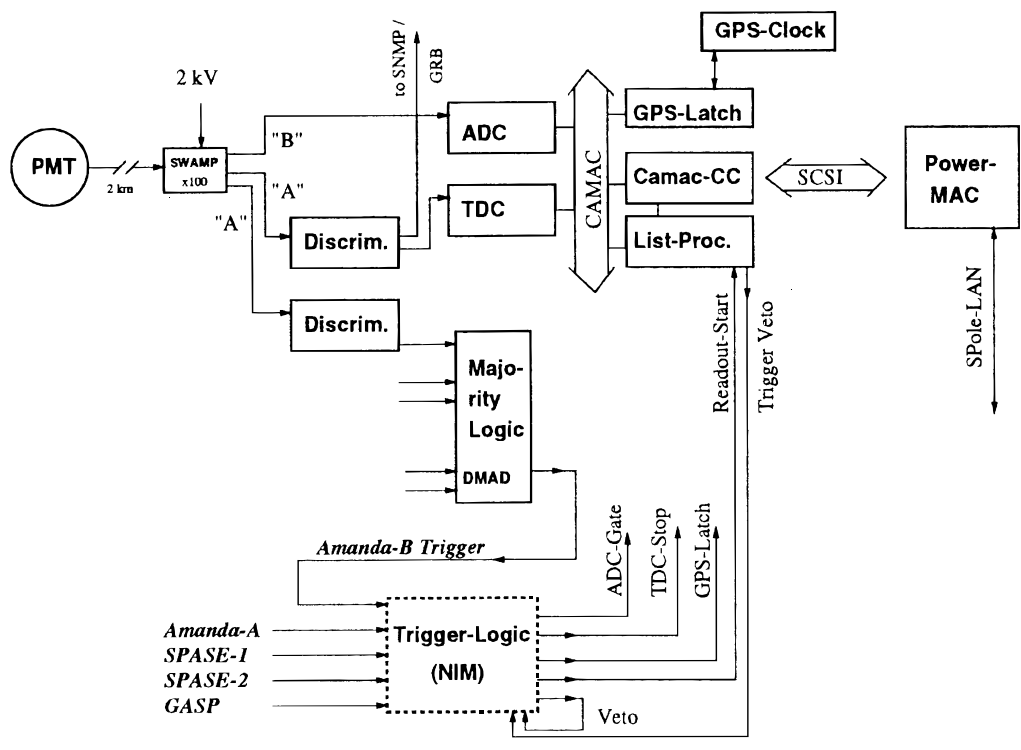


Figure 21: DAQ system used for AMANDA-B4 during 1996

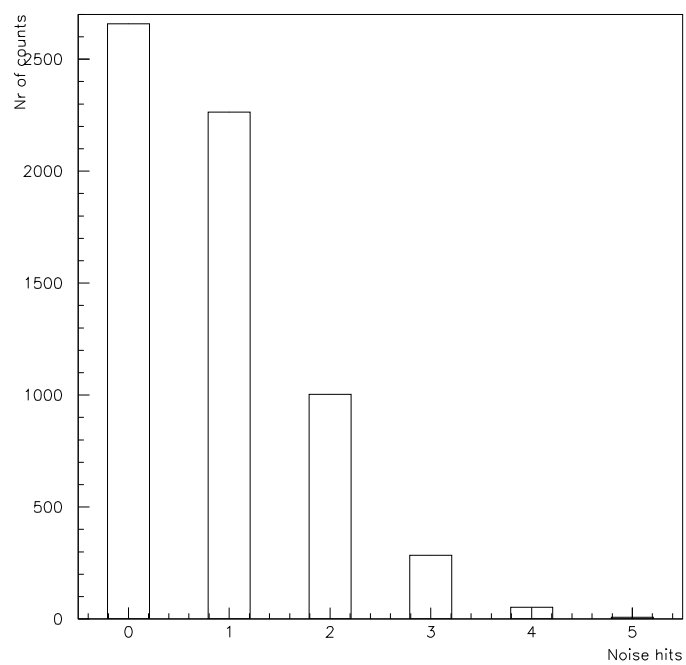


Figure 22: PM dark-noise contents of simulated atmospheric muon events. Each point shows the number of muon events with 0, 1, 2, etc. hits contributed from PM noise. The hits are collected in a 32 μs time window and a majority trigger of 8/1 is used.

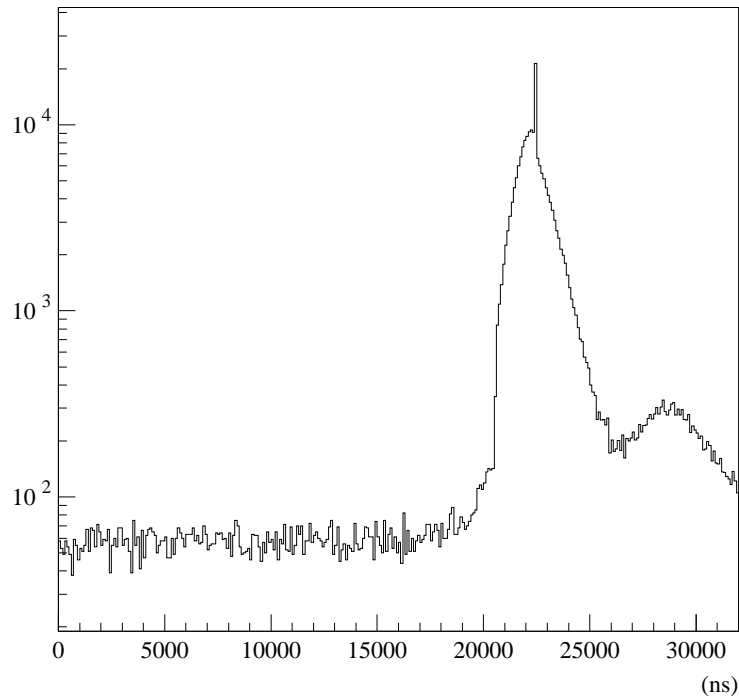


Figure 23: All leading-edge times of all modules of the array for data taken with an 8-fold majority trigger. The only cut imposed is on the time-over-thresholds ($250\text{ns} < \text{t.o.t.} < 1200\text{ns}$). The sharp peak at $23\ \mu\text{s}$ is given by the time of the eighth module hit within the $2\ \mu\text{s}$ trigger window (i.e. it is located at the upper edge of that window). Pure noise hits produce the flat distribution and the bulge after the main distribution is due to afterpulses.

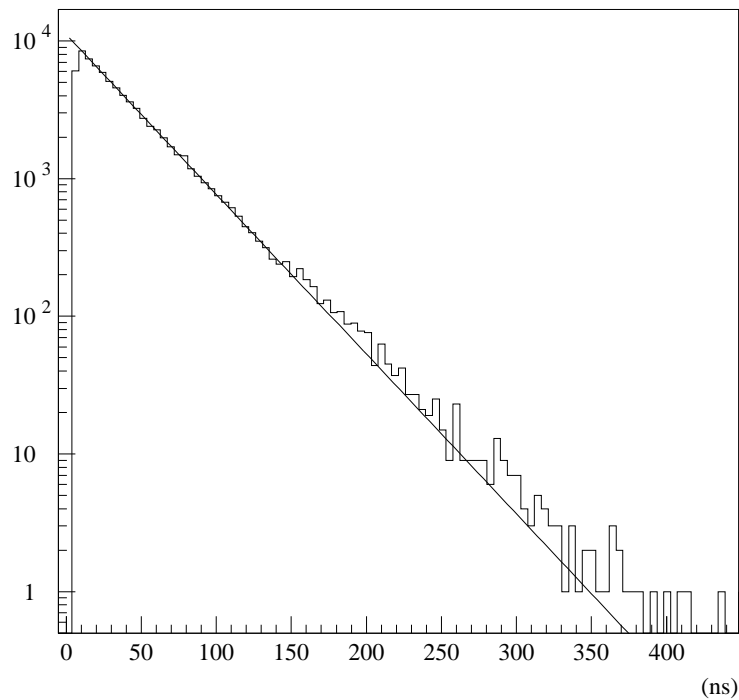


Figure 24: Distribution of the time between two consecutive events.

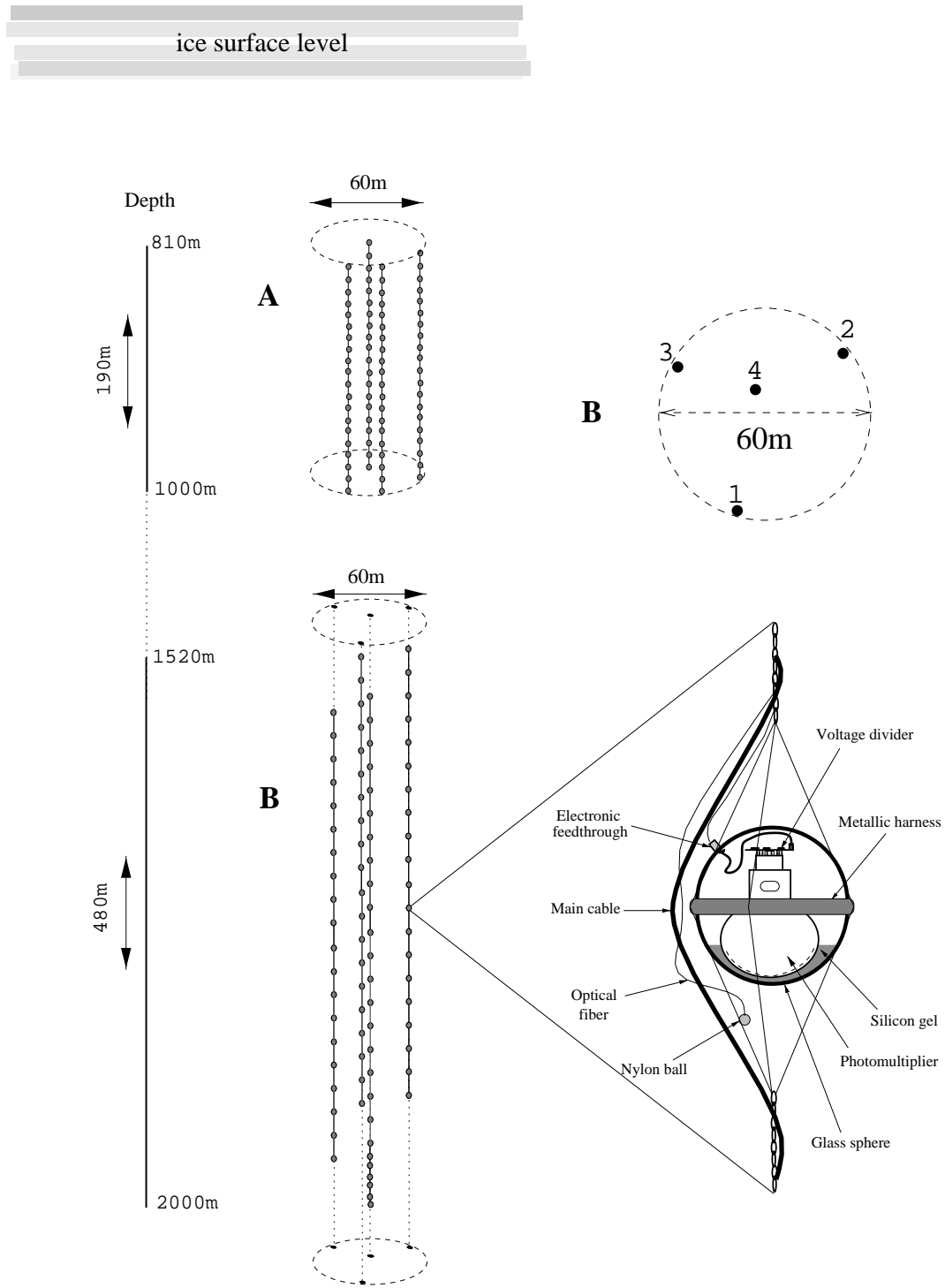


Figure 25: Geometries of the AMANDA-A and AMANDA-B4 arrays with a zoomed-in view of an optical module of the B-array.

5 Optical properties of the South Polar ice

5.1 Diffusive scattering in AMANDA-A

Several light sources have been installed in-situ in order to assess the optical properties of the glacier ice in which the different stages of the AMANDA array are deployed. One concern is that photons would get scattered on air bubbles or dust and the Cherenkov cone get deformed, another is to find which depth has the clearest ice. As air bubbles trapped in the accumulating snow get buried deeper with time, their size diminishes due to the increasing pressure. Eventually a phase transition occurs, in which hydrate crystals are formed and no bubbles can be observed [48]. Ice cores taken at the Russian Vostok Antarctic base reported bubble free ice at depths below 1280 m [49], and cores taken at Byrd station yielded bubble free ice below 1100 m [50].

Preliminary studies by AMANDA, made with a single string containing four OMs, indicated negligible scattering by air bubbles or dust in the ice at 800 m depth [51].

For AMANDA-A, measurements of time-distributions of light emitted from the sources deployed and detected by OMs further away (typically by tenths of meters) did not result in a sharp peak which would indicate clear ice. Instead, they yielded broad curves extending over several microseconds, characteristic of scattering by air bubbles (see Fig. 26) delaying the arrival times of the photons. The AMANDA-A array is located at depths between 810 m and 1000 m, with the geometry shown in Fig. 25.

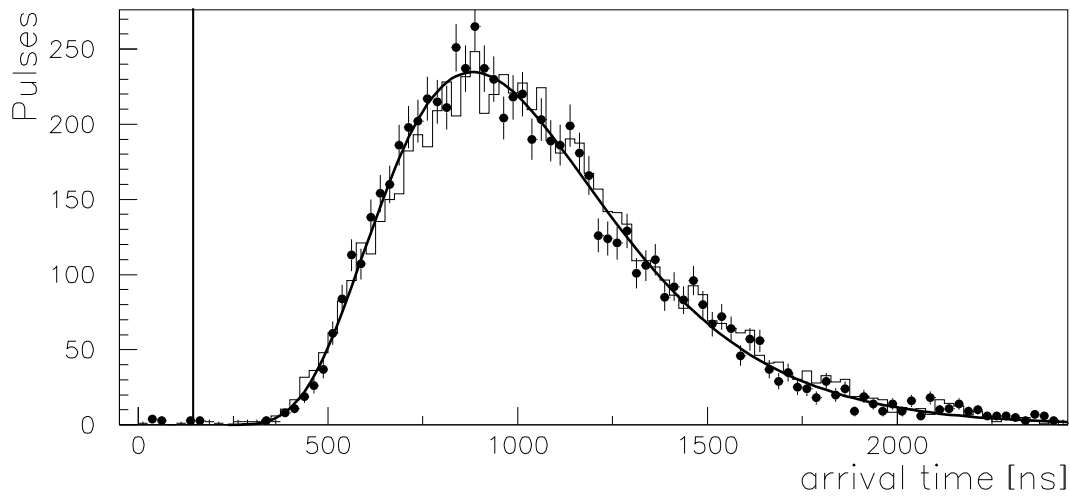


Figure 26: Arrival time distribution at an OM located 32 m away from the source. The straight line indicates where unscattered photons would have hit the cathode. The data, represented with dots, is fitted by the thick curve and the histogram represents the Monte Carlo simulation.

Since the time distributions recorded indicate that photons undergo several scatterings along their path, the situation can be best described by a random walk process [52]. The Green's function for an isotropic light source can be derived in the limiting case when the distance between emitter and receiver of light is large compared to the mean distance between scatterings (λ_{bub} in the case of bubbles):

$$\lambda_{bub} = \frac{1}{n_{bub} \langle \pi r^2 \rangle_{bub}} \quad (42)$$

where n_{bub} is the bubble density and $n_{bub} \langle \pi r^2 \rangle_{bub}$ their geometric cross section.

The probability for a photon of getting to the distance \mathbf{R} after N steps is [53]:

$$W_N(\mathbf{R}) = \frac{1}{(2\pi \langle \mathbf{R}^2 \rangle_N / 3)^{3/2}} e^{-\frac{3\mathbf{R}^2}{2\langle \mathbf{R}^2 \rangle_N}} e^{-\frac{N\lambda_{bub}}{\lambda_a}} \quad (43)$$

where

$$\langle \mathbf{R}^2 \rangle_N = \left\langle \left(\sum_{j=1}^N \mathbf{r}_j \right)^2 \right\rangle \propto 2N\lambda_{bub}^2 [1 + \tau + \tau^2 + \tau^3 + \dots + \mathcal{O}(\tau^N)] = \frac{2N\lambda_{bub}^2}{1 - \tau} \quad (44)$$

where $\tau = \langle \cos\theta \rangle$ is the average cosine of the scattering angle on a bubble, which has a value of 0.75 under the assumption of spherical bubbles.

Finally, the time distribution of an isotropic light source received at a distance d is obtained by expressing the path length as a function of time using $N\lambda_{bub} = c_i t$ and multiplying the expression given in Eq. 43 by an absorption factor $e^{-\frac{c_i t}{\lambda_a}}$ in :

$$f(d, t) = \frac{1}{(4\pi Dt)^{3/2}} e^{-\frac{d^2}{4Dt}} e^{-\frac{c_i t}{\lambda_a}} \quad (45)$$

where $D = c_i \lambda_{eff} / 3$, λ_a is the absorption length and $\lambda_{eff} = \lambda_{bub} / (1 - \tau)$ is the definition of the effective scattering length. For a more detailed discussion on the topic, see [54, 55].

A first analysis was made on data taken during the 1993-1994 austral summer season, using a laser to send pulses of light with a wavelength of 515 ± 15 nm through optical fibers ending at a diffuser near OMs. By fitting time distributions between different such emitters and receivers (OMs) with the Green's function of Eq. 45, the parameters λ_a and λ_{eff} could be extracted from the data. This procedure yielded an absorption length $\lambda_a = 59 \pm 1(stat) \pm 3(syst)$ m and a depth dependent scattering length λ_{bub} in the range 12.5-25 cm [54].

A further analysis made in the following year [56] and using 10 different wavelengths in the range 410-610 nm, exhibited the strong wavelength dependence of the absorption length shown in Fig. 27(a).

It also confirmed the depth behaviour of the scattering length (see Fig. 27(b)) observed in the previous analysis. An absorption length of 310 m at 380 nm could also be deduced using the Cherenkov light from atmospheric muons and comparing data time distributions with Monte Carlo simulation results [57]. The measured absorption lengths were longer than previous measurements made on ice in the laboratory [58, 59], which can be explained by higher concentrations of impurities in the preparations.

Eq. 45 is the Green's function for the ideal case when at most one photon reaches the photocathode where it produces a photoelectron. In reality, a large number of photons are emitted in a laser pulse, out of which several can reach the receiving OM. Each of these photons is following the Green's function, but the times recorded are those of the first leading edge of the first photon hitting the cathode. This biases the recorded time distributions towards smaller time values. In order to select distributions where this effect is small, the zero:th class of the Poisson probability distribution for photoelectrons was computed as:

$$P(0) = \frac{N_0 - N_{trig}}{N_0} \quad (46)$$

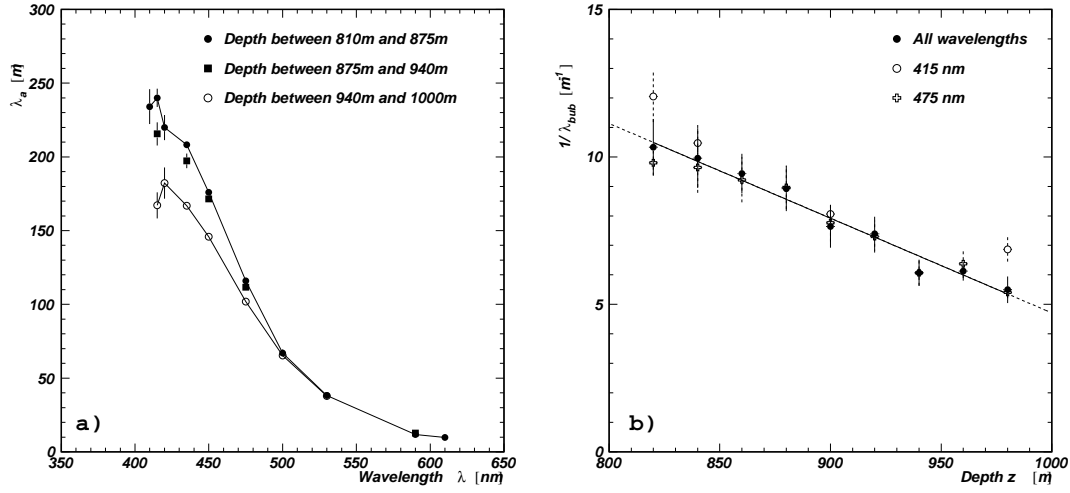


Figure 27: a) Absorption length as a function of wavelength for various depth ranges in AMANDA-A. b) Inverse scattering length as a function of depth.

where N_{trig} is the number of triggers recorded during a data-taking session and N_0 the number of light pulses that were emitted at the source. The expected number μ of p.e.'s is then trivially found from the identification:

$$P(0) = e^{-\mu} \Rightarrow \mu = -\ln\left(1 - \frac{N_{\text{trig}}}{N_0}\right) \quad (47)$$

and only distributions with $\mu < 0.01$ were chosen for the analysis ($\mu < 0.06$ for the first analysis), ensuring that the bulk of the hits were single photoelectrons. The effect of multi-photoelectrons at those intensity levels was included in Monte Carlo simulations and the induced systematic errors checked [56].

Distributions produced by using a higher light intensity can also be described analytically. Given a Green function $f(t)$, the probability that a photon would not arrive before a given time t is $Q(t) = 1 - F(t)$ with:

$$F(t) = \int_{t_0}^t f(t') dt' \quad (48)$$

which is the cumulative of f .

The probability that the earliest of n photons would arrive in a time within the interval $[t; t + dt]$ is then:

$$n \cdot f(t) dt \cdot Q(t)^{n-1} \quad (49)$$

where the factor n expresses that any of the photons can be chosen as the earliest and $Q(t)^{n-1}$ is the probability that the $(n - 1)$ remaining photons do reach the receiver later than t . Assuming that the number of photons is Poisson distributed with an expectation value γ , we can weight Eq. 49 accordingly and sum that expression over all $n \geq 1$:

$$\sum_{n=1}^{\infty} \frac{\gamma^n e^{-\gamma}}{n!} n \cdot Q(t)^{n-1} \cdot f(t) dt = \gamma e^{-\gamma} \cdot e^{\gamma Q(t)} \cdot f(t) dt = \gamma e^{-\gamma F(t)} \cdot f(t) dt \quad (50)$$

But the expression in Eq. 50 does not correspond to a properly normalized probability distribution. Integrating the formula over all t 's yields the normalization:

$$\int_{t_0}^{\infty} \gamma e^{-\gamma F(t)} \cdot f(t) dt = \gamma \int_{F=0}^1 e^{-\gamma F} dF = \gamma \left[-\frac{e^{-\gamma F}}{\gamma} \right]_0^1 = 1 - e^{-\gamma} \quad (51)$$

and we get the properly normalized probability distribution function:

$$\frac{\gamma}{1 - e^{-\gamma}} \cdot e^{-\gamma F(t)} f(t) \quad (52)$$

Another way of reaching this result is by noticing that the derivation of the p.d.f. in Eq. 50 assumes that we actually observe a hit. Dividing it by the probability $1 - e^{-\gamma}$ to have at least one hit, we get the conditional p.d.f. in Eq. 52.

If the number of photons is Poisson distributed, then the number of photoelectrons is Poisson too [60]. In reality, the PMs record photoelectrons, so their expectation value is the number of photons hitting the cathode, times the quantum efficiency Q_{eff} of the PM. Thus, the formula in Eq. 52 can be used, replacing γ by $\mu = \gamma \cdot Q_{eff}$ and replacing f by the Green's function given by Eq. 45.

This distribution has been tested by fitting time distributions taken with high intensity pulses [23], yielding absorption and scattering lengths compatible with previous analyses. It is useful where there are no reliable measurements of hit intensities and the only data available are the hit times. An analysis of electron neutrino induced cascades in AMANDA-A has been made, making use of a more sophisticated version of Eq. 52 in a reconstructing algorithm of cascades. It resulted in limits put on the $\nu_e + \bar{\nu}_e$ flux at energies greater than 10^4 GeV [61].

5.2 The ice at AMANDA-B depths

Calibration-data from AMANDA-B4 have also been analyzed, yielding much narrower time distributions than AMANDA-A (see Fig. 28). This is in agreement with the increase in scattering length with depth measured in AMANDA-A. Indeed, by extrapolating the curve in Fig. 27 to 0, the disappearance of air bubbles can be predicted below ~ 1200 m, whereas the shallowest AMANDA-B4 modules is located at 1520 m depth. The remaining time delays in the distributions are believed to be caused by scattering on dust particles. Preliminary Monte Carlo simulation comparisons indicated a scattering length so long that the assumption of diffusion could not hold anymore. A Green's function could not be derived for the range of optical parameters, where $\lambda_{eff} \approx 25$ m (i.e. of the order of the distance between strings) and $\lambda_a \approx 100$ m. Instead of relying on an analytical formula, the optical parameters of the ice between 1520-2000 m had to be extracted from the data by fitting distributions with different absorption and scattering lengths to it. Two statistical methods were used: the Kolmogorov-Smirnov test and a straightforward χ^2 -minimization. The first yielded $\lambda_{eff} \approx 23$ m and $\lambda_a \approx 100$ m using both calibration data taken with the 337 nm N_2 -laser module from UCB at 1830 m depth and light sent from a YAG-laser from the surface through optical fibers ending at different levels, assuming an isotropic light source in both cases. In the latter, pulses of light in the range 475-515 nm could be produced in situ.

The second method was applied on the N_2 -laser module data, with the improvement that the source was simulated more correctly, as a $\cos\theta$ distribution covering 2π sr and pointing upward [63]. The orientation of the receiving OM was also taken into account. An example of such

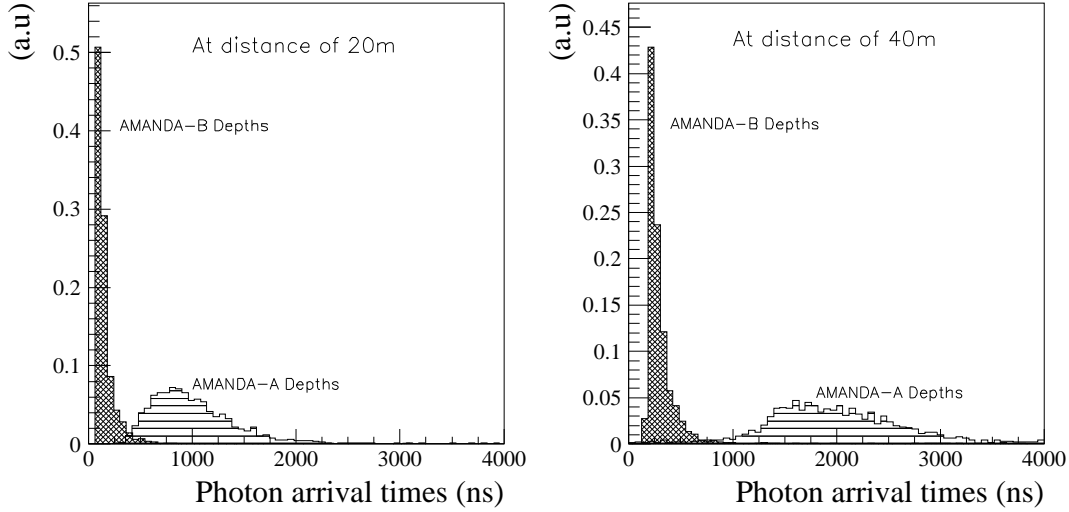


Figure 28: Time distributions at 20 m and 40 m separation between light source and receiving optical module. At AMANDA-B depths, the distributions are markedly more peaked than at AMANDA-A depths, indicating less scattering [62].

a fit is shown in Fig. 29, yielding $\lambda_{eff} = 23.9 \pm 0.6$ m and $\lambda_a = 88.8 \pm 3.2$ m. The wavelength dependence of the absorption length derived with this method, is shown in Fig. 31. A value of $\langle \cos\theta \rangle = 0.8$ was assumed and varying it between 0.7-0.9 did not make a significant change in the fitted values of λ_{eff} and λ_a .

The data from the different DC sources deployed was analyzed as well, using the formula for the flux of photons at a distance d from an isotropic source of N_0 photons:

$$F(d) = \frac{N_0}{16\pi\lambda_{eff}d} e^{-\sqrt{\frac{3}{\lambda_a\lambda_{eff}}}d} \quad (53)$$

obtained from integrating Eq. 45 over times. By using receiving modules far enough from the source so that diffusion can be assumed, the function in Eq. 53 can be fitted to the number of counts for OMs at different distances from a DC lamp emitter and the attenuation length extracted:

$$L_{att} = \sqrt{\frac{3}{\lambda_a\lambda_{eff}}} \quad (54)$$

The absorption length is affecting the tail of the time distributions when using the time information, whereas the effective scattering length is affecting the location of the peak, and is believed to have a more robust estimate in that analysis. Since the two parameters λ_a and λ_{eff} are difficult to disentangle using Eq. 53, the DC lamp analysis [64] was made, assuming $\lambda_{eff} = 24$ m. The fits were made for wavelengths of 350, 380 and 450 nm and an example is shown in Fig. 30.

The absorption lengths measured, combining all analyses, are: 95 ± 5 m at 337 nm, 90-120 m between 350 nm and 480 nm, and 45 ± 10 m at 515 nm (see Fig. 31). The effective scattering length is 24 ± 2 m, yielding an attenuation length of 27-30 m.

A refractive index $n = 1.32$ throughout the analysis, but in reality, it varies slightly (between 1.31 and 1.33) in the wavelength window where the Hamamatsu photocathode is sensitive (~ 250 – 650 nm).

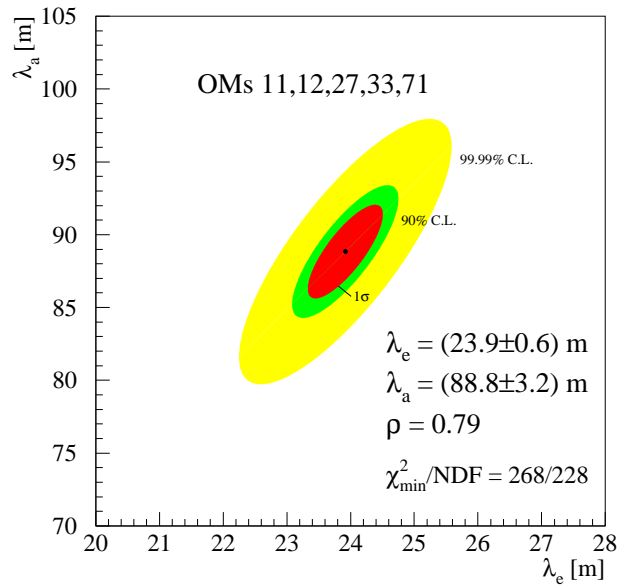


Figure 29: Contour plot of the χ^2 value yielded by comparing data time distributions with their simulated counterparts varying the parameters λ_a and λ_{eff} .

The dependence of n on wavelength can be useful for other purposes though (simulation, computation of energy loss by Cherenkov emission) and is shown in the curve in Fig. 32, taken from [65].

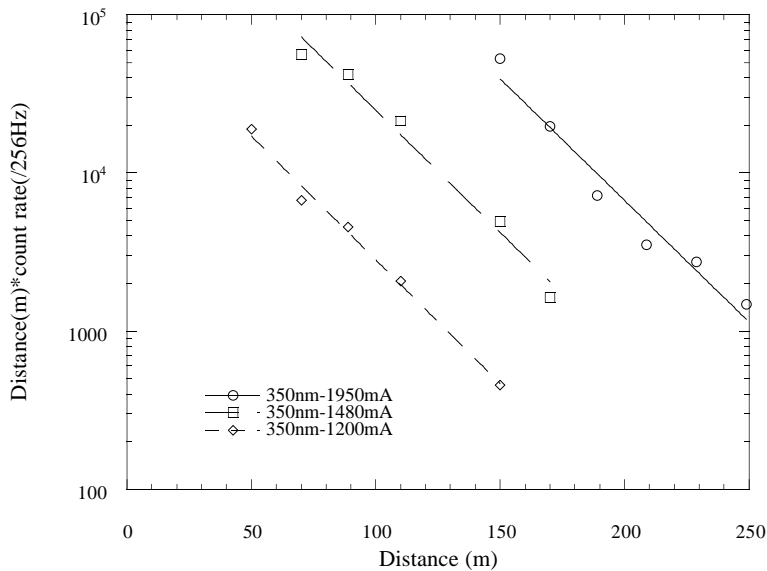


Figure 30: Distance \times counting rate versus distance for DC lamp source emitting 350 nm photons. The data-points are well fitted by an exponential, as expected from Eq. 53

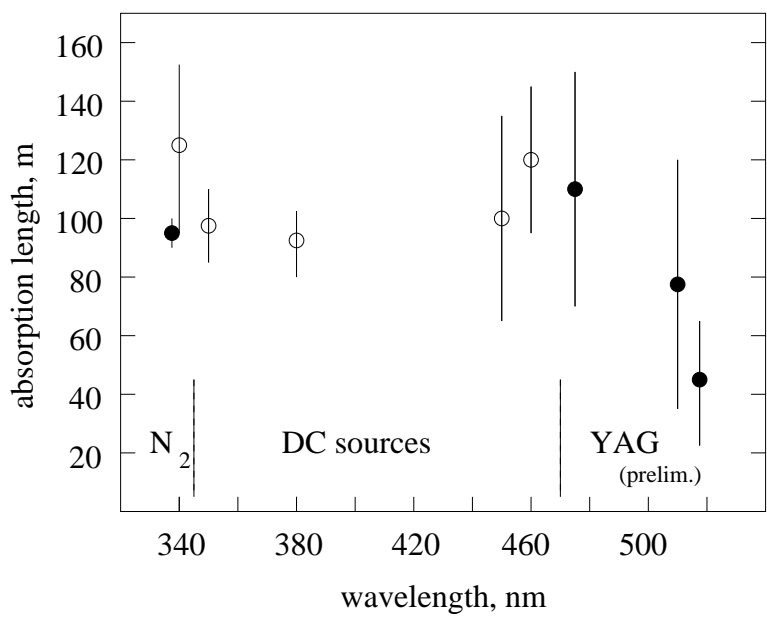


Figure 31: Absorption length measurements made at AMANDA-B depths, using various light sources and methods. The range 337-515 nm has been covered with a N_2 pulsed laser module, DC lamp sources and a YAG-laser at the surface used to send pulses through optical fibers.

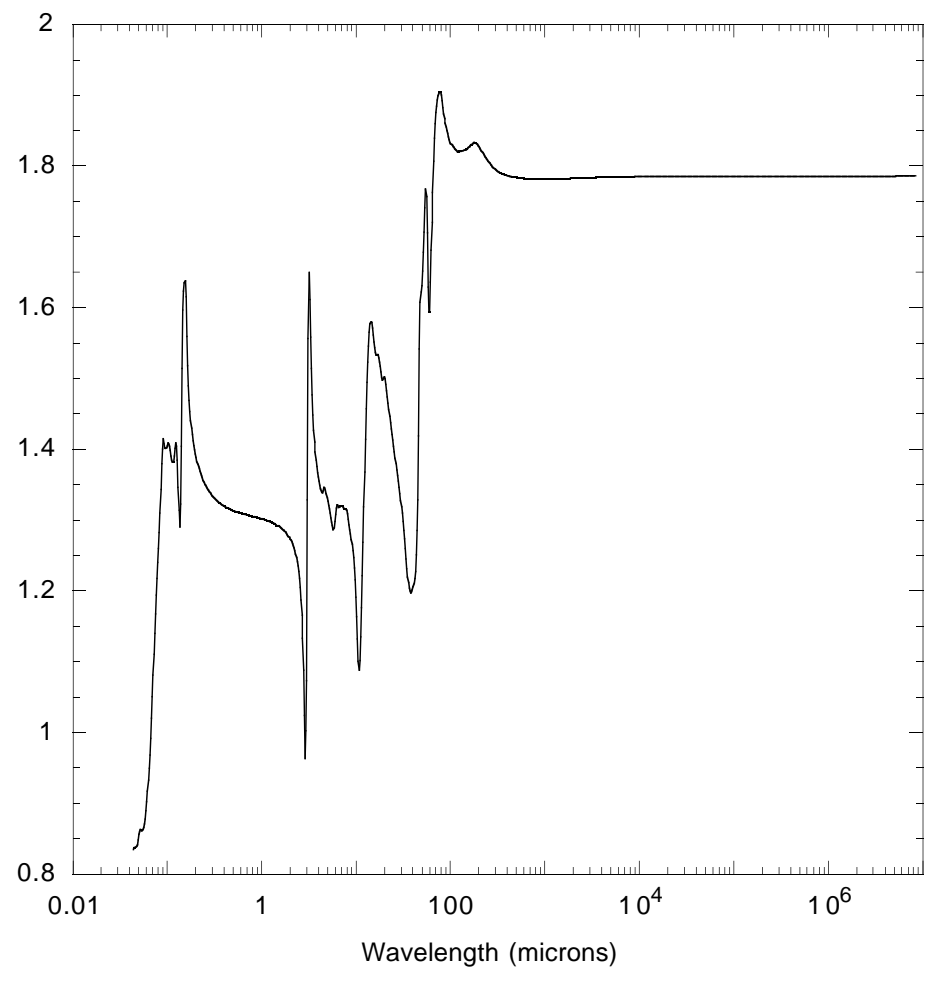


Figure 32: Refractive index of ice at different wavelengths.

6 Calibration

6.1 Time calibration

During the first calibration phase, right after deployment at the South Pole, a YAG laser was used to measure all the time delays due to different cable-lengths and transit times in the PMs (t_0s) which have to be subtracted from subsequent leading-edge measurements. An optical fiber ending at an isotropizing nylon ball right below each OM was used to send light from the surface with the YAG-laser. The data thus acquired was then used to make the in-situ time-calibration of the detector. The distance between the nylon ball and the OM is typically less than a meter (much less than one scattering length in ice), so that we can safely assume that all hits are direct (unscattered).

Since the pulses arriving at the surface have traveled through nearly 2000 meters of coaxial cable, they are very stretched, with typical t.o.t.'s of 550 ns and rise-times of 180 ns. The threshold used is set to the same value for all pulses and this means that small ones, with a slow rise-time, are measured as coming very late, compared to those with larger amplitudes.

In order to account for that effect, a correction based on the measured ADC value is used (see Eq. 55 and Fig. 34).

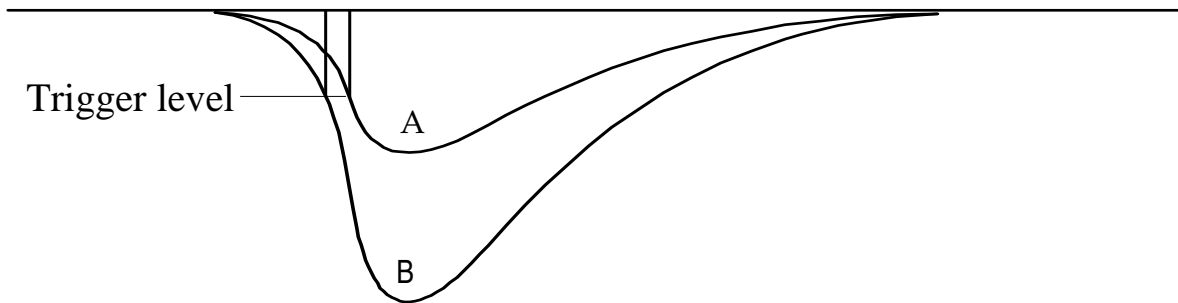


Figure 33: Time-walk due to constant level discriminator

This is the fit of the leading-edge versus ADC plots made, in order to be able to make time-walk corrections, i.e. to correct for differences in time measurements due to different pulse amplitudes (see Fig. 33):

$$\alpha/\sqrt{ADC} + C \quad (55)$$

where C is an arbitrary constant. An example of such a fit is shown in Fig. 34.

In some data-taking runs, the TDC trigger level for several of the OMs was changed; this had also to be taken into account. When the threshold on some PM was lowered from the 100 mV calibration value to a new value, the formula above had to be modified to the form:

$$\alpha/\sqrt{ADC/(0.01 \cdot x)} + C \quad (56)$$

(with x , the new threshold, in mV). However, this fit is neither good for too low ADC values, where noise becomes a concern, nor for too large values, where saturation effects enter. Light cuts can be applied on the ADC values in an off-line analysis to improve the time measurements. This way, a time resolution of ~ 5 ns is achieved at the 10^9 gain voltage at which the detector is operated for normal data-taking (see Fig. 35).

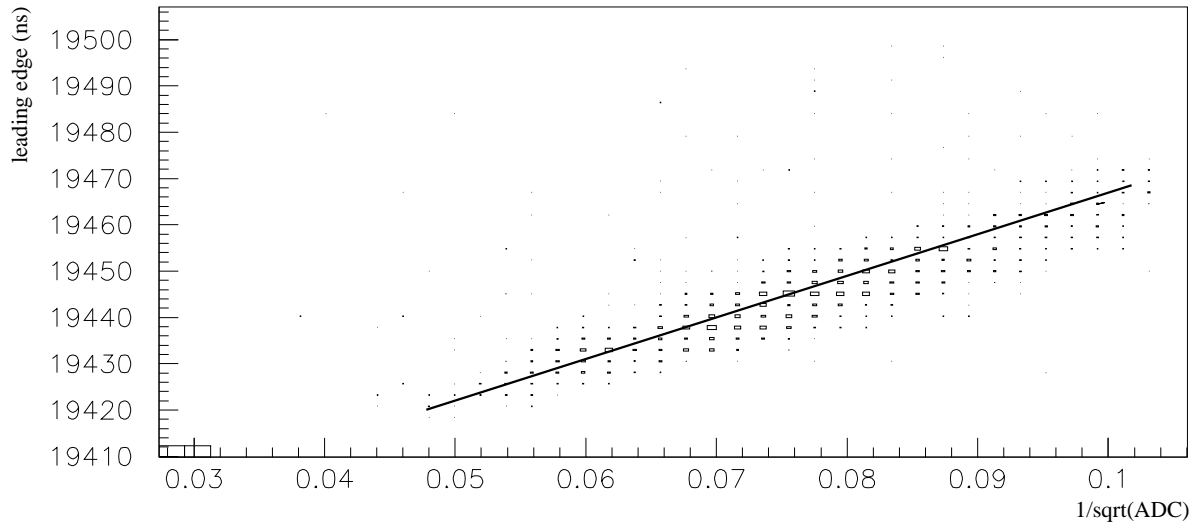


Figure 34: Example of a fitted leading edge (with $100 < \text{ADC} < 1200$) for module 19 on string 3

t_0 is another crucial parameter measured as well. It is defined as the sum of the PM's transit time at a specific voltage and of the time an unsmeared delta-pulse takes to travel through the cable. The fit in Eq. 55 is made on times including light propagation in the optical fiber. This is taken into account by measuring the fiber length with an OTDR (Optical Time Domain Reflectometer) analyzer and then subtracting the time this yields for the wavelength used, i.e. $t_0 \equiv C - t_{OTDR}$.

A calibration of the whole array was undertaken in 1996 and repeated in 1997. The standard deviation between the two t_0 -sets was 6 ns. However, studies of coincidences between AMANDA-A and AMANDA-B indicate possible errors of 15 ns on average, which could be assigned to imperfect OTDR measurements [39].

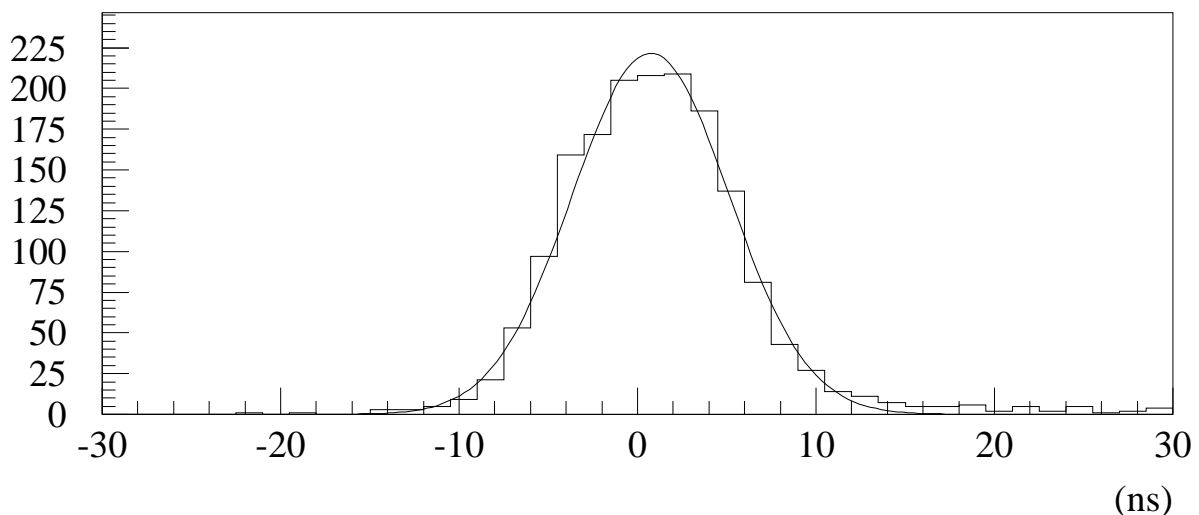


Figure 35: Residuals left from subtracting the time correction obtained with the fitted parameters for module 19 on string 3. The standard deviation is 4 ns.

That a precision of 5 ns is required for an efficient use of the detector is shown in section 9, where a comparison is made between the results of Monte Carlo simulation analyses at this measured 5 ns resolution and at 5 ns resolution with added systematic errors of ~ 15 ns resolution in each module.

6.2 Position calibration

6.2.1 Laser positioning

Measurements

In order to measure the OM positions and the ice properties, calibration data was taken while sending out light pulses with a YAG-laser at the surface. That light was led by an optical fiber to a diffusive nylon sphere right below an optical module. There were two such fibers per OM. A specific laser-module was installed 10 meters below OM16 (module 16 on string 1) for the same purpose, and a few specially designed LED modules were put at various locations inside the detector. The main goals were to study the optical properties of the ice at the depths at which the detector was buried, and — what concerns us here — to make an as accurate as possible position calibration of the detector.

The laser module contained a N_2 laser pulsed at a rate of 6 Hz, which made it possible to send light pulses strong enough to reach modules at large distances, as opposed to the surface-based sources. This laser gave a wavelength of 337 nm, for which the attenuation length in the ice is very large.

From the data taken with it, only the last three data-runs (158–160) were found to be usable, the remaining ones containing too few events.

The data-taking conditions were as follows:

- The voltage of OM16 at a gain of 10^9 is 1680 V.
- Settings (high-voltage and discriminator levels) for different runs, used in the time corrections discussed in section 6.1:

Run#	HV16 [V]	Disc. 1-16 [mV]	Disc. 17-80 [mV]	Photo-electrons
R158	800	100	100	445
R159	1300	100	100	14
R160	1200	200	100	27

Table 1: Settings for the different laser-module runs.

The intensity of the laser estimated in the last column were calculated roughly, knowing that the gain as a function of voltage (for a similar tube that had been tested in the laboratory prior to deployment) varied in the following way:

Therefore, applying a conservative estimate of the decrease in gain of 50% per 100 V, one gets the rough estimates from the ADC spectra for different runs, listed in table 1.

High Voltage [V]	Gain $\cdot 10^{-9}$
1300	0.03
1400	0.12
1500	0.27
1600	0.52
1700	1.0

Table 2: Gain for different high voltages.

Measurements were also made with the surface YAG-laser, which were carried out in the same way as those with the laser-module. In this case however, there were many emitters located at different locations in the array and many distributions for each emitter. Several different wavelengths between 465 and 545 nm were used for later use in optical properties studies, but most of the runs were made at 515 nm, including the very bright ones, especially made for geometry calibration. The pulsing rate was a bit higher (10 Hz instead of 6 Hz) and the light intensity at large distances much lower.

The data available at the end of each acquisition-run contained essentially leading-edge time, ADC(peak-sensing) and time over threshold information. The time-difference distributions yielded were compatible in features with Monte Carlo data obtained by simulating dust-contaminated ice. Assuming that some hits are direct in this scheme (i.e. that some photoelectrons were actually produced by non-scattered photons), one can get the distance between an emitter and a receiver of light by measuring the time given by the first bin in their time-difference distribution.

In principle, one could be satisfied with the method sketched above, although it uses only a minimal of information from the distribution. However, even if one did so, one should be careful not to choose a too small bin size, in order to avoid too large Poisson fluctuations, and there is always a certain level of constant noise present in the data to be concerned about. For these reasons, we chose the following slightly more complex approach:

- bin the distribution in 10 ns bins
- select distributions that have a highest bin (bin_0) with at least 50 entries and record its height ($height_0$).
- find the first bin (bin_1) that has more entries than $height_1 = height_0/10$.
- make a Gaussian fit of the distribution between the centers of bin_1 , resp. bin_0 .
- finally, find for which time the fitted function yields a value equal to $height_1$. That last step is taken in order to avoid systematic errors due to the bin size.

This method was tested on MC data and found to give different biases for different distances. It was applied on batches of 1000 events each (an example of this can be seen in Fig. 36), and the conditions used were:

- absorption length $\lambda_a = 100$ m
- scattering length $\lambda_s = 7$ m

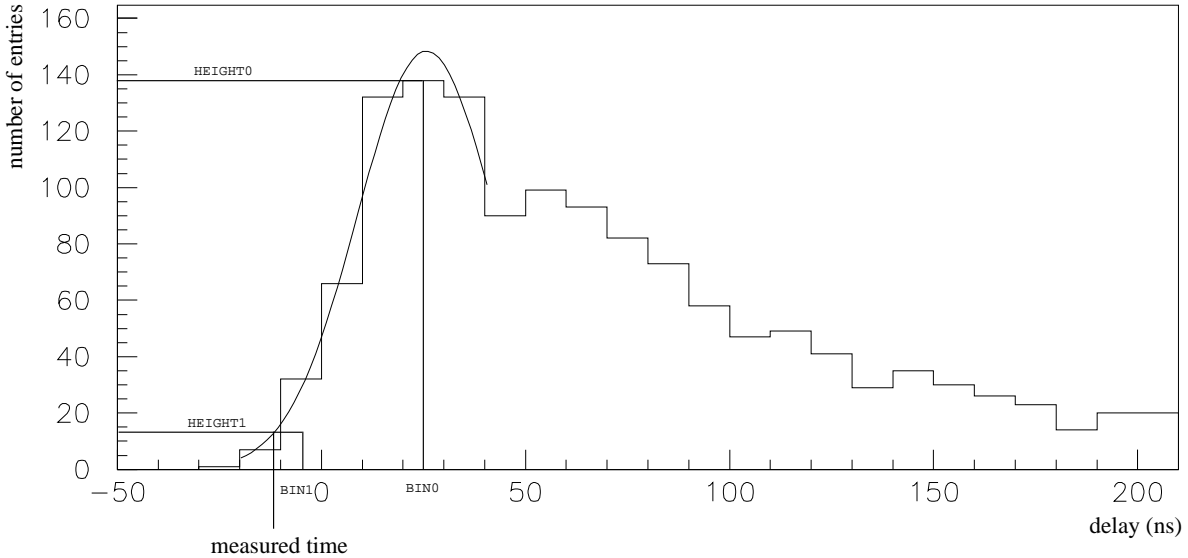


Figure 36: Time-shift measurements for a 1500 events, one p.e, 60 m distance simulated time difference distribution. A Gaussian smearing of 10 ns was applied on individual entries. Clear ice would yield a narrow peak at 0.

- average of the cosine of the scattering angle $\tau = 0.7$ implying an effective scattering length of $\lambda_{eff} = \lambda_s / (1 - \tau) = 23$ m
- each time measurement was smeared by a Gaussian function with a standard deviation σ .

The first three of these parameters were indicated by preliminary studies of the optical properties of the ice. Varying the absorption and scattering length by a few meters did not yield a significant change in results. The method was also checked on 500- and 5000-event batches and found to yield close results for the biases, but not similar statistical errors. The biases did not vary much with wavelength, so the simulations were made at a single fixed wavelength of 515 nm, although the actual data covered a frequency range from 465 nm to 545 nm for the YAG-data and were taken at 337 nm for the laser module data.

Corrections

Time corrections due to the delays induced by small amplitude pulses had to be applied, taking into account the changed thresholds (see section 6.1). We used ADC values between 100 mV and 1200 mV, for a TDC threshold set at 100 mV. For the laser-module data, different ADC cuts had to be made in order to get rid of laser-induced noise. Different runs were taken with specific light intensities, which gave a more or less Gaussian time distribution in OM16 (see Fig. 85 in the appendix), with different standard deviations.

The dynamic range of a PM is ≈ 10 photo-electrons at the 10^9 gain voltage at which it is operating for normal data-taking. In order to avoid saturating the PM closest to the light-source during the calibration phase, its gain was reduced by lowering its voltage by hundreds of volts, differently at each data-taking session. This, in turn, affected the PM's transit-time, making it significantly longer. It also degraded the total time smearing (emitter+fiber+receiver) to typically ≈ 8 ns for

YAG-data, larger than the 5 ns time resolution at the 10^9 gain voltage at which the OMs are normally operated. Laboratory measurements show that the transit-time can be assumed to increase linearly down to a level 300-400V below the 10^9 gain voltage — further down, the linearity assumption cannot be made to a good degree of accuracy (a deviation of a few ns), and a fit to a second-degree polynomial matches the relationship better (see Fig. 37).

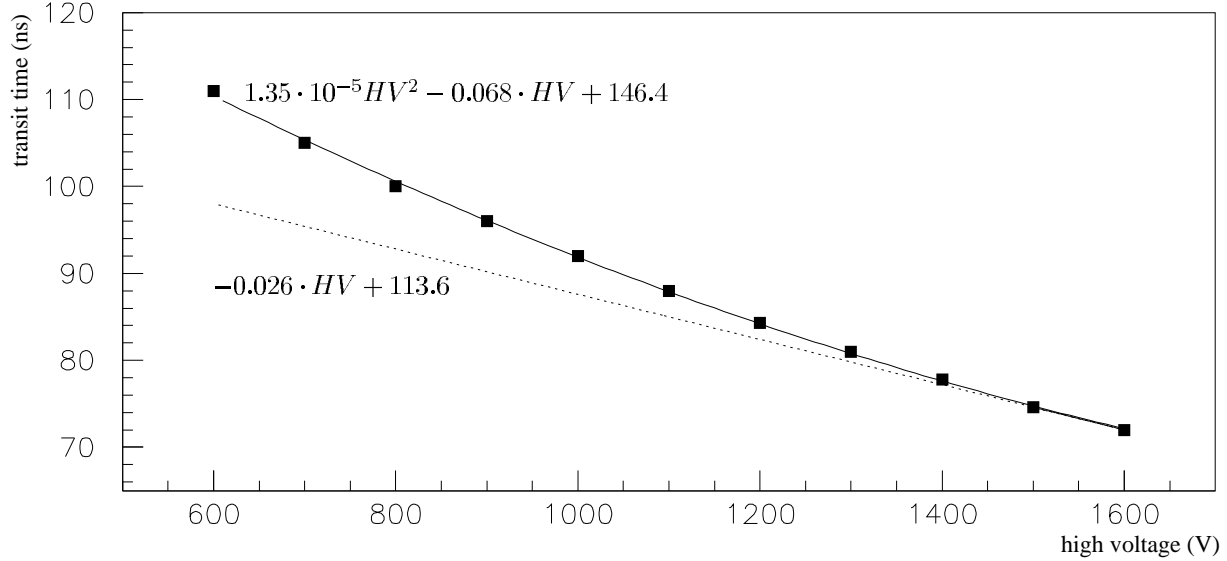


Figure 37: Lab measurement of transit time for PMT BB6308 at 50 p.e.

The difference in transit-time between individual tubes has not been estimated yet, and no *in situ* measurements of that effect have been made. We will assume that the transit-time drops by a nominal 2.6ns/100V, as a first approximation.

A further correction to that was found by shifting the intermodule distances within the emitting string, to the expected values of 20, 40, 60 m, etc. , once they were measured (see Fig. 38).

As mentioned in section 1, the time-smearing from the light source and the time-jitter of the PMs, give a bias in the measured distances. On the other hand, the scattering of light gives a bias in the opposite direction since it flattens the time-delay distribution, pushing the measured time to higher values. The combined effect is shown in Fig. 38.

The corrections that have to be applied to leading-edge time measurements are thus summed up in the general expression:

$$t_{measured} - t_0 - \alpha / \sqrt{ADC / (0.01 \cdot x)} - dt_t - bias \quad (57)$$

with :

- x : the threshold in [mV]
- t_0 : cable length + transit time
- $\alpha / \sqrt{ADC / (0.01 \cdot x)}$: the ADC correction for a new threshold x

- dt_i : the increase in transit time for a specific emitter at a voltage yielding a gain less than 10^9 gain.
- $bias$: MC-measured time-shift for the same distance

Note: for the data taken with light emitted from the laser module between OMs 16 and 17, there is an additional 44 ns to subtract, since the time reference in those runs is OM16, 10 m above the laser-module.

A problem that could not be solved in a thorough way is the effect of obscuration. On the one hand, each light-source is located directly below a specific OM, which should screen much of the light emitted upwards. On the other hand, the OMs below that emitter are facing down, so that most of their hits are caused by scattered photons.

Results

It would be impossible to have each OM's coordinates as free parameters in a global position-fit given the relatively modest amount of data we have. One could make the assumption that no piling up of the OMs in the holes has occurred (meaning $\Delta z =$ cable length between 2 OMs), that the holes are straight, and only keep 14 parameters to make a positioning relative to one arbitrary string:

- one string's y- and z-coordinates.
- two other strings' x-, y- and z-values
- those three strings' ϕ and θ directions relative to the fixed one's.

Unfortunately, even this left us with too many parameters for the fit to converge. So we had to try a simpler approach, and make the further assumption that all the strings were parallel. The distances were estimated by trying to find, for each emitter on a certain string, enough receivers on the other strings, so as to be able to make a graph of the inter-module distances versus depth, which could be fitted with the function:

$$f(z) = \sqrt{D^2 + (z - z_0)^2} \quad (58)$$

where D is the distance between the emitter and the receiving string in the x-y plane and z_0 the depth of the emitter measured along the receiving string, as shown in Fig. 39.

Laser-data

The resulting distances after corrections are listed in tables 22, 23, 24 in the appendix, together with the corresponding nominal distances. By 'nominal distances', we intend to mean those given by a 'nominal setup' where the inter-string distances are given by the position of the holes at the surface, and the relative depth-shifts have been estimated roughly from a first look at the data. It is summed up in table 3.

The inter-string distances and depth shifts resulting from these measurements are summarized in tables 5 and 6 (see also Fig. 86). Putting the three runs together, and making a new fit, one gets the results shown in table 4.

These figures should be better than the ones given by individual runs, not only because they

	Nominal	R158	R159	R160
d_{12}	70	79.5 ± 0.4	$72.0 \pm 1.1^*$	80.3 ± 2.4
d_{13}	60	68.2 ± 1.6	62.0 ± 2.0	70.0 ± 8.0
d_{14}	40	52.3 ± 1.7	$51.1 \pm 1.1^*$	55.0 ± 1.4
d_{23}	60			
d_{24}	40			
d_{34}	30			
z_{12}	0	-0.9 ± 1.1	$6.0 \pm 2.5^*$	-0.3 ± 6.0
z_{13}	-50	-55.5 ± 2.8	-47.0 ± 3.0	-52.7 ± 2.0
z_{14}	-30	-32.4 ± 3.4	$-33.5 \pm 2.2^*$	-31.0 ± 2.7

Table 3: Nominal setup and fit results for laser runs R158–R160 on interstring distances in xy -plane, d_{ij} (m), and depth, z_{ij} (m) (* denotes a fit with no well defined minimum)

Total R158+R159+R160	
-distance string1-string2:	78.9 ± 1.0 m
-distance string1-string3:	68.2 ± 1.0 m
-distance string1-string4:	52.6 ± 1.0 m
-depth-shift string1-string2:	-0.4 ± 2.7 m
-depth-shift string1-string3:	-53.3 ± 2.1 m
-depth-shift string1-string4:	-30.9 ± 2.0 m

Table 4: Results with all laser-module runs put together.

involve more data-points, but also because these points are distributed in a more symmetric way around the minimum. Run 159 is a typical instance of this case, with all its data-points on one the same side of the valley, as can be seen in Fig. 87 in the appendix.

Since the spreads around the mean given by the simulations were clearly underestimated, we chose to scale them up until a $\chi^2/n.d.f$ close to one was achieved. This should be kept in mind when considering the quoted errors on the fitted parameters.

YAG-data

Since the data was taken at low intensities, we had to gather measurements from runs with the same emitter in a common scatter-plot of distance vs. depth before making a fit. Doing so, we demanded that there should be at least five distance measurements at five different depths on the receiving string, and also that the minimum should be well defined (i.e. that the location of its minimum did not have to be extrapolated from data-points located exclusively on one flank of the curve). These requirements were lowered when they could not be fulfilled by any emitter for a specific pair of strings. Here, a time smearing of $\sigma = 8$ ns was used, and the smearing corrections were based upon that value.

We also added together measurements done at different depth levels, for two reasons. Firstly, even by combining runs, one was often left with only three degrees of freedom to fit. And secondly, because, with more data-points involved, some measurements that were strikingly off

from the others were more easily found and removed from the fit.

Summary

From these results we can deduce the results shown in tables 5 and 6:

Distances (in m) between emitters (rows) and receivers (columns)				
String#	1	2	3	4
1	-	79.8 ± 0.7	68.3 ± 0.7	54.8 ± 0.6
(laser-module)	-	78.9 ± 1.0	68.2 ± 1.0	52.6 ± 1.0
2	75.3 ± 1.3	-	59.8 ± 0.9	32.6 ± 0.4
3	64.0 ± 0.9	61.7 ± 0.6	-	31.4 ± 0.5
4	47.2 ± 0.5	36.5 ± 0.4	32.5 ± 0.4	-

Table 5: Inter-string distances given by the laser module and by the YAG laser.

Depth shifts (in m) between emitters (rows) and receivers (columns):				
String#	1	2	3	4
1	-	1.9 ± 1.9	-49.8 ± 1.4	-28.7 ± 1.2
(laser-module)	-	-0.4 ± 2.7	-53.3 ± 2.1	-30.9 ± 2.0
2	-2.9 ± 3.9	-	-53.7 ± 2.6	-29.4 ± 0.6
3	46.2 ± 2.7	47.5 ± 1.8	-	21.3 ± 0.8
4	31.3 ± 0.9	29.4 ± 0.9	-22.2 ± 0.7	-

Table 6: Depth-shifts between strings given by the laser module and by the YAG laser.

These measurements agree within a couple of meters with the laser module data.

Then, we put the laser module and YAG measurements together and assumed reciprocity between strings. This yielded the distances:

String#	2	3	4
1	77.6 ± 0.7	67.3 ± 0.7	50.0 ± 0.5
2	-	61.0 ± 0.7	36.0 ± 0.4
3	-	-	32.2 ± 0.3

Table 7: Inter-string distances obtained by combining both laser module and YAG laser results.

and the relative depths:

These fits are also shown in Fig. 92

String#	2	3	4
1	1.9 ± 1.8	-51.5 ± 1.5	-30.0 ± 1.0
2	-	-51.0 ± 2.0	-29.5 ± 0.8
3	-	-	22.0 ± 0.6

Table 8: Depth-shifts between strings obtained by combining both laser module and YAG laser results.

Estimating the errors

From the Monte Carlo simulation runs, one can readily find out what the errors ought to be. However, these seem to be underestimated in reality, since one never gets a chi-squared per degree of freedom close to unity without scaling up the error bars by a factor of typically 6.

If one compares the distance from one string to another and its reciprocal, a clear difference can be seen for, e.g., the case of strings 1 and 4. There could be several sources of error for this:

- the strings are not parallel, as was assumed. In that case, measurements made at different depths would give different inter-string distances. The fitted function itself would also be incorrect.
- the time-corrections, especially those for the transit-time, are wrong. This would strike harder if the shifted time is the emitter's, which is a reference for all receivers in a specific run.
- the modules' locations relative to the emitter and their orientations affect the time distributions more than expected, and a more detailed Monte Carlo simulation is needed to correct that effect.
- the dust-contamination of the ice is not homogeneous within the detector.
- something is wrong with the measured ice-parameters.

Comparing the distances measured between the emitter and other modules within the same string with their true values for that particular case one could get an idea of what the true errors are (yielding 2-3 m), see Fig. 38. Another rough estimation was made, looking at the distribution of the deviation between data points and the summed-up fits for YAG data, see Fig. 40. This distribution of residuals has a standard deviation of 2 m.

Putting constraints on the geometry

Since all parameters so far have been determined between pairs of strings, without considering the special geometry of the array, they can be improved by using the constraint that it gives.

There are six distances that can be measured between the detector's 4 strings. We made a general least-square estimation of the distances, using an iterative method [60]. The constraint is that the distance from string three to four should be equal to the distance between those two strings, yielded by the five remaining inter-string distances (see Fig. 41). It is introduced as a Lagrange multiplier.

The least-square sum is:

$$X^2 = (\vec{y} - \vec{\eta})^T V^{-1}(\vec{y})(\vec{y} - \vec{\eta}) \quad (59)$$

With the constraint:

$$f(\vec{\eta}) = \eta_6^2 - \left(\frac{1}{2} \frac{\eta_1^2 + \eta_3^2 - \eta_5^2}{\eta_1} - \frac{1}{2} \frac{\eta_1^2 + \eta_2^2 - \eta_4^2}{\eta_1} \right)^2 - \left(\frac{1}{2} \eta_3 \sqrt{4 - \frac{(\eta_1^2 + \eta_3^2 - \eta_5^2)^2}{\eta_1^2 \eta_3^2}} - \frac{1}{2} \eta_2 \sqrt{4 - \frac{(\eta_1^2 + \eta_2^2 - \eta_4^2)^2}{\eta_1^2 \eta_2^2}} \right)^2 = 0 \quad (60)$$

So we require:

$$X^2 - 2\lambda^T f(\vec{\eta}) = (\vec{y} - \vec{\eta})^T V^{-1}(\vec{y})(\vec{y} - \vec{\eta}) - 2\lambda^T f(\vec{\eta}) = \text{minimum} \quad (61)$$

However, the new distances resulting from this fit did not change significantly:

String#	2	3	4
1	77.4 ± 0.64	67.1 ± 0.7	50.2 ± 0.4
2	-	61.0 ± 0.6	36.1 ± 0.3
3	-	-	32.0 ± 0.3

Table 9: Inter-string distances yielded by a constrained fit.

The calculations are shown in Eq. 59 and completed with Eq. 93 for the gradient, in the appendix. From this, we can get the coordinates of the strings pinned down in an absolute reference frame by the position of hole 2 and by the angle between grid north and the axis defined by holes 2-3 (notice that this orientation is arbitrary):

String#	X [m]	Y [m]
1	-8.7	49.5
2	-24.8	-26.3
3	31.8	-4.2
4	0	0

Table 10: x- and y-coordinates of the four strings.

We had measured six depth shifts in section 4, but only three such measurements are independent. We can thus make a constrained least square fit [60] to improve the accuracy, using the linear dependency of three depths shift on the remaining ones.

This yields the following values:

These figures are compatible within two meters with the depths aimed at during deployment, as shown in table 12, listing the depth shifts between strings as computed from the cable lengths.

String#	2	3	4
1	0.2 ± 1.0	-51.5 ± 0.9	-29.5 ± 0.8
2	-	-51.7 ± 0.9	-29.7 ± 0.7
3	-	-	22.0 ± 0.6

Table 11: Depth-shifts between strings yielded by a constrained fit.

The reason for burying different strings at somewhat different depths was to increase the range in which the optical properties of the ice could be probed.

String#	2	3	4
1	0	-50	-30
2	-	-50	-30
3	-	-	20

Table 12: Depth-shifts according to cable-mark measurements.

6.2.2 Drill positioning

Another opportunity to survey the geometry of the array in a completely independent way was by monitoring the position of the drill head while going down each of the four holes.

A major advantage of this technique is that the positions it gives are relative to fixed points at the surface of the glacier ice (e.g. the points at which the holes are started) whereas a laser positioning can only yield the positions of the strings relative to each others. However, the logging of the holes is made before deployment and thus the precise position of each module within the hole cannot be determined. The measured cable length can be used for that purpose, but then, possible stacking of the OMs would remain undiscovered.

The data was recorded by the drill instrumentation at each 10 cm step and contained:

- the path-length through which the drill had proceeded so far
- the value of the Earth's magnetic field as measured by a flux magnetometer
- the angles (bank and elevation) given by two perpendicular pendulums

This information made it possible to reconstruct the whole path of the drill in detail in a fixed reference frame (see [66] for the details of this analysis). Basically, a displacement vector was computed at each step and the putting together of all vectors yielded the hole profile.

	Hole 1	Hole 2	Hole 3	Hole 4
X(1500)	-2.4	-22.2	32.5	1.7
Y(1500)	51.5	-25.9	-5.5	0.1
X(1730)	-1.0	-22.0	32.6	0.
Y(1730)	50.2	-25.9	-5.0	0.
X(1900)	-2.8	-21.6	32.6	-0.9
Y(1900)	50.4	-25.8	-4.8	-1.0

Table 13: x-y coordinates of the holes at a few depths.

String#	2	3	4
1	79.1	65.5	51.6
2	-	58.4	33.8
3	-	-	31.4

Table 14: Average distance between strings, yielded by the drill-positioning.

Error estimation

A simulation of a drill-logging was made, assuming an accuracy of 0.1° for each read and resulted in a total deviation from top to bottom of 3 cm. Notice that the real data contained several reads at each 10 cm station.

A more serious source of error could have been induced by an incorrect anchoring of the drill prior to drilling. Let us assume for instance that the drill-head direction deviated by some unknown angle relative to the vertical in our reference frame. Then, the reconstructed path would be a track going away from the initial hole in one direction in the x-y plane. Or, more likely, since the drill head keeps spinning as it goes down, the hole would have seemed to have a spiraling shape, although the real path might be a straight hole, perhaps with a larger diameter. The systematic error relative to the surface position thus introduced was estimated to be of the order of two meters [66].

Results and comparisons with laser positioning

The x-y coordinates for any depth can be retrieved from the reconstructed drill-path and some values are shown table 13.

And the distances between strings (averaged over depth) are shown in table 14.

This table agrees well with table 9 within two meters, which is satisfying, given that some of the strings are not straight—an assumption of the laser analysis. Fig. 42 displays the x-y coordinates of the four strings as seen from above, exhibiting the difference between strings. A hole drilled at a slow enough pace should be very straight since the path of the drill, in the absence of any other force is pulled down by the gravitational force. Holes 2 and 3 are very straight and do not deviate markedly from their positions at the surface, whereas holes 1 and 4 have drifted away and follow a crooked path. This difference in quality of the holes is in agreement with the

experience from the field, where the drilling of holes 1 and 4 were deemed more problematic than the rest.

6.2.3 Conclusions

We have been able to make an estimation of the position of the AMANDA-B detector. However, the amount of data collected during the calibration period was not large enough to assess all the parameters.

The data was divided between different files and one distance vs. depth fit used up many runs. Many runs could not be used due to the fact that they did not contain enough data, and that there were no curves they could contribute to. The errors on the measurements were larger than expected. A simple correction of $2.6\text{ns}/100\text{V}$ accounting for the transit time change as a function of voltage was used throughout the calculations, and when that did not suffice, a correction was extracted from the data itself. The data-taking could be improved by collecting more data in each run, and by measuring the time-offset for the time-reference tube at the voltage it is set to.

Positioning is a crucial part of the detector calibration and fortunately, we have two methods of performing it. Using laser-pulses, we can determine distances between modules and thus perform a local positioning. But, to achieve an absolute positioning, we must rely on the drilling profile of the holes. This second method has very small statistical error, whereas the error using laser light is more difficult to assess. Having two completely independent methods has proved invaluable for cross-checks and to help correct mistakes. Remaining discrepancies could be eliminated by a more careful laser positioning, taking into account the angular acceptance of the PMs and the non-isotropy of the laser-module. A larger amount of data is required in order to incorporate the tilts of the strings. The knowledge acquired when calibrating the 4 first holes has led to a number of suggestions listed in [67], [66] to improve the precision. Finally, the following points could be established:

- holes 1 and 4 are shifted at the level of the modules, relative to their nominal (surface) positions.
- furthermore, these holes are slightly tilted.
- the depths aimed at during string deployment have been met correctly, as checked using laser-data.
- the x-y positions were given by the drill data-analysis, the absolute depth using measured cable lengths and the relative depths between OMs were given by the laser data-analysis.
- a conservative estimate of the precision of the positioning is 2 meters.

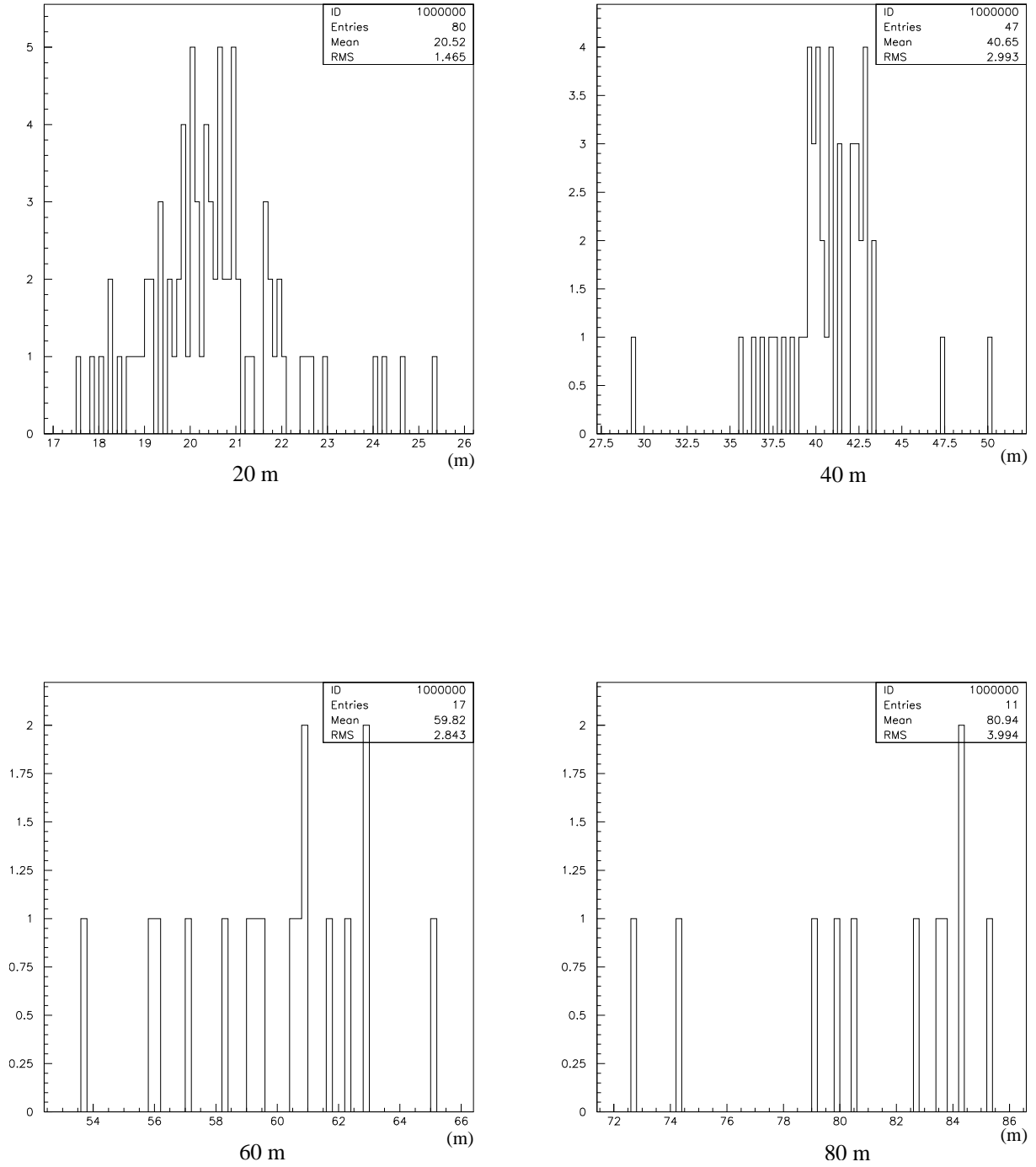


Figure 38: Distances actually measured between an emitter and modules within the same string

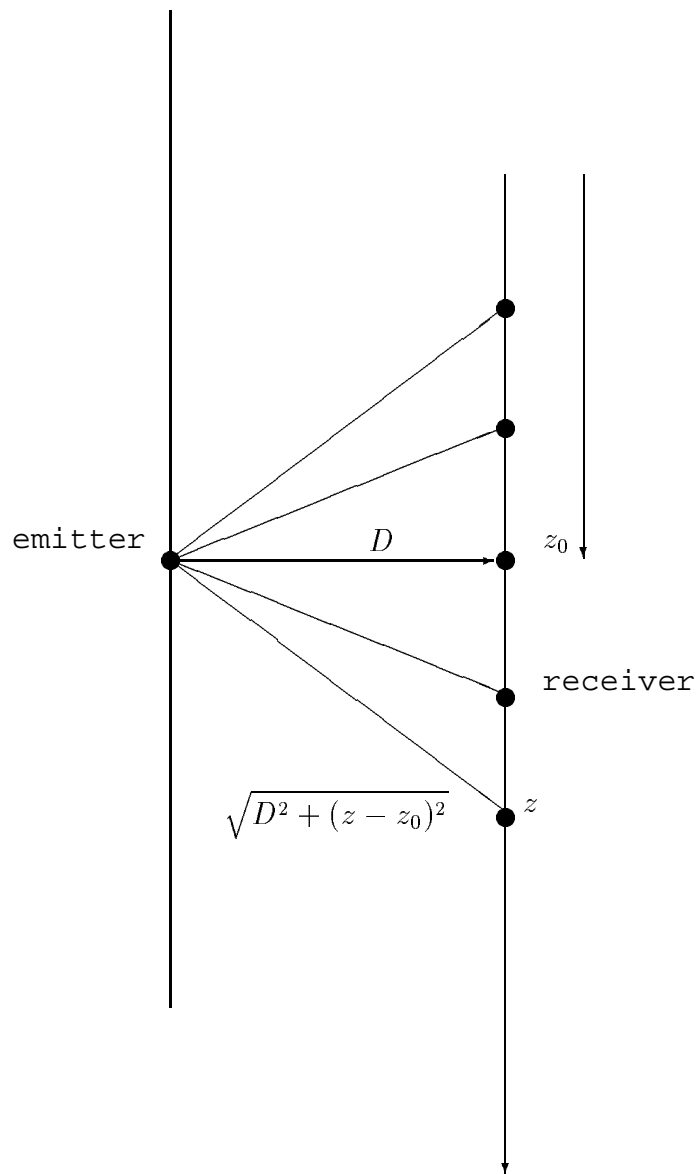


Figure 39: Schematic figure defining the parameters to be fitted

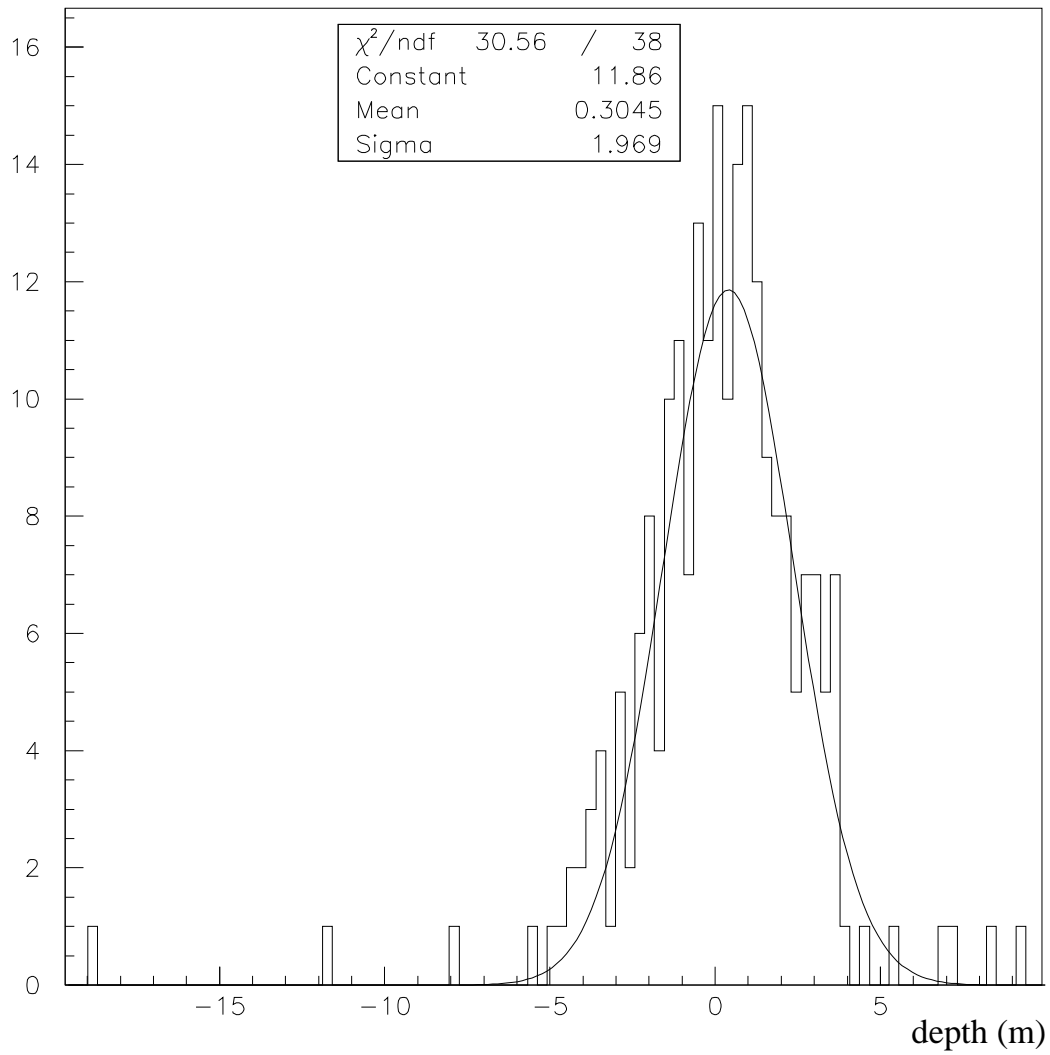


Figure 40: Distribution of the residuals of all measured distances after fitting

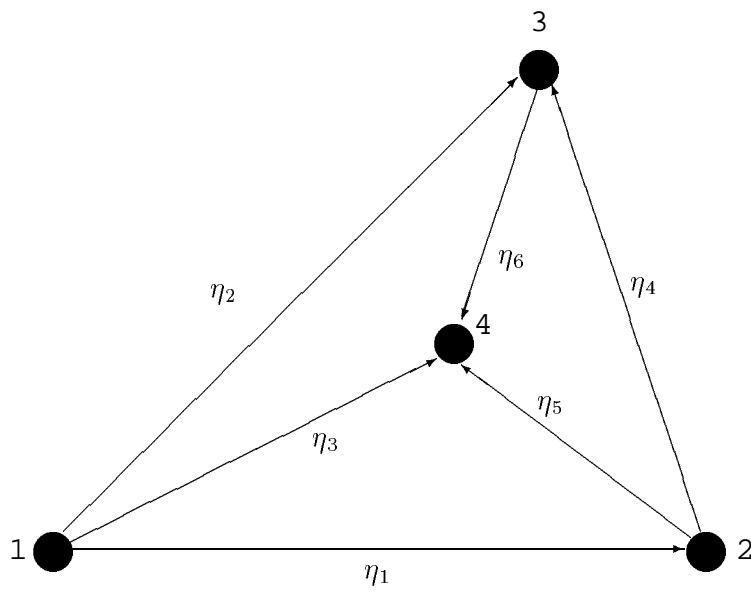


Figure 41: Top view of the AMANDA-B detector

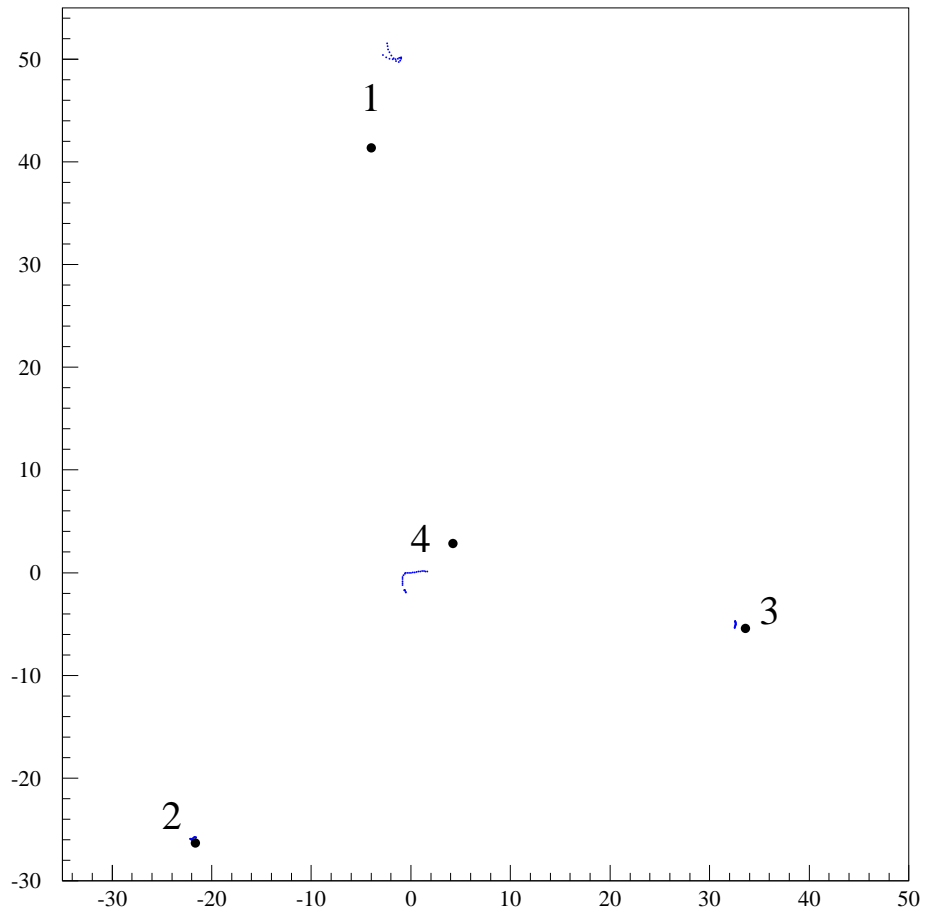


Figure 42: The AMANDA-B4 geometry seen from above. The big dots are for the position of the holes at the surface and the points are for the positions of the modules, further down.

7 Data filters

7.1 Data cleaning

The information contained in the data consists of ADC and TDC information for each hit OM, the GPS time at which the trigger was formed, the number of the channel to which the OM is connected, information about which detector gave the trigger and an ID number for each event.

For each OM, at most eight leading-edge times and eight trailing-edge times can be registered, but only one peak-ADC value. Two pulses in the same OM can yield two different times, but they must be separated by several hundred nanoseconds, since the mean time-over-threshold is 550 ns.

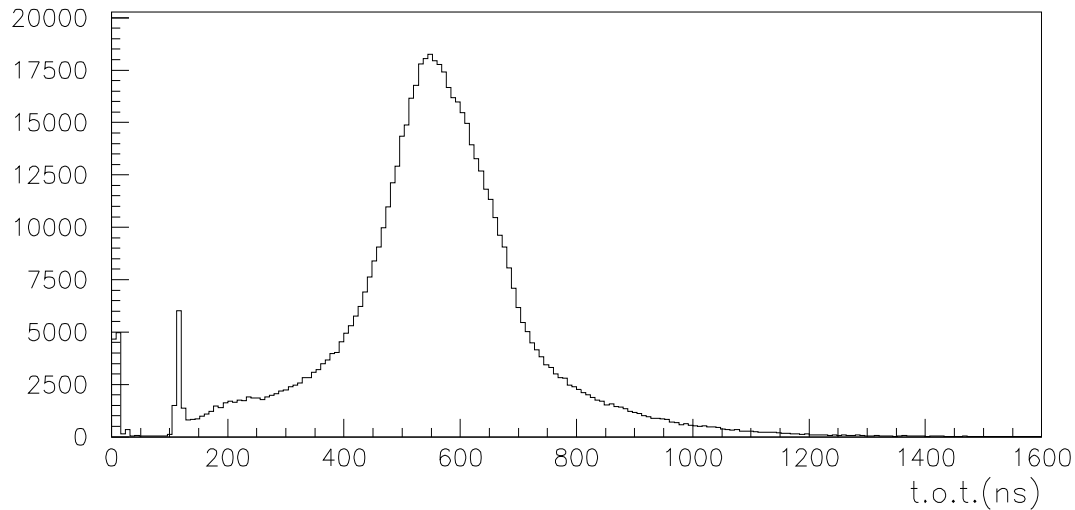


Figure 43: Time-over-threshold values before data cleaning.

The data contains unwanted hits that can be due to PM dark noise, afterpulses, late photons from secondary processes or from other muons, pulses picked up by the electronics, etc. Prior to any filtering or analysis made on an event basis, the least reliable OM information must be removed [68]. The cleaning of data can affect whole OMs, which are taken away completely from an event, or only part of the information associated to them, e.g the leading-edge time of a pulse with a very small time-over-threshold value. The first case leads to the following steps:

- The TDCs can only keep eight leading-edges per channel at most and are operated in common-stop mode. This implies that the first time would be lost if more than the maximum number separate pulses have been acquired. OMs which have registered eight pulses are discarded completely from the event.
- Some hits are registered, coming from channels connected to OMs which are known to be actually dead. This can only be due to electronics noise and those OMs are also taken away.
- Different OMs are set to slightly different high voltages, and yield different gains. After scaling the measured ADC units to p.e.'s, a cut is made at half a photo-electron level.

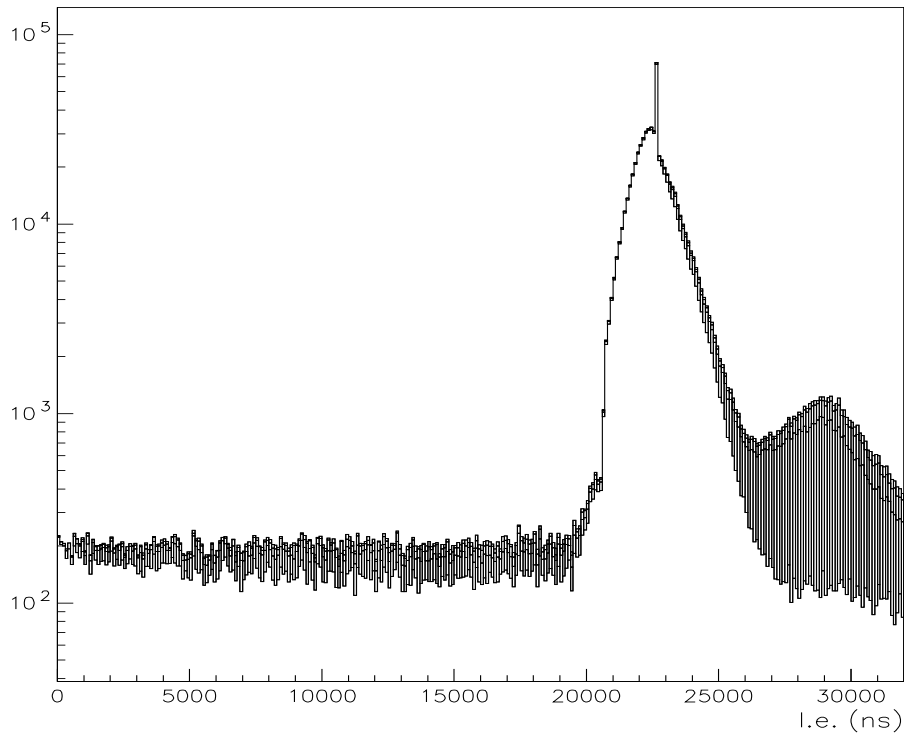


Figure 44: All leading edge times for all modules before cleaning. Contributions from l.e. times of 2nd, 3rd, etc. pulse are shown in the shaded part.

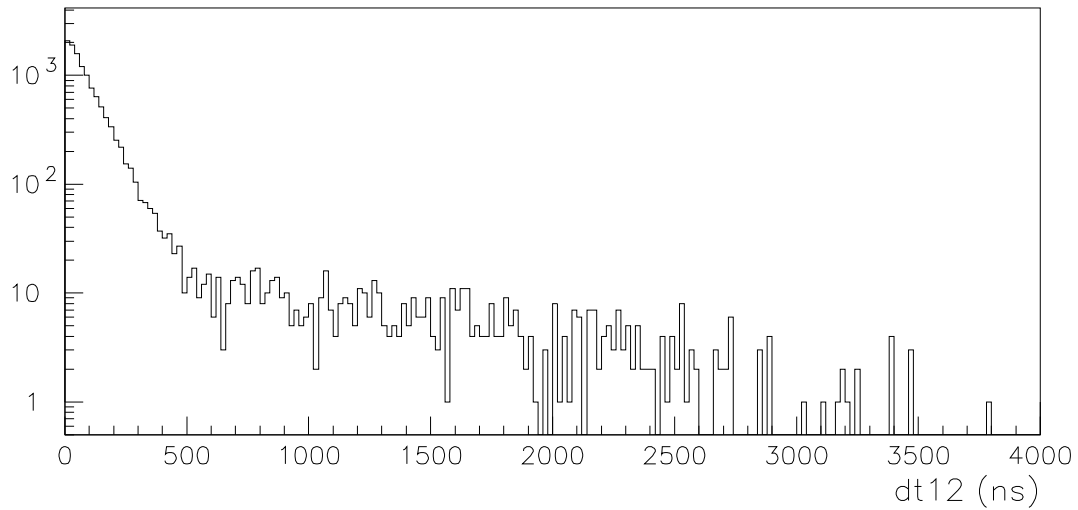


Figure 45: Time difference between the first l.e. of the first OM hit and the first l.e. of the second OM hit by a muon. Cable and transit time compensations have been applied and all cleaning routines except the last one in the list have been applied.

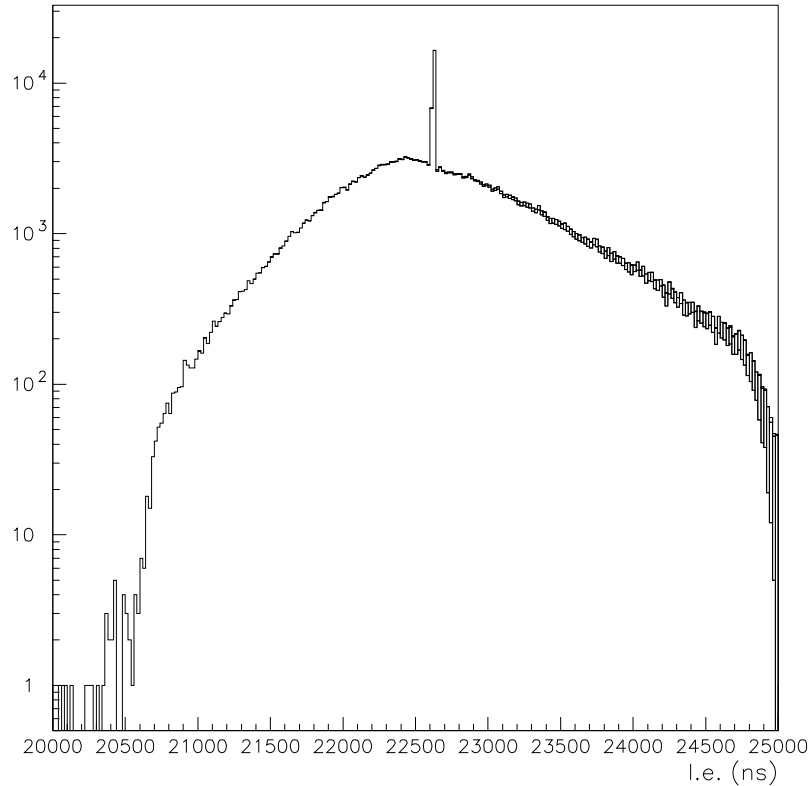


Figure 46: All leading edge times for all modules after data-cleaning. The l.e. times of 2nd, 3rd, etc. pulse are shown in grey.

In the second case, where only part of the information in an OM is considered for rejection, we may proceed along the following lines:

- Pre-pulses and electronics noise are removed by identifying pulses with time-over-threshold values either below 250 ns or above 1200 ns (see Fig. 43).
- Since the data-taking window is as large ($32 \mu\text{s}$), and a muon event is typically contained within a few microseconds, several registered pulses must be pure dark noise coming from the PMs. Fig. 44 shows all the first leading-edge times of all modules in the AMANDA-B4 array. Comparison between data and Monte Carlo simulation yields that the flat part of the distribution is constituted by dark noise. Thus, hits outside the interval 20000–25000 ns are to be removed. Most of the afterpulses (see Fig. 16, section 4) produced with \sim six microseconds delay are removed by this cut. The remaining second leading edges occur $1.2 \mu\text{s}$ after the first on average. Some afterpulsing can still be included, but at this stage, only \sim 2% of the OM's have two or more pulses left.
- The time difference (after cable time subtraction) between the first and second OM that have been hit reveal more noise. Again, comparison between Monte Carlo simulation and data shows that the flat tail in Fig. 45 is made up of PM dark noise. If the first OM's first

pulse occurs more than 600 ns before the second OM's, it is removed. The process is repeated iteratively, looping over OMs and pulses within OMs, until the time difference is less than 600 ns. A similar procedure is applied on the last and next-to-last OMs.

It is important to apply the operations mentioned above in the right order. For instance, the t.o.t.'s should preferably be cleaned before checking the time difference between the first and second OM hit, since short-pulsed noise might occur much earlier than a real pulse. Furthermore, removing enough pulses can result in the removal of the whole OM from an event. The mean event multiplicity can thus change and even drop below 8 OMs. It is 14 before cleaning of the data and 12 after. Cross-talk between channels is of no concern, since it is negligible for both the coax cable and in the SWAMPs.

7.2 Pre-filtering of events

Since the 1996 data sample totalized $4 \cdot 10^8$ events and since most of these were induced by atmospheric muons triggering the detector at ~ 26 Hz, a fast pre-filter was designed in order to reduce it to a more manageable size [39].

The limiting factors were both the storage space available and the speed of the reconstruction algorithm (a few CPU seconds on a DEC Alpha computer). Furthermore, there was little knowledge about the data at the stage at which this filter was implemented. The aim was therefore more pragmatic than just maximizing the data-reduction factor and a filter with loose cuts was best suited for our purposes.

Two samples of events were simulated to test the filter. The first was produced using atmospheric muon bundles from HEMAS (thus comparable with the bulk of the data) and the second was for a point source located at the same declination as Markarian 421.

A number of quickly computable variables were defined which either correlate with the angle of incidence of the muons or make it easy to separate single muons tracks from the downgoing multi-muon background events:

- $\cos \theta$ given by a plane-wave fit, where θ is the incident angle of the muon
- the average relative time ($t_{higher\ module} - t_{lower\ module}$) between hits in all module pairs
- the number of layers that were hit, where the 4 string array was divided into 4 layers equidistant in depth
- the number of hits per layer
- the time difference between the earliest module hit and the mean time of the deepest layer hit
- a speed variable, defined as the depth-difference between the earliest module hit and the deepest layer hit, divided by their time difference

Figs. 48, 49, 47 illustrate how these variables are distributed for an actual data-sample and for simulated samples of atmospheric multi-muons and a point source at the declination of Mrk421. The following cuts were then used to differentiate between up- and down-going events:

- $\cos \theta \geq -0.5$

- the average relative time between pairs ≥ -100 ns
- the number of layers that were hit ≥ 2
- the number of hits per layer ≥ 2
- the time difference to the deepest layer ≥ 0 ns
- the speed variable ≥ 0.25 m/ns

Applying these cuts reduced the size of the data sample to 5.2% of its original size, the simulated atmospheric muons to 4.8% and the simulated source of up-going events to 49.8%.

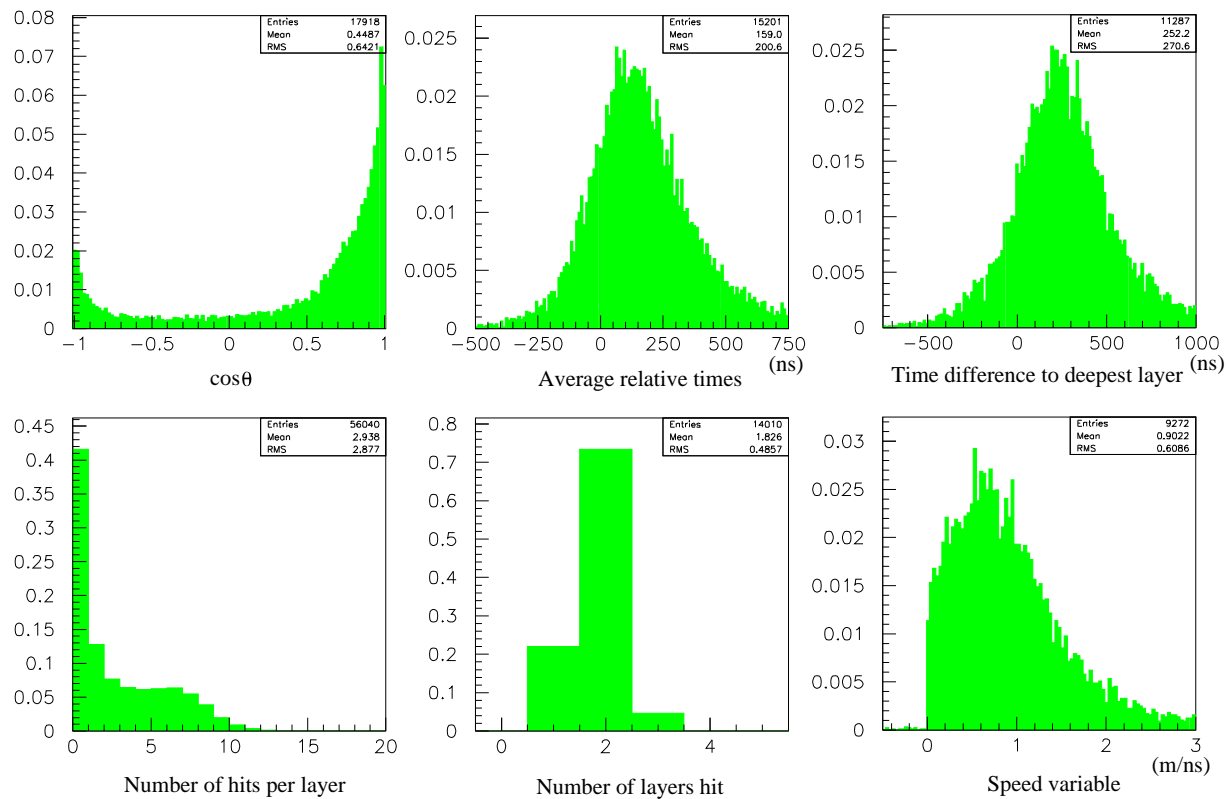


Figure 47: A simulated point source at 132° zenith angle.

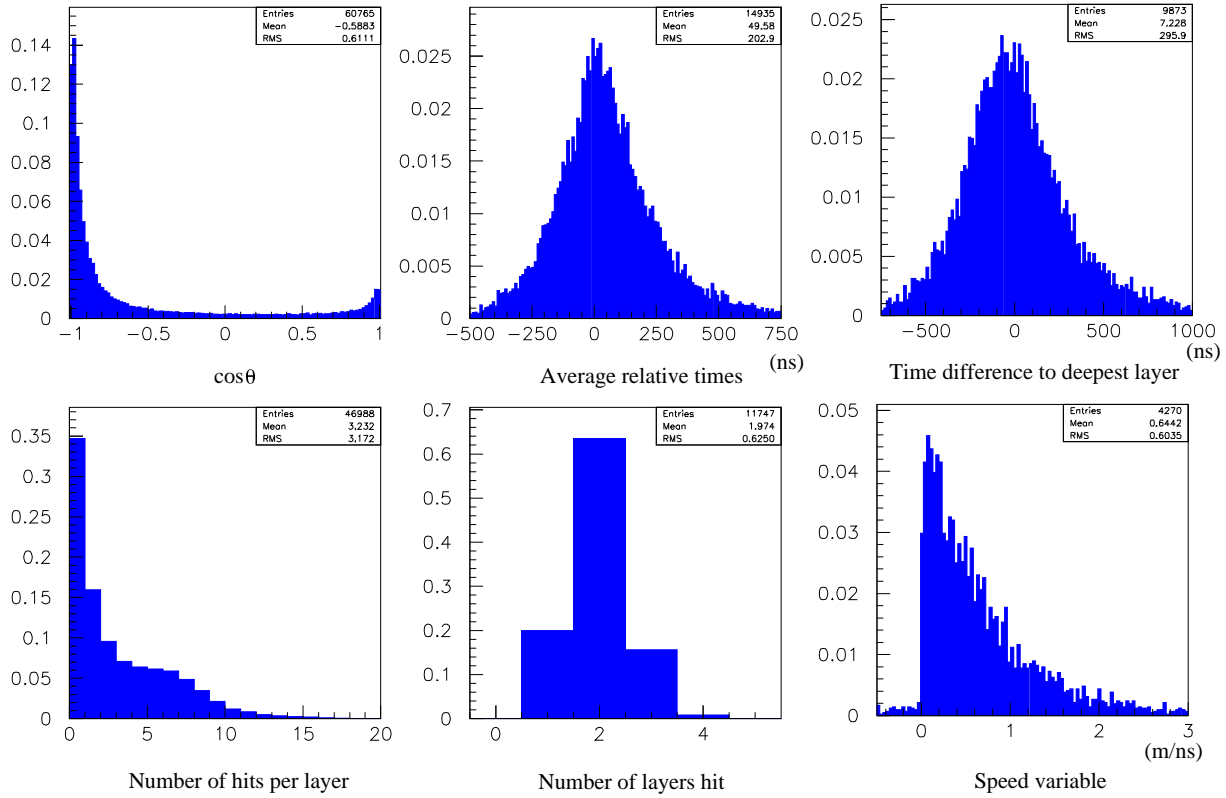


Figure 48: Distributions of the cut variables used in the pre-filter for real data.

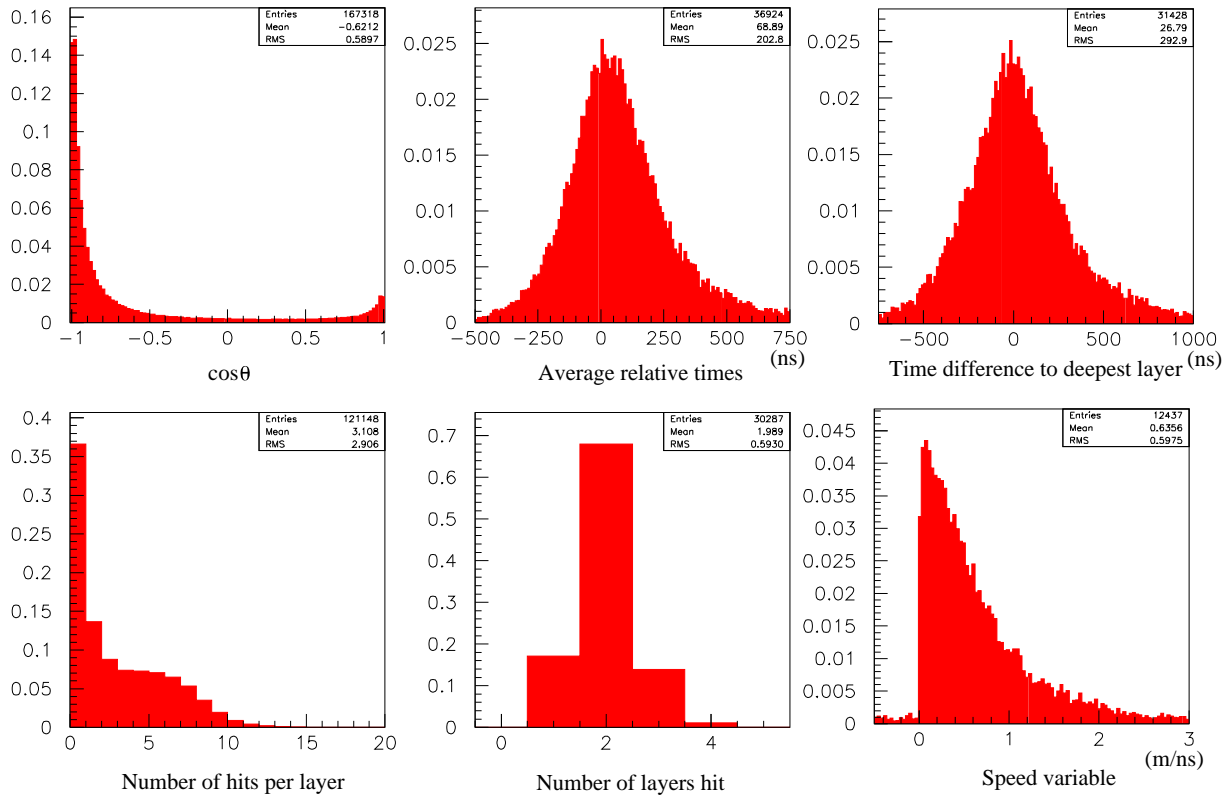


Figure 49: Simulated atmospheric multi-muon events in AMANDA-B4.

8 Reconstruction of muons-tracks

8.1 Introduction

The reconstruction of muon tracks in ice is based on the time-information left by a muon passing through the detector, close enough to several optical modules for its Cherenkov light to be detected. In order to fulfill the trigger that is set (typically, demanding that at least 8 modules should be hit and that they should be distributed over at least 1, 2 or 3 strings), the muon should be highly relativistic. A simplistic argument for this requirement is that a muon passing through ice loses ~ 0.2 GeV/m (see section 3.2) and thus needs at least an energy of 4 GeV to make it between two arbitrary modules (the spacing between neighbours on a same string being 20 m in AMANDA-B4). With a mass of 105.7 MeV/ c^2 , the muon is highly relativistic and one may safely assume the path to be straight when reconstructing it.

A straight trajectory in three-dimensional space has five degrees of freedom to be chosen (e.g. the three components of a vertex at a given time and two directional angles).

For practical implementation reasons in the reconstruction program, the parameterization chosen here was according to (see also Fig. 50):

- x_0 and y_0 , the coordinates of the track crossing the z-plane of the reference-frame.
- t_0 , the time at which the crossing occurs.
- θ and φ , the polar and azimuthal angles.

The data to which we want to fit the muon are in the form of hit-times and pulse amplitudes at different module locations. Since there is no way to know when the muon was created, these times are all relative to each other and, as a consequence, we cannot make the economy of the t_0 parameter. This is in contrast with the more robust data made up by the pulse amplitudes, which yield absolute distances to the track. Unfortunately, the number of photo-electrons is Poisson-distributed and its expectation value drops below two p.e.'s already after a few meters between OM and muon-track (see Fig. 58). Since the detector has to be operated at a one p.e. level to yield a satisfying effective area, a working implementation of a reconstruction algorithm based on that information alone is not possible. Another practical obstacle for this scheme to work is the limited dynamic range to ~ 8 -10 p.e.'s of the ADCs.

Reconstruction could be made by setting up a χ^2 function based on the time information and minimizing it with respect to the muon track parameters. However, this would be done under the assumption that the time smearing is Gaussian, which is not the case, since direct ice properties measurements have shown that there is a significant light scattering effect (see section 5.2, Fig. 28). Making this assumption would force us to keep only direct hits, clearly resulting in the rejection of a large fraction of the hits and thus of the events.

In fact, the χ^2 minimization approach would work successfully only for a near-perfect medium with hardly any scatterers, where the only time smearing would come from the time jitter of the PMs (which is indeed Gaussian).

Another and better way to fit the track parameters is to use the Maximum Likelihood (ML) method, which allows for the use of all OM hits (as shown in [69]). A good understanding of how light propagates in the ice is then required; a resulting drawback of the method is that it becomes more sensitive to the simulation implementation. For instance, the ice parameters have to be estimated correctly, as well as the angular efficiency of the modules, which might be different

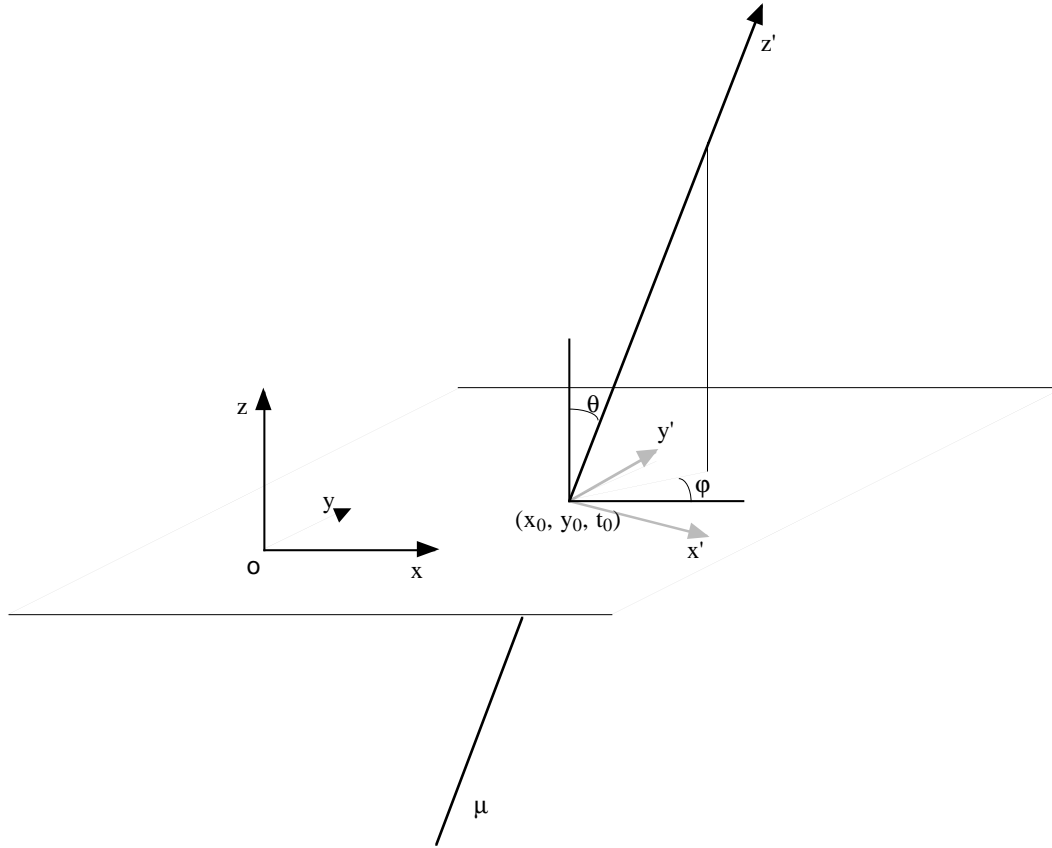


Figure 50: Coordinates used to describe a muon track in the standard reference frame of the detector

from what was measured in the lab, due to a possible accumulation of bubbles around the OMs during the re-freezing phase of the melted ice in the holes after deployment.

A likelihood function \mathcal{L} is built up with contributions from each of the N_{hits} modules that produced one photo-electron (or more) according to:

$$\mathcal{L} = \prod_{i=1}^{N_{hits}} \mathcal{L}_i \quad (62)$$

where:

$$\mathcal{L}_i = P(t_i | x_0, y_0, t_0, \varphi, \theta) \quad (63)$$

is the probability density of having a hit at time t_i for the corresponding OM (i) and the parameter estimates are yielded, according to the maximum-likelihood principle, by the minimization of the function:

$$-\log \mathcal{L} = - \sum_{i=1}^{N_{hits}} \log \mathcal{L}_i \quad (64)$$

with respect to the track parameters.

The arrival time of a Cherenkov photon emitted by a muon travelling through clear ice with a refractive index n_i can easily be computed, after transforming the OM coordinates to a reference

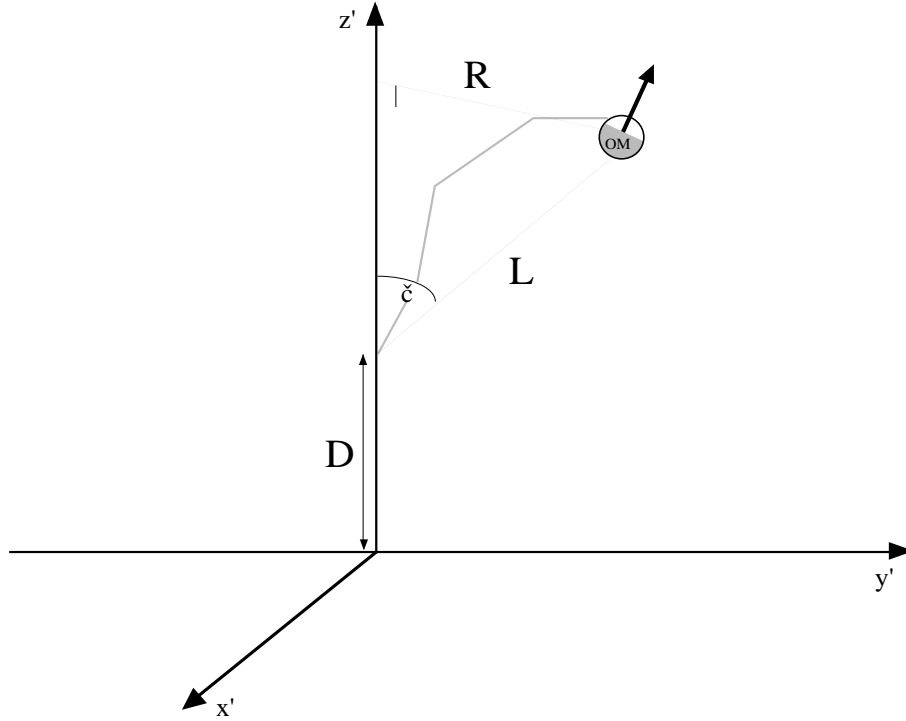


Figure 51: In a coordinate system where the muon track is used as the z-axis, the path relative to some arbitrary starting point is $D + L$ for a direct hit. If the photon has been scattered, L must be replaced by the length of the photon path (in grey).

frame where the muon starts at the origin and goes in the positive z-direction (shaded axes in Fig. 50).

Such a transformation would relate the old coordinates (x, y, z) of an OM to its new coordinates (x', y', z') through the set of equations:

$$\begin{cases} x' = (x - x_0)\cos\theta\cos\varphi + (y - y_0)\cos\theta\sin\varphi - z\sin\theta \\ y' = -(x - x_0)\sin\varphi + (y - y_0)\cos\varphi \\ z' = (x - x_0)\sin\theta\cos\varphi + (y - y_0)\sin\theta\sin\varphi + z\cos\theta \end{cases} \quad (65)$$

To compute the arrival time of an unscattered photon is then straightforward and a little bit of algebra gives:

$$t = \frac{D}{c} + \frac{L}{c_{ice}} + t_0 = \frac{1}{c} \left(z' - \frac{R}{\tan\check{c}} \right) + \frac{1}{c_{ice}} \left(\frac{R}{\cos\check{c}} \right) + t_0 \quad (66)$$

or equivalently

$$t = \frac{1}{c} \left(z' + \sqrt{(n_{ice}^2 + 1)(x'^2 + y'^2)} \right) + t_0 \quad (67)$$

where $\cos\check{c} = \frac{1}{\beta n_{ice}} = \frac{1}{1.32}$ assuming $\beta = 1$ and (x', y', z') are given by Eq. 65.

The hit-time probability distributions P used in Eq. 63 were obtained by simulating Cherenkov photons emitted by muons with infinite track length, at various positions relative to an OM's axis in order to account for the angular dependence of the PMs. An OM axis was defined as the direction for the photo-cathode peak sensitivity. Thus, the position of a track relative to an OM can be described by:

- its impact parameter (or distance of closest approach) D .
- the azimuthal and polar angles φ_{OM} and θ_{OM} defined in the coordinate system spanned by the closest-approach axis (x), the muon track (z) and a third axis (y) given by the cross product $\hat{e}_z \times \hat{e}_x$. See Fig. 52.

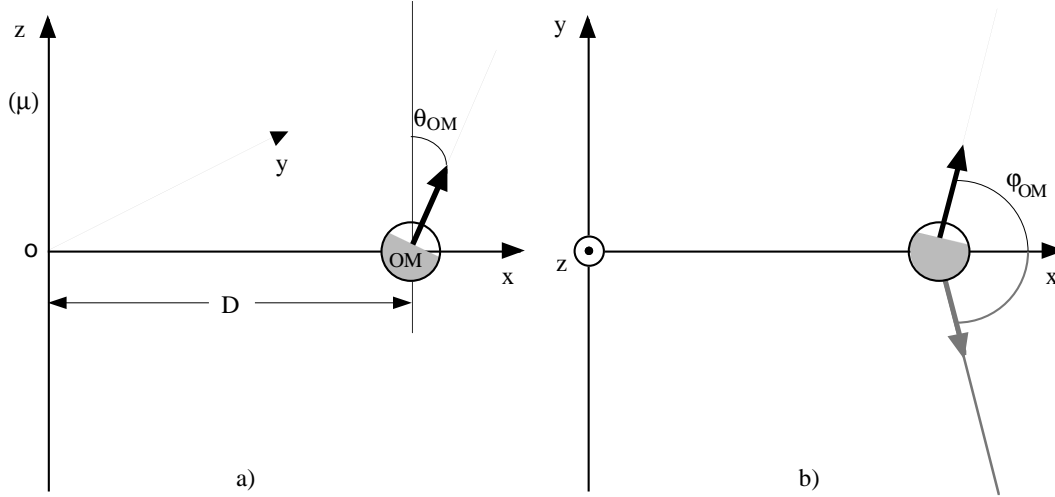


Figure 52: Parameters describing the relative positions of a muon and an OM: (a) D is the distance between them along an axis x perpendicular to the muon track and θ_{OM} is the declination angle of the OM in a right-handed coordinate system defined by the x -axis and a z -axis taken as the track itself, (b) shows how the azimuthal angle φ_{OM} is defined and the shaded projection of the OM axis illustrates the symmetry across x .

The times recorded in the simulation were the delays between the hit times of photons that had undergone scattering and the arrival time of an unscattered Cherenkov photon. The OM properties are folded into these time delay distributions, since they are for actual hits, i.e. photons that produced photoelectrons. Note that, due to scattering, photons originating from a section of the track located far away from the point given by the Cherenkov angle have also a chance of hitting the photocathode.

A Single Track REConstruction program (STREC) was written, integrating the different steps of data-cleaning, filtering and reconstruction of muon track events by the minimization of a log-likelihood function.

8.2 Time probability distribution functions

The Swedish Monte Carlo simulation program LOLITA was run to produce the data used in the following study. The optical parameters of the ice were set to the following values:

- peak-absorption length $\lambda_a = 100$ m
- scattering length $\lambda_s = 7$ m
- average of the cosine of the scattering angle $\tau = 0.7$ implying an effective scattering length of $\lambda_{eff} = \lambda_s / (1 - \tau) = 23$ m

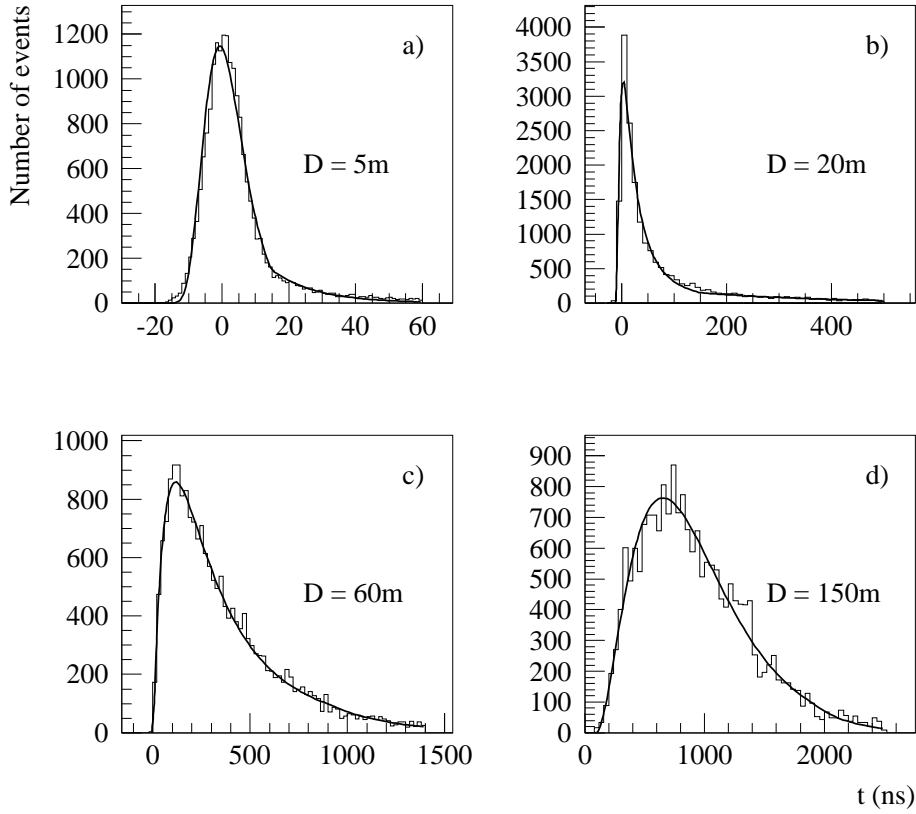


Figure 53: Fitted time-delay distributions for various impact distances. θ_{OM} is 180° in all figures or, equivalently, the muon is head-on and parallel to the OM axis. They all contain the same number (20000) of events. The time range on each plot is such that 95-97% of the distribution is contained. In (a), most of the hits are direct, which is reflected by the almost Gaussian shape, (b) is the distribution in a mode where scattering is changing the order of magnitude of the time spread, in (c) and (d), one has virtually entered the diffusion regime.

Each time measurement was smeared by a Gaussian function with a standard deviation of 5 ns.

Time delay distributions were recorded for different combination of the parameters $(D, \varphi_{OM}, \theta_{OM})$ and then stored into tables. The variable D was divided in bins of uneven size ranging from 0 to 150 meters, with a bin size increasing with larger distances —where the relative growth of the standard deviation is smaller. The angle θ_{OM} between muon and OM was evenly divided in bins of 20° . As for φ_{OM} , although it was found not to be affecting the shape of the distributions strongly, it was binned in the same way as θ_{OM} . For φ_{OM} , the reflection symmetry across the abscissa exhibited in Fig. 52 was used to reduce the amount of information by a factor of two.

Since the recorded times represented actual hits, the distributions were of photo-electrons rather than of photons. Thus, the actual result of the simulations is a convolution of photonic time distribution, Cherenkov wavelength spectrum, glass sphere transparency, PM quantum efficiency, angular and geometrical acceptance (see Fig. 53).

As the resulting histograms would have required too much space to be stored as they were, and in order to improve the speed-performance of the reconstruction program, they were fitted with analytical functions. Only the parameters of the fitted functions were kept for subsequent use in the minimization algorithm.

The spread of the time-delay distributions covers several orders of magnitudes, ranging roughly from the PM time-jitter of a few nanoseconds, to several microseconds for large values of D when the photons are in a completely diffusive regime.

A good candidate function to fit these histograms is the F-distribution. This function (with a shift in time t_s and a scale factor σ introduced) is given by:

$$f(t; t_s, \sigma, \nu_1, \nu_2) = \frac{1}{\sigma} \frac{\Gamma(\frac{\nu_1 + \nu_2}{2})}{\Gamma(\frac{\nu_1}{2})\Gamma(\frac{\nu_2}{2})} \left(\frac{\nu_1}{\nu_2}\right)^{\frac{\nu_1}{2}} \frac{(\frac{t-t_s}{\sigma})^{(\frac{\nu_1}{2}-1)}}{[1 + \frac{\nu_1}{\nu_2}(\frac{t-t_s}{\sigma})]^{(\frac{\nu_1 + \nu_2}{2})}} \quad (68)$$

(Note: the $\frac{1}{\sigma}$ -term in front of Eq. 68 is there for normalization and the parameters have no obvious physical interpretation).

It is used from some value t_s where the probability is very small, up to a fitted time t_c when the function turns into an exponential shape, after which the distributions are fitted accordingly.

This yields the function:

$$g(t; t_s, \sigma, \nu_1, \nu_2, t_c, b) = \begin{cases} Af(t; t_s, \sigma, \nu_1, \nu_2) & \text{for } t \leq t_c \\ Be^{-bt} & \text{for } t > t_c \end{cases} \quad (69)$$

which is used to fit our Monte Carlo simulation distributions.

Normalization and continuity requirements allow us to determinate A and B of equation 69, yielding:

$$g(t; t_s, \sigma, \nu_1, \nu_2, t_c, b) = \begin{cases} \frac{f(t)}{F(t_c) + f(t_c)/b} & \text{for } t \leq t_c \\ \frac{e^{-b(t-t_c)}}{F(t_c)/f(t_c) + 1/b} & \text{for } t > t_c \end{cases} \quad (70)$$

where

$$F(t; t_s, \sigma, \nu_1, \nu_2) \equiv \int_{t_s}^t f(t'; t_s, \sigma, \nu_1, \nu_2) dt' = \sigma I \left(\frac{\nu_2}{\nu_2 + \nu_1 \frac{(t-t_s)}{\sigma}}; \frac{\nu_2}{2}, \frac{\nu_1}{2} \right) \quad (71)$$

is the probability contents of the F-distribution and $I(x; \alpha, \beta)$ is the incomplete beta function:

$$I(x; \alpha, \beta) \equiv \frac{\int_s^x t^{\alpha-1} (1-t)^{\beta-1} dt}{\int_s^1 t^{\alpha-1} (1-t)^{\beta-1} dt} \quad (72)$$

The cumulative of the function g in Eq.70 is given by:

$$G(t; t_s, \sigma, \nu_1, \nu_2, t_c, b) = \begin{cases} \frac{F(t)}{F(t_c) + f(t_c)/b} & \text{for } t \leq t_c \\ \frac{F(t_c)}{F(t_c) + f(t_c)/b} + \frac{f(t_c)}{b} [1 - e^{-b(t-t_c)}] & \text{for } t > t_c \end{cases} \quad (73)$$

In spite of their somewhat intricate analytical expressions, all of the functions considered in Eqs. 68 — Eq. 73 can be computed using fast routines from e.g. [70]. For values of t less than t_s , the time probability density function (p.d.f.) g was set to to a constant level.

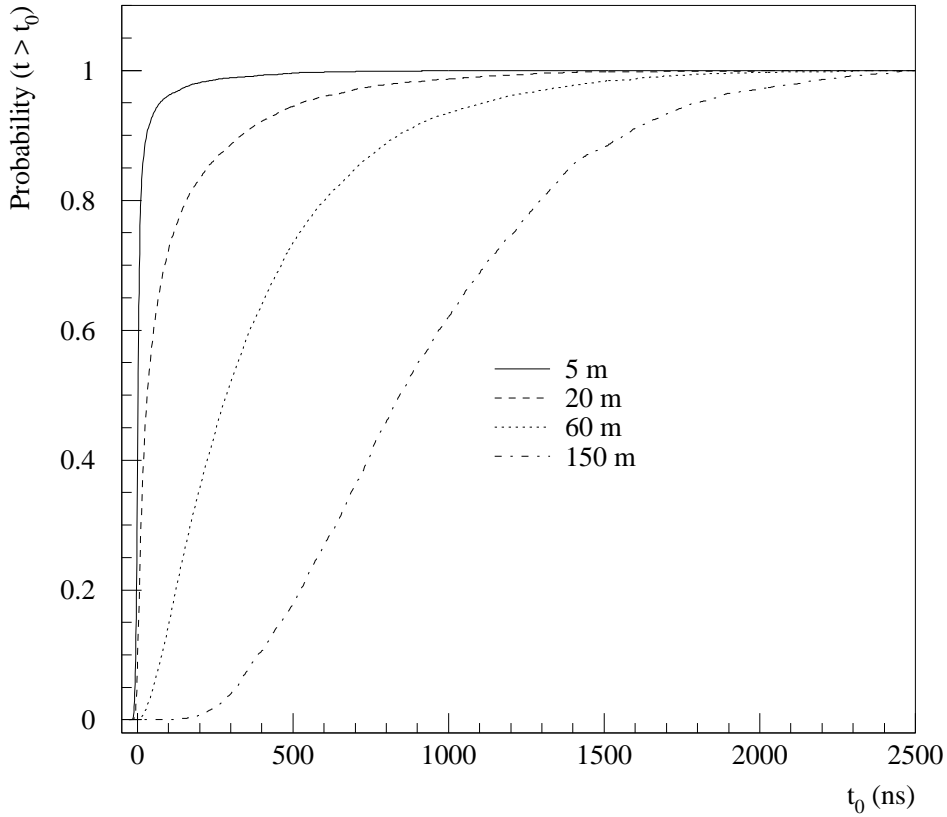


Figure 54: Cumulatives of time distributions for head-on muons for several distances.

As the distance between the muon and the OM increases, $g(t; t_s, \sigma, \nu_1, \nu_2, t_c, b)$ is moving from a regime of (nearly) direct hits to a regime of total diffusion, passing through an intermediate phase. At the one end, for the extreme case of direct hits, the delay time distribution is merely reflecting the Gaussian time-jitter of the PM, whereas at the other end of the scale, i.e. for large distances, the diffusion equation can be suitably used.

The overall shapes and widths of the functions are varying greatly within this range of cases (see Fig. 56 below), but the resulting fits are satisfying, as can be seen in Fig. 53, which shows time-delay p.d.f.'s for a muon-track passing at various distances from an OM facing it. At a distance of 5 meters, most of the photons remain unscattered. At 20 meters, the left flank has still a sharp rise, but now, most of the events are in the tail of the distribution. At 60 meters and above, this asymmetry is much less marked and the spread has increased considerably. Drawing these distributions on the same plot would be difficult, as the size of their intervals of containment spans over several orders of magnitude. A better way to compare them is by looking at their probability contents, Fig. 54.

Fig. 55 shows the difference in shape between the distributions for modules facing towards, resp. away from the muon-track. As expected, the difference is significant at small distances, where photons emitted by a muon coming from behind the OM have to go through a lot of scatter-

ing in order to hit the sensitive part of the cathode. That difference amounts to a mere (relatively small) shift for large impact parameters. In absolute terms, however, the time-gap between the two cases increases with distance, reaching some 100 ns discrepancy for the mean value after just 10 meters (see Fig 56(c)). For the peak value (or mode), the time-gap reaches 100 ns after 40 meters (Fig 56(b)).

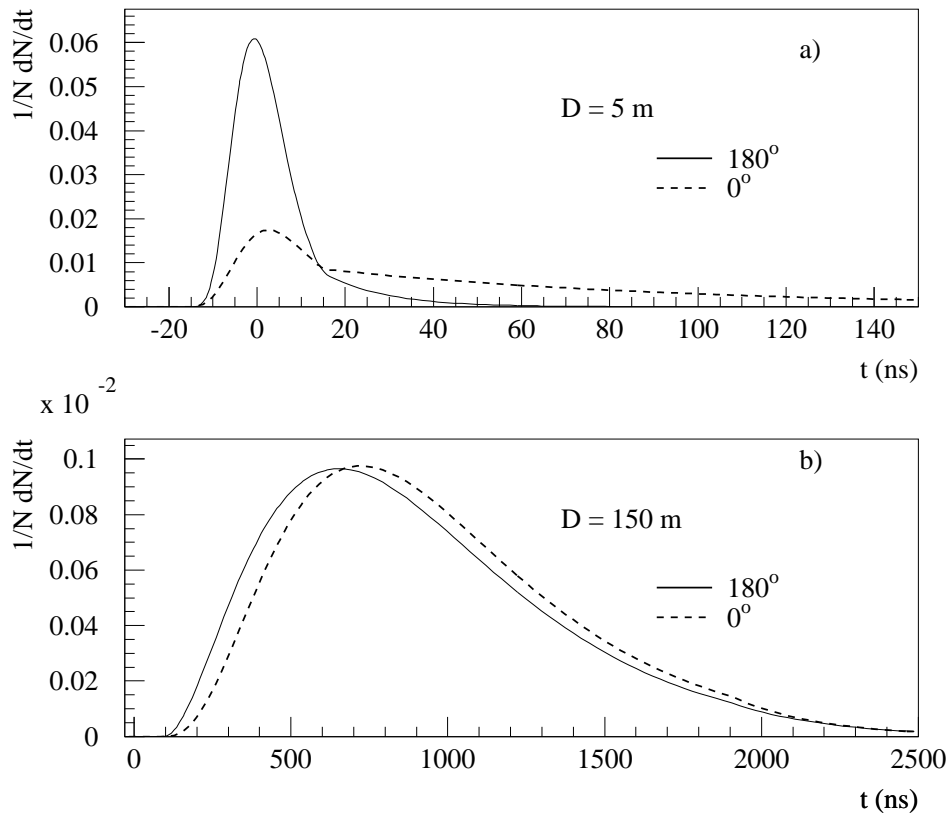


Figure 55: Delay-time distributions for modules facing (full curves) and away-looking (dashed curves) a muon track with an impact distance of 5 meters (a) and 150 meters (b).

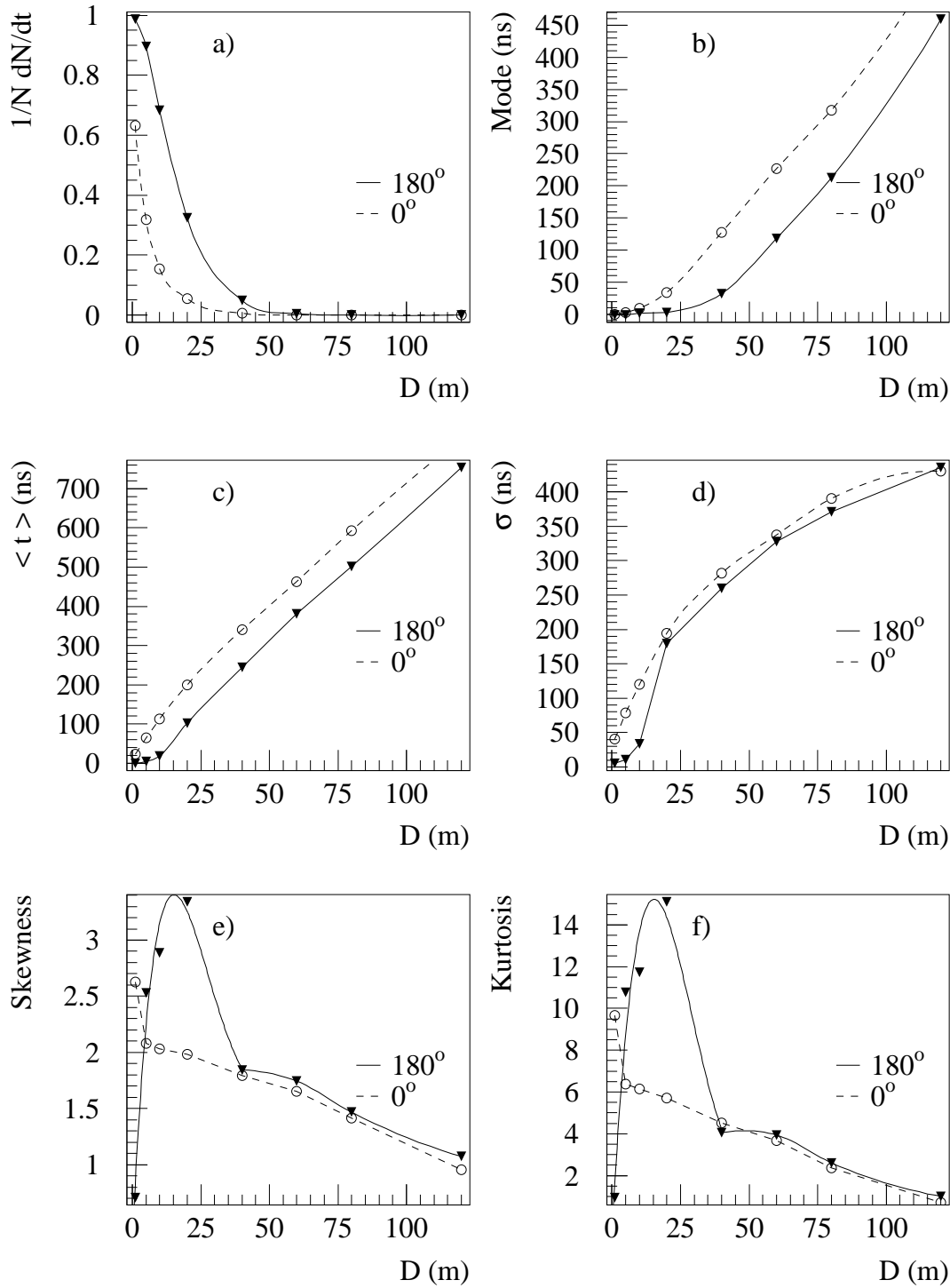


Figure 56: Comparison between time delay distributions of modules facing ($\theta_{OM} = 180^\circ$) and looking away from ($\theta_{OM} = 0^\circ$) muon tracks at different impact distances D . The probability of getting a hit between -15 ns and $+15$ ns is shown in (a). Fig. (b) shows the most probable time, (c) the average delay-time, (d) the standard deviation, (e) the skewness and (f) the kurtosis, all as a function of the impact parameter D .

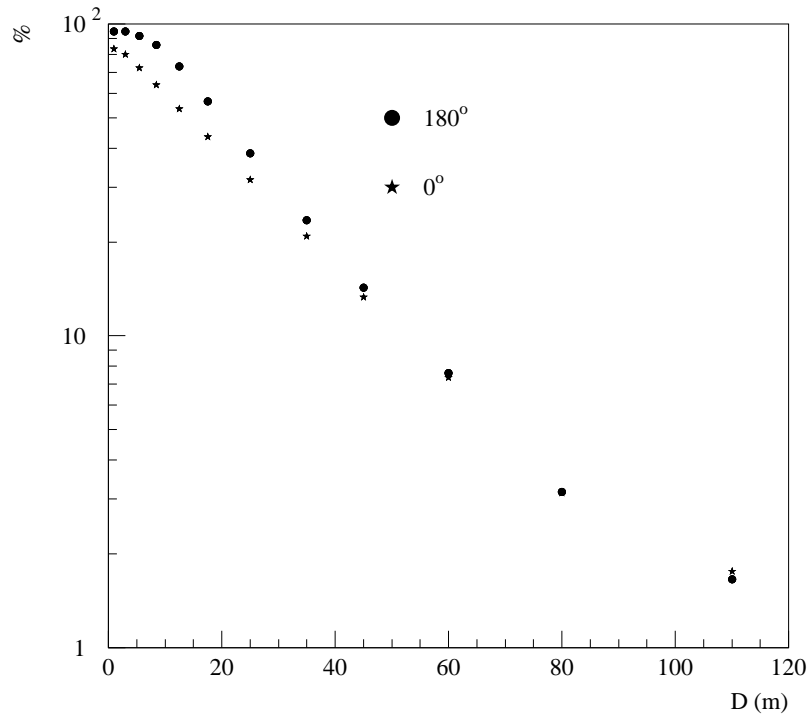


Figure 57: Probability in % of getting a hit from muons coming with an impact parameter D for head-on muons (dots) and muons from behind (stars)

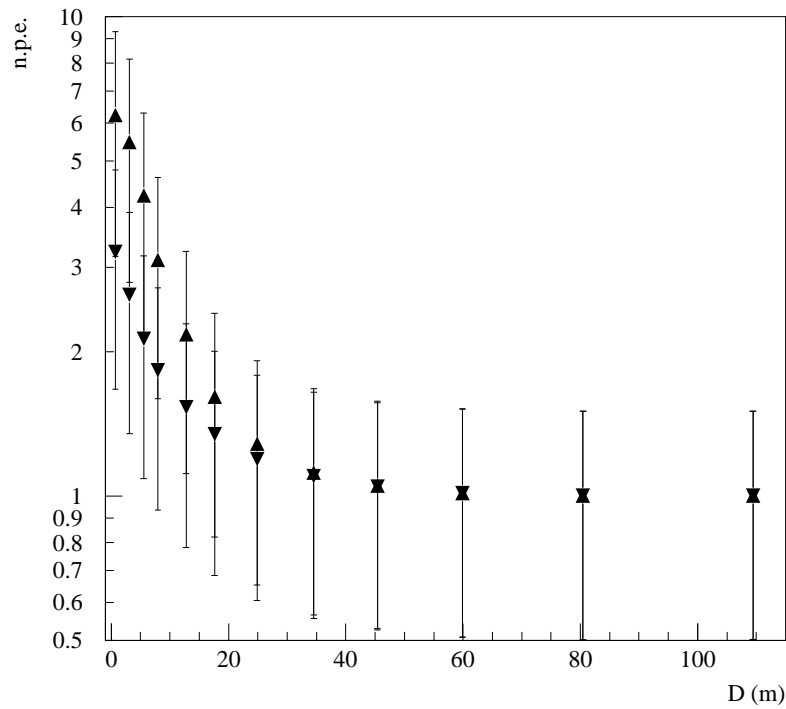


Figure 58: Expected number of photo-electrons given a hit versus distance between OM and track, given that the OM was hit. The up-looking triangles are for OMs facing the muon track and the down-looking triangles represent OMs in the opposite direction. A saturation at 8 p.e.s was used in the simulation.

Several measures of the distributions for the same two orientations of the OM relative to the muon are displayed against distance in Fig. 56.

In (a) we see that the probability for direct hits is clearly larger for a facing than for an away-looking PM and that this fast-falling probability amounts to zero after 50 meters. This is a crucial parameter for reconstruction.

The graphs in (b) and (c) exhibit the same behaviour of both the mode and the mean, namely an increasing gap between the two orientations, stabilizing after some distance. The gap is slowly closed at larger distances, although this can not be seen within the scale of the graphs.

As for the standard deviation, it gets independent of the orientation of the OM after 20 meters, as can be seen in (d).

The skewness (or degree of asymmetry) is positive for all distances, but is markedly dependent on the orientation in a range of 0 to 40 meters (Fig. 56(e)). For an OM facing the muon track, it becomes very large already for distances \sim a few meters, for which there are still a large amount of direct hits and the distribution can be fitted with a Gaussian super-imposed on an exponential. At larger impact distances, the asymmetry of the resulting function is reduced and the skewness tends to zero asymptotically. It is always positive though, meaning that the rise time of the function is always smaller than the fall-time. For an OM looking away from the muon, the skewness is a monotonously decreasing function of distance. After 40 meters, the OM orientation becomes irrelevant.

Roughly the same behaviour can be noted for the kurtosis (or peakedness) in (f). All the curves are leptokurtic, i.e. have a positive kurtosis coefficient, meaning that the height of the peak is large relative to the spread of the function.

For a given choice of parameters $(D, \varphi_{OM}, \theta_{OM})$, the p.d.f. value is yielded by multilinear interpolation. Multilinear interpolation ensures the continuity of a function across grid boundaries, but not necessarily the continuity of the gradient. A higher-order interpolation technique would fix up the continuity of derivatives, but this would require a large number of extra numerical computations [70, 71].

8.3 Reconstruction method

The function $-\log \mathcal{L}$ to be minimized (in Eq. 62) is plagued with local minima, arising because of the periodicity of the trigonometric functions that appear in Eq. 65. Other complicating factors are the size of the problem (five parameters to be determined) and the low number of degrees of freedom for a typical muon event acquired with a trigger of 8/1, as was the case for AMANDA-B4 1996 data, which yields a less pronounced global minimum. Conventional minimization techniques are thus of limited value in this context. A simplex method would not amount to much more than a mere grid search in a five-parameters phase space, an near impossible task with the computer power available in the collaboration. A gradient method would terminate much faster, but such algorithms are also unable to carry on with the search after a local minimum has been reached. However, the smoothness of the considered functions should not lead to serious trouble in this respect.

The algorithm

The minimization technique opted for in order to find estimates of the track parameters is the simulating annealing method (SA), a stochastic global minimization method based on a downhill

simplex algorithm [70]. It is one of the most efficient methods for this kind of minimization and has been evaluated against other methods in [72]. SA combines the extensive coverage of simplex methods with a stochastic decision-making algorithm (Metropolis) which allows it to get out of local minima.

Its name is given by an analogy with the process of slow cooling ('annealing') of a liquid towards its state of lowest energy [70].

Offered a move in a certain direction, the Metropolis algorithm decides to accept that move with a probability $p = \exp[-(f_2 - f_1)/T]$, where f_1 is the value of the function at the moment and f_2 its value for the proposed move. This probability is the Boltzmann probability distribution function. There is always a non-zero probability to accept a move upwards and thus to get out of a local minimum. For a downhill move (i.e. if $f_2 < f_1$), the probability is set to one, i.e. the move is always accepted.

The basic idea of SA is to start with a high temperature T and to lower it in steps according to a predefined scheme, performing a simplex downhill search with a Metropolis decision-making scheme between cooling steps.

In this implementation we chose to change the temperature T , lowering it by 5% each time, using 200 steps. These figures were reached by varying the parameters and comparing the results after intensive computations. The starting values of the simplex were found in the same empirical way. As starting values, the solution given by the plane-wave fit (see Eq. 76 below) was assigned to the first node of the simplex and the remaining nodes were set to the same value, but with added deviations of:

- 10 meters in x_0 for node 2
- 10 meters in y_0 for node 3
- 0.1 radian ($\sim 5.7^\circ$) in φ for node 4
- 0.1 radian ($\sim 5.7^\circ$) in θ for node 5
- 1000 nanoseconds in t_s for node 6

Starting points

A very useful first guess for the parameters to be fitted can be calculated by making a line fit of the hit-times to the OM coordinates [73, 74]. This is done by describing the muon position at any time t with the equation:

$$\vec{r} = \vec{r}_o + \vec{v}t \quad (74)$$

and minimizing the least-square function (where the weights q_i are a measure of the amplitude of the signal in PM# i):

$$X^2 = \sum_{j=1}^3 \sum_{i=1}^{N_{hits}} q_i (x_i^j - x_0^j - v^j t_i)^2 \quad (75)$$

with respect to the six parameters \vec{r}_o and \vec{v} . The procedure is equivalent to fitting the track to the modules and yields the set of solutions:

$$x_0^j = \frac{\sum_{i \neq k}^{N_{hits}} \sum_{k=1}^{N_{hits}} q_i q_k [x_i^j (t_k^2 - t_i t_k) + x_k^j (t_i^2 - t_i t_k)]}{\sum_{i \neq k}^{N_{hits}} \sum_{k=1}^{N_{hits}} q_i q_k (t_i - t_k)^2} \quad (76)$$

$$v^j = \frac{\sum_{i \neq k}^{N_{hits}} \sum_{k=1}^{N_{hits}} q_i q_k (x_i^j - x_k^j)(t_i - t_k)}{\sum_{i \neq k}^{N_{hits}} \sum_{k=1}^{N_{hits}} q_i q_k (t_i - t_k)^2} \quad (77)$$

Eq. 75 expresses that the sum of the squared distances between the track and the OMs hit should be minimized, which is equivalent to saying that the light from the muon should hit an OM at the time of impact (or closest approach to it). This means that the solution yielded is that for a plane-wave passing through the detector, i.e. that we have approximated the conical Cherenkov wavefront with a plane.

The resulting track passes through the barycenter of the projections of the hit OMs in a plane orthogonal to the fitted vector \vec{v} . Note that the solutions are given explicitly and hence can be computed very fast.

This first guess is not always successful and the minimization has to be restarted several times, with alternative starting points. These other tracks are chosen as tracks with 40° , 80° and 120° declination angle and 0° , 90° , 180° , 270° azimuthal angle relative to the plane-wave solution. In practice however, the gain in performance is low since the SA method goes through most of the phase-space during its global minimum search, and one or a couple of starting points including the line-fit are enough. The mean θ -error for an isotropic muon distribution is 26° and the mean total error is 39° before any cuts.

Correlations

So far, the coordinate system used was assumed to be arbitrary. In fact, the reconstruction depends on its choice both for precision and for computational speed.

If the reference plane used is located far away from the concentration of hit OMs, the angular track-parameters will be highly correlated with x_0 , y_0 , making the minimization harder. This can easily be seen in Fig. 59: for a muon-track passing through the detector in that frame, small steps in θ near the solution will be matched up by large steps in the x_0 and y_0 direction. For that reason, we decided to use a specific coordinate system for each event, having its origin at the center-of-mass of the hit OMs weighted by their number of photo-electrons and a z-axis along the plane-wave guess. Having the origin in the middle of the data-points (the OMs) is a usual way of avoiding correlations between the parameters to be fitted.

Using the direction of the first guess as z-axis has the advantage of reducing the risk of choosing a coordinate system for which the solution might be parallel to the x-y plane.

Performance

STREC was tested on several samples of naked single muon events simulated by LOLITA, coming from a fixed declination and random azimuthal angles. The absolute error, $|\theta_{reconstructed} - \theta_{MC}|$ is histogrammed for samples simulated at 20° intervals. All events were simulated with a background noise rate of 300 Hz in each PM [20], a bit lower than those rates measured in-situ at the South Pole, and cleaned in the canonical way described in section 7.1.

A first observation, before making any cuts, is that steeper tracks seem to be better reconstructed than those coming from a direction closer to the horizon (see Fig. 60). The dimensions and shape of AMANDA-B-4, a ~ 30 meters in diameter and ~ 380 meters long array, may well explain differences in resolution, since an up-going track has a better chance to pass close to

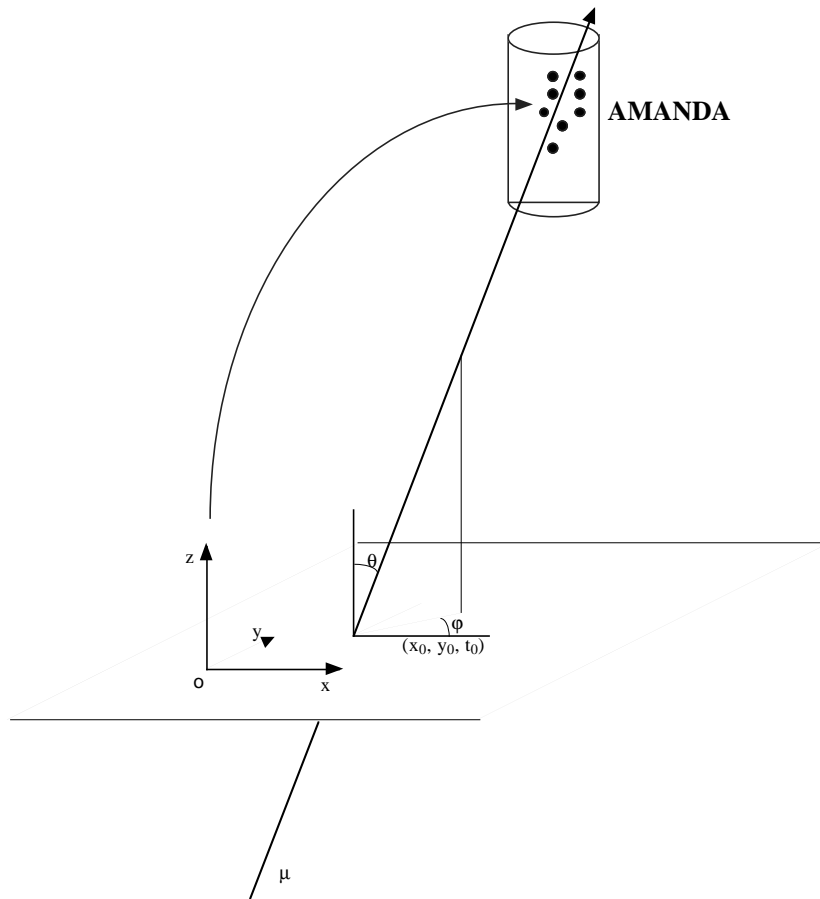


Figure 59: If the origin of the reference frame is located too far away from the data-points, large correlations between the fitted parameters make the minimization difficult. This effect may be reduced by using a system with its origin inside the detector.

several tubes and therefore yield unscattered hits, than a near-horizontal track. One should keep in mind that neighboring OMs on a string are separated by 20 meters, which is a large distance when it comes to getting unscattered light, as shown in Fig. 56(a).

Tracks coming from above the detector are also better reconstructed than those coming from the side, although less well than straight up-going ones. The latter is due to the smaller quantum efficiency of the down-looking PMs for photonic hits from behind, biasing hits from down-going light to scattered paths and thus larger delays.

In fact, after applying a cut demanding that at least five or six OMs should have a time residual between -15 and $+15$ ns, the efficiency (defined as the percentage of events surviving that cut) drops drastically for near-horizontal tracks (see Fig. 61).

The effective area of AMANDA-B4 has a similar declination dependence and would reinforce the above-defined efficiency, suppressing horizontal events and motivating the search for straight up-going events undertaken later on. For the same reasons, there are no good prospects to find high energy muons from horizontal air showers.

The θ -error after reconstruction looks different for different angles, as illustrated by Fig. 62.

Table 15 yields the results, with no entries for the angles at which cutting on the data reduces the number of events so much that no reliable fit can be made (Fig. 62). The last two columns show that the reconstruction method has a declination-dependent systematic shift of the order of a degree and a mean error of about three degrees. The root mean squared (r.m.s.) is a measure that can be used for the simulation angles where the distribution $(\theta_{reconstructed} - \theta_{MC})$ has a Gaussian shape, but would not make much sense, for straight up-going tracks (see Fig. 62). However, by simply looking at the distribution $|\theta_{reconstructed} - \theta_{MC}|$, one can see that the error is still of the order of three degrees for that error estimate for these tracks.

The resolution in the ϕ -direction is not as good, probably due to the low string-multiplicity and to the distance between strings (between 30 and 80 meters) which is much larger than the distance between neighboring modules (20 meters). For steep tracks, the mean error in ϕ grows larger: in fact for straight up- or down-going tracks, ϕ is by definition undetermined.

The total angular mismatch is independent of which specific coordinate system is chosen and is $\sim 1.5^\circ$ for straight up- or down-going tracks and goes up to $\sim 6.5^\circ$ for less steep tracks (see table 16).

No pulse height information was used in the reconstruction, except in computing the first-guess. However, that information exists in real data and is interesting from the point of view of robustness -timing is relative whereas photo-electrons are absolute numbers. An easy way to use it would be to weigh the components of Eq. 62 by the corresponding likelihoods for amplitudes, or to add a corresponding pulse height likelihood function to the first one. But given that the ADCs were not properly normalized and that electronics were simulated only very roughly in LOLITA at the time when this study started, we decided to do without. This is not to say that the pulse-height information was left unused altogether: in fact, it was used in the hit-cleaning and the pre-filtering of both data and Monte Carlo simulation and the plane-wave fit makes also use of it.

Fig. 57 displays the probabilities to get one photoelectron or more as a function of impact parameter for simulated muon-tracks. A few interesting remarks can be made: the effect on this probability of the orientation of an OM relative to a muon is marked but at most 27% and it disappears virtually after 40 meters; the probability drops below 50% after 10-17 meters and below 95% further away than 60 meters. These figures can be used to assess the validity of a reconstruction. One could for instance reject a track if reconstructed as passing close to several functioning modules that got no hits at all.

Attempts were also made to improve reconstruction results by discarding tubes with large residuals and performing a new fit in an iterative way. However, this approach did not yield any noticeable progress and was abandoned as the cost in computation time increases linearly with the number of starting points. On the one hand, long delays may degrade the quality of the reconstruction but on the other hand, with a Maximum-Likelihood approach, they tend to have a stabilizing effect by the sheer fact of increasing the statistics.

θ_{MC}°	$ (\theta_{reconstructed} - \theta_{MC}) $ (no cut)		$ (\theta_{reconstructed} - \theta_{MC}) $ $N_{direct}[-15; 15] \geq 5$		$(\theta_{reconstructed} - \theta_{MC})$ $N_{direct}[-15; 15] \geq 5$	
	Mean	R.M.S	Mean	R.M.S	Mean	σ
0	7.2	19.3	1.5	1.2	-	-
20	8.6	18.3	3.2	3	-1.9 ± 0.2	2.7 ± 0.2
40	19.3	27.7	3.3	3	-1.6 ± 0.4	3.4 ± 0.5
60	19	22.7	-	-	-	-
80	20.8	20.9	-	-	-	-
100	22.6	23.4	-	-	-	-
120	21.9	26.6	-	-	-	-
140	18.4	28.2	-	-	-	-
160	14.8	30	3.2	3.3	1.2 ± 0.3	2.9 ± 0.5
180	11.2	26.7	1.7	1.3	-	-

Table 15: Some measures of the error in θ for events simulated at a fixed angle θ_{MC} . No values are given when the statistics are too low, or when making a gaussian fit is not relevant due to the high asymmetry of the distribution. All values are in degrees.

θ_{MC}°	$ (\phi_{reconstructed} - \phi_{MC}) $ $N_{direct}[-15; 15] \geq 5$		$\widehat{Track_{rec.} - Track_{sim.}}$ $N_{direct}[-15; 15] \geq 5$	
	Mean	R.M.S	Mean	R.M.S
0	-	-	1.5	1.2
20	18.2	24.6	6.6	6
40	8.4	7.7	6.9	4.7
60	6.6	6.9	6.8	6.2
160	18.2	30	6.5	6.9
180	-	-	1.7	1.3

Table 16: Estimates (in degrees) of the error in ϕ and of the total angular mismatch for single muons simulated at different θ angles.

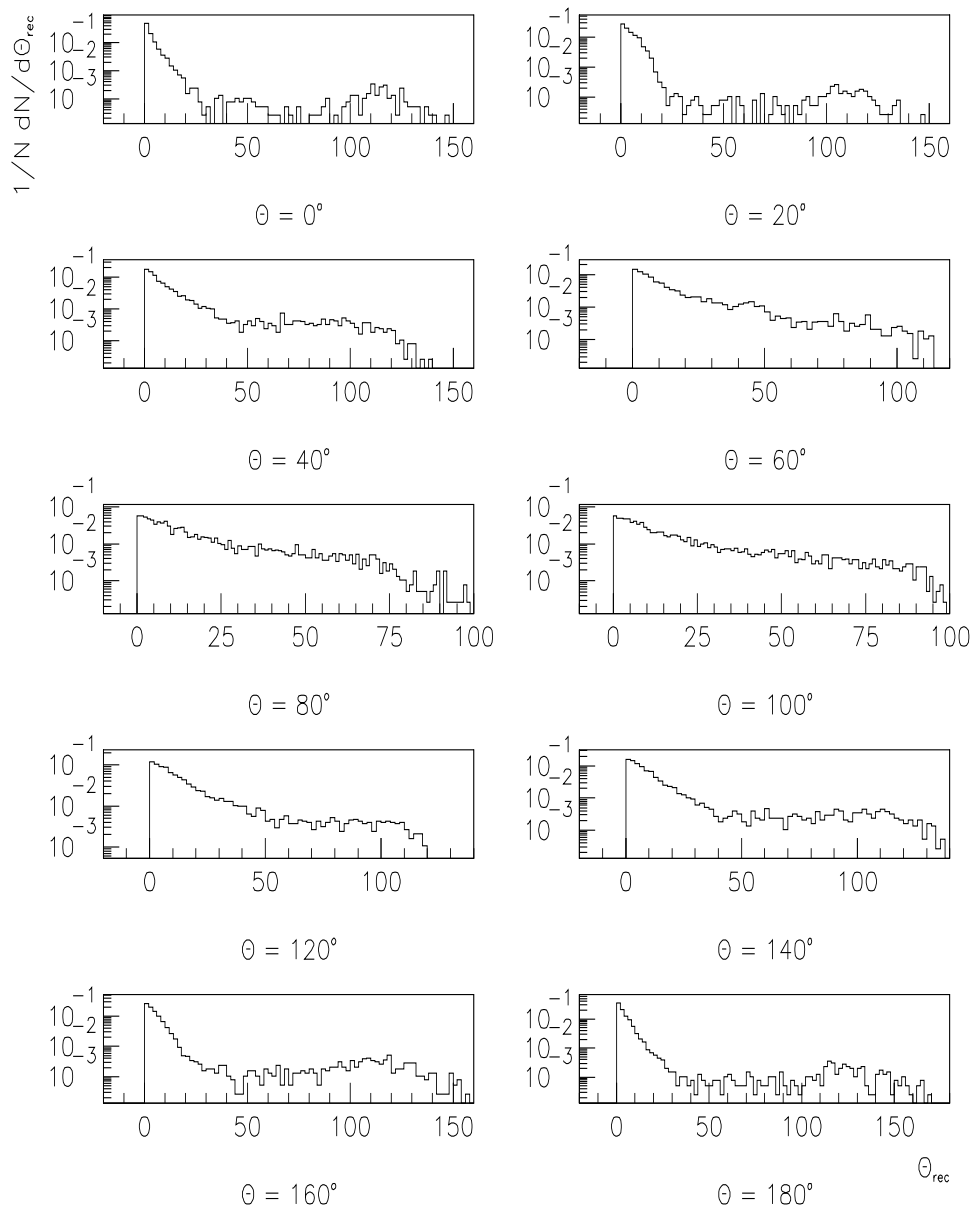


Figure 60: $|\theta_{reconstructed} - \theta_{MC}|$ for samples simulated at different angles.

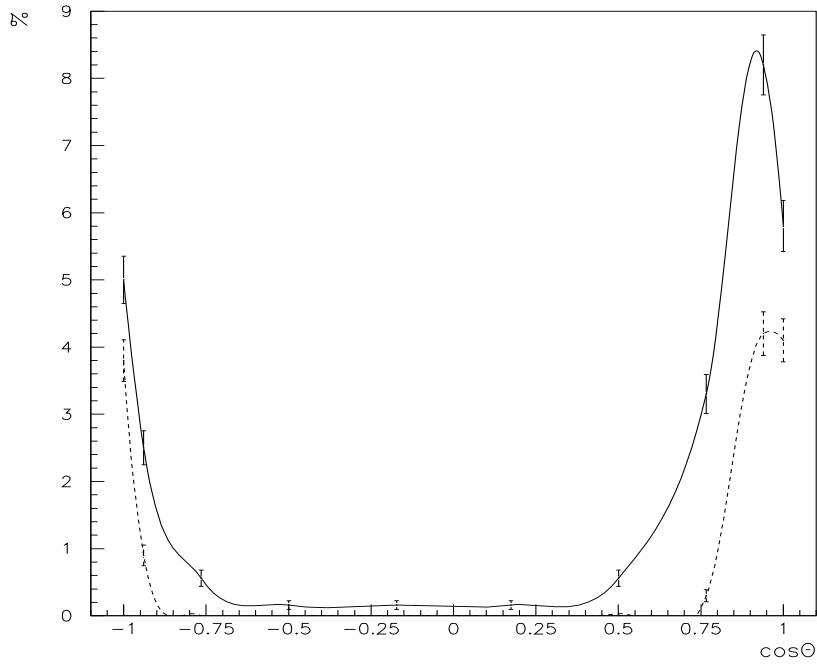


Figure 61: Percentage of reconstructed events surviving a cut of at least five (full line) or six (dotted line) direct hits between (-15 and +15 ns) as a function of their θ -angle.

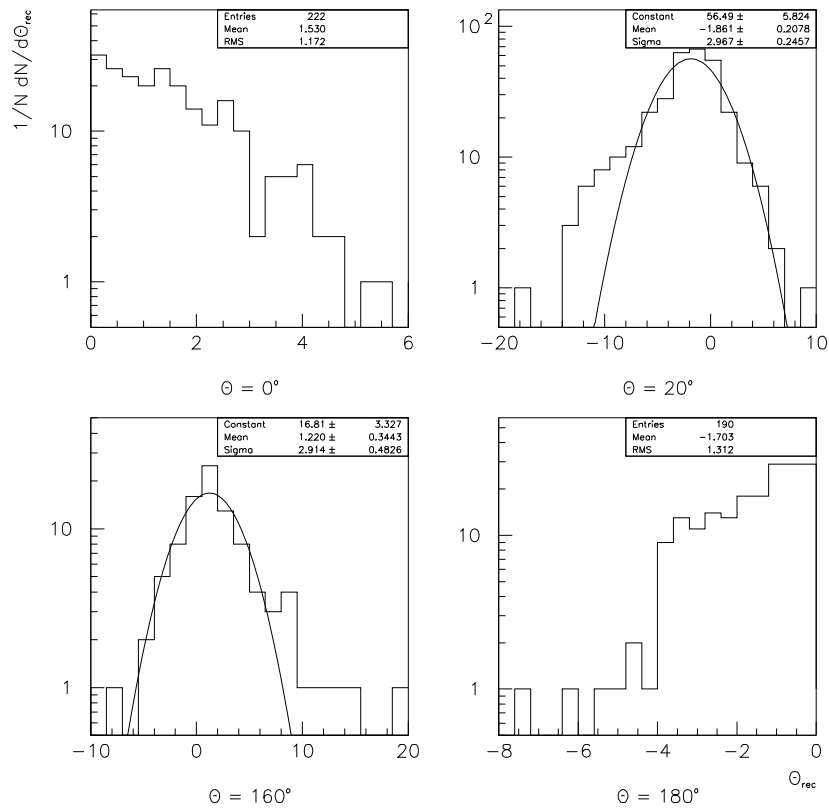


Figure 62: $(\theta_{reconstructed} - \theta_{MC})$ for muon samples simulated at different angles demanding that at least five residuals must be in the interval [15;+15]ns.

9 Analysis of 1996 data

There are two main sources of background to the expected signal of cosmic VHE neutrinos. One is the flux of secondary atmospheric muons resulting from air showers, coming with a zenith angle of more than 90 degrees, the other is the isotropic flux of atmospheric neutrinos produced in air showers too.

Quantitatively, these two fluxes are very different, but whereas muons are stopped by ~ 10 km [7] of Earth material and can thus effectively not be observed by AMANDA below an angle of $\sim 10^\circ$ above the horizon, the neutrinos are not stopped and become the major diffuse background to up-going signals.

The first kind of event is a background to the expected signal in the sense that it can be misreconstructed as an up-going muon, because of the large ice-induced time-smearing combined with the typically low OM multiplicity in a sparse detector. The second kind is a less problematic background, although it yields data which on an event-by-event basis is completely indistinguishable from those left by cosmic neutrinos. The reason for this is that the atmospheric neutrino background is expected to be nearly isotropic, whereas with a good enough angular resolution, signal point-source events coming from a small solid angle can clearly be seen above that background. The expected number of atmospheric neutrino induced events is estimated in [79].

9.1 Description of the data sample

The data was taken between mid-February and the end of October 1996, with an 8-fold majority trigger. This period is equivalent to 6 months of live-time or, with a mean trigger rate of ~ 26 Hz, to $4 \cdot 10^8$ events. During most of this time, the trigger rate stayed at an almost stable level (i.e. did not fluctuate by more than 0.5 Hz around some mean value during periods of \geq month). A sharp drop can however be seen, occurring around day 130, from ≈ 27.5 to ≈ 25.5 Hz. This is strongly correlated with a change in the average ADC values recorded by a subset of PMs, probably due in turn to new high voltage settings. Further small variations are due to the turning on and off of experiments such as SPASE sending coincidence trigger signals to AMANDA-B and other sources of disturbances, to be determined (possible such sources are external noise, changes in the muon rate caused by varying atmospheric conditions [75], etc.). Larger variations could often be traced back to a failure or an incorrect readout of the GPS repeater, which occurred during a fraction of the data-taking session used to calculate the rate. However, this did not affect the quality of the data in any other respect.

The coincidences with AMANDA-A, SPASE-1 and SPASE-2 represent $\sim 1\%$, 14% and 2% of the collected data, respectively, when these detectors were on. The bulk of the events are due to atmospheric muons, whereas a small fraction comes from other sources, such as muons created when atmospheric or cosmic neutrinos interact with matter inside and in the vicinity of the detector.

Out of 86 deployed OMs, nine did not survive the refreezing period, whereas the remaining are still functioning. The six modules at the bottom of string four were using a twisted pair cable and were not calibrated properly during the 95/96 season. They were the deepest buried OMs and it was difficult to send down enough light through an optical fiber of 2000 m. Therefore, these modules were not used in the analysis, which concentrated on the 71 remaining ones.

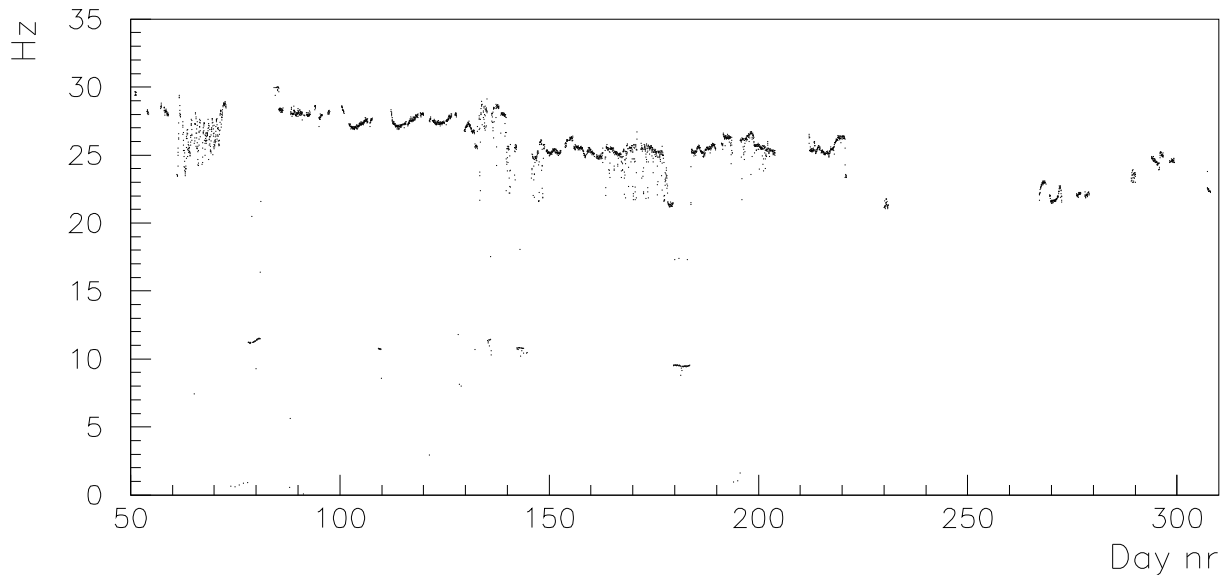


Figure 63: Data-taking rate of AMANDA-B4 as a function of time. All triggers, including those coming from detectors operated in coincidence external are counted. Each dot represents one run.

9.2 Atmospheric muons

The angular distribution of atmospheric muons at the surface of the ice produced with HEMAS is shown in Fig. 64. These muons were yielded by primary cosmic rays with energies between 10^3 and 10^4 TeV and demanding that the muon energy should be at least 500 GeV at their production point above the surface of the ice. The muon multiplicity in each bundle can be quite high, (see Fig. 65). The flux of muons that have triggered the detector hardly shows any difference in its declination distribution.

However, the pre-filtering clearly shifts the data sample to more horizontal tracks as can be seen from Fig. 66. This is in order, since its task is to remove all the more or less obviously down-going events. As a result, we are left with more ambiguous events, such as near-horizontal tracks and, in the case of real data, cascades and brehmsstrahlung, which were not yet simulated in LOLITA at the time of this analysis. For geometry reasons, such events are less likely to yield direct hits than straight down-going tracks.

9.2.1 The atmospheric muon spectrum

Reconstructing data and Monte Carlo simulated events with STREC yields similar θ distributions. Fig. 67 shows the reconstructed declinations for the real data and for atmospheric muon-bundles simulated with LOLITA and, to make the comparison fair, these histograms have not been normalized to each other. The differences seen can be due to the unsophisticated hardware simulation in the Monte Carlo simulation and to the missing implementation of secondary processes. Other possible reasons could be that the optical properties of the ice might be changing with depth, whereas LOLITA assumes them to be depth-independent. Also, the angular efficiency of the OMs, or, to rephrase it, the properties of the ice in the hole close to modules locations might be affected by a higher amount of scatterers (such as bubbles, e.g.) induced during the melting and refreezing of the ice. This would allow photons passing very close to a mod-

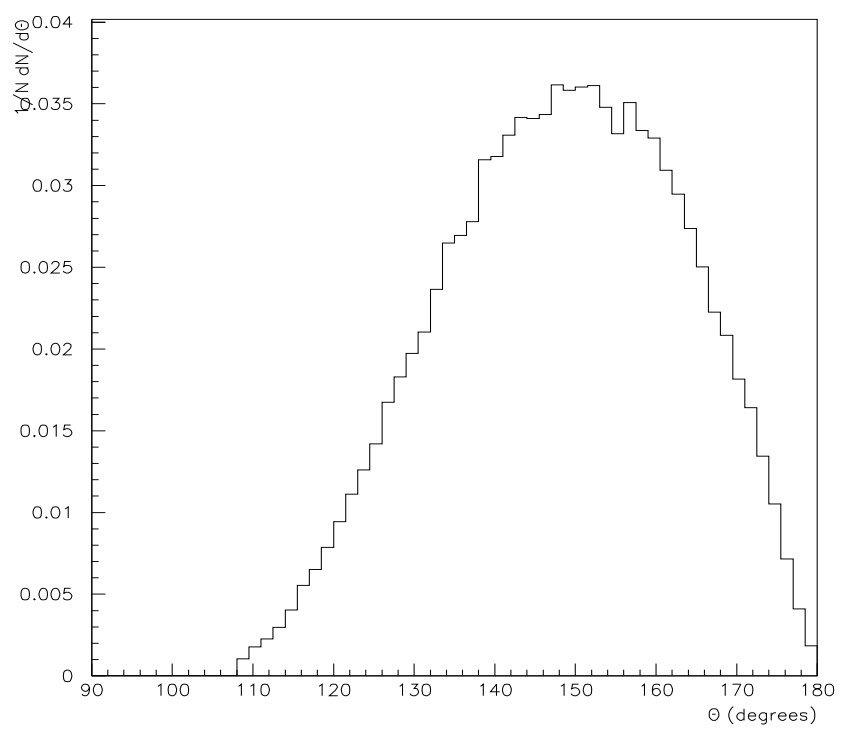


Figure 64: Atmospheric muon flux at the surface of the ice as produced by HEMAS.

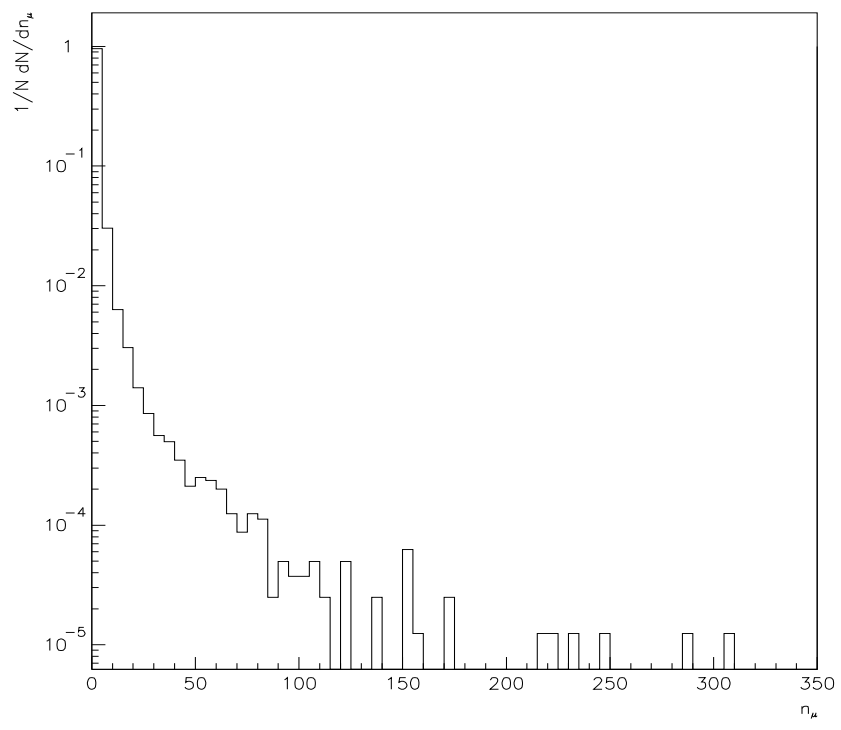


Figure 65: Muon bundle multiplicity at the surface of the ice.

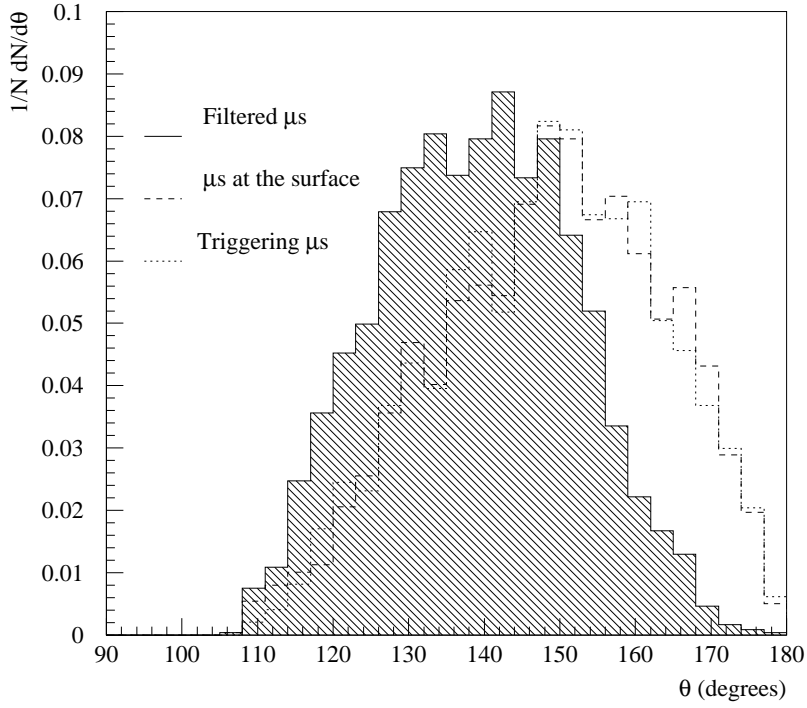


Figure 66: Monte Carlo declination distribution of muons that have triggered AMANDA-B 4-strings

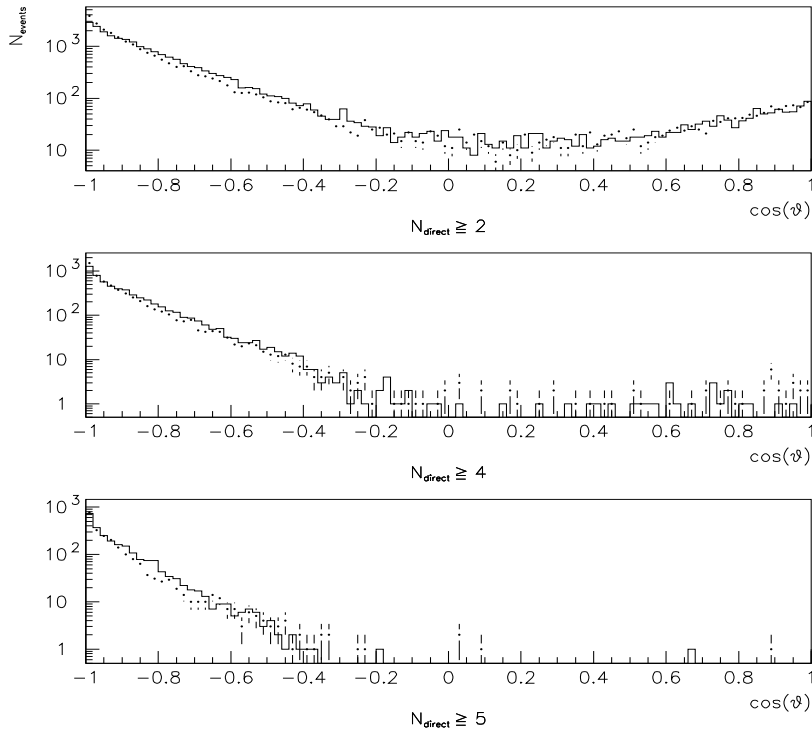


Figure 67: $\cos(\theta_{rec})$ is shown with cuts on the number of residuals in the interval $[-15; 25]$ ns. The solid line represents Monte Carlo simulations with a trigger of 8-2 and the dots with error bars represent the real data

ule to scatter back and give a hit, whereas they would just pass by it in the simulated model and the net effect would be that light coming from above would take a shorter path and thus be less delayed. Notice however that, as harder cuts are applied on the number of unscattered hits, the overall shapes of the distributions still agree well 67.

Another way of comparing data and Monte Carlo simulations is to look at the percentage of events that survive a certain cut. Fig. 68 shows that number as a function of a cut N_{direct} which is defined as the minimum number of residuals within two limits [69], here -15 and +15 ns. There are less events left from real data at any N_{direct} level and, as expected, this difference gets larger with harder cuts. When requiring at least five direct hits, the disagreement is of the order of 30%.

The tidying up of the simulated data by such a cut is clearly seen in Fig. 69, where the reconstructed θ angle is plotted against the simulated θ . Putting harder cuts on the events makes the difference between the simulated and the true θ smaller and the points converge to a line with slope 1.

The resulting resolution in θ for events having gone through a cut of five or more small residuals is $\sim 2.2^\circ \pm 0.1^\circ$ and $\sim 13.8^\circ \pm 0.7^\circ$ for ϕ (see Figs. 70,71). This can of course only be computed for simulated events, but we will see later, that thanks to the coincidence data taken with SPASE-2, we have the means of getting a good idea of what the angular resolution is for real data.

The ϕ resolution is correlated with the simulated ϕ and anticorrelated with the number of strings hit in the muon events. This behaviour (which could be expected) is illustrated in Fig. 72, showing the resolution in ϕ versus the angle of the simulated muon-bundle on the one hand and versus the string-multiplicity on the other. A light cut of two unscattered hits or more was applied, in order to have enough statistics left to still see the effect.

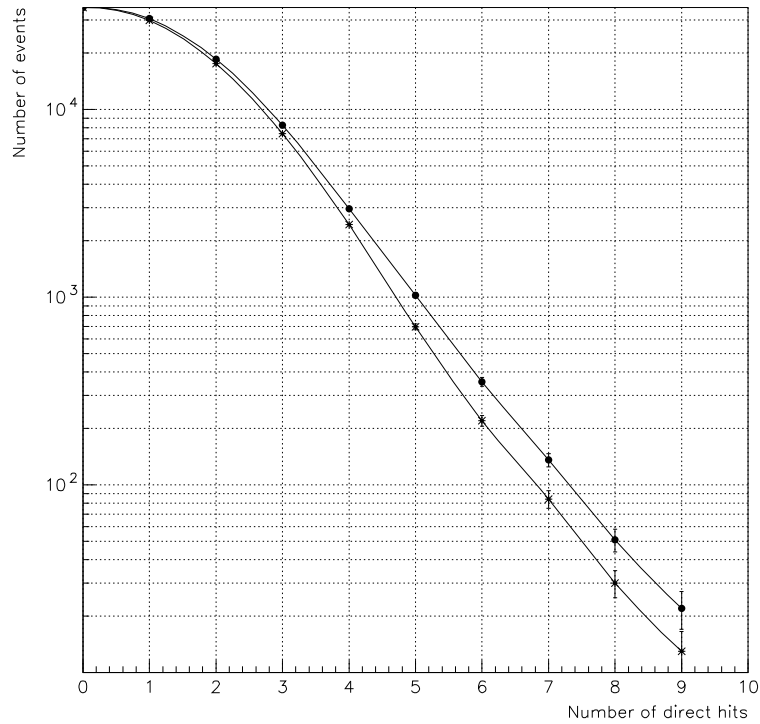


Figure 68: Number of events left as a function of a cut made on the number of residuals left in the interval $[-15; 15]$ ns. The dots represent Monte Carlo simulations with a trigger of 8-2 of atmospheric muons and the stars represent the real data.

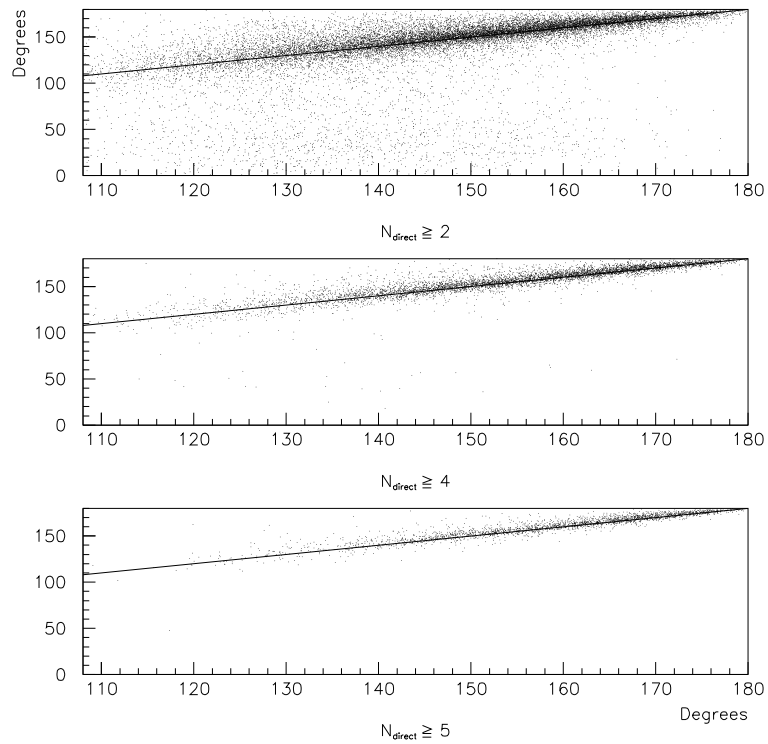


Figure 69: Scatter-plot showing the AMANDA-reconstructed θ -angle of atmospheric muons versus the MC, at several cut levels.

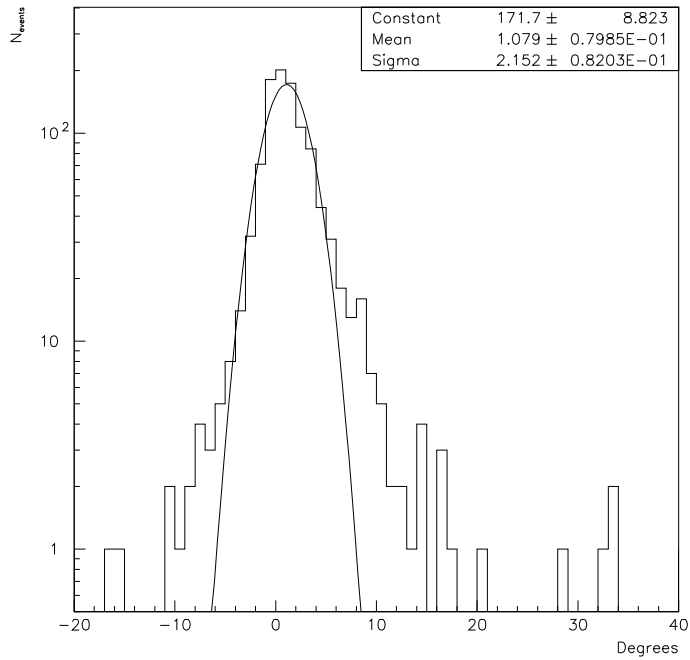


Figure 70: $\theta_{rec} - \theta_{MC}$ for STREC-reconstructed atmospheric Monte Carlo simulated muons with at least five residuals in the interval [-15;15] ns

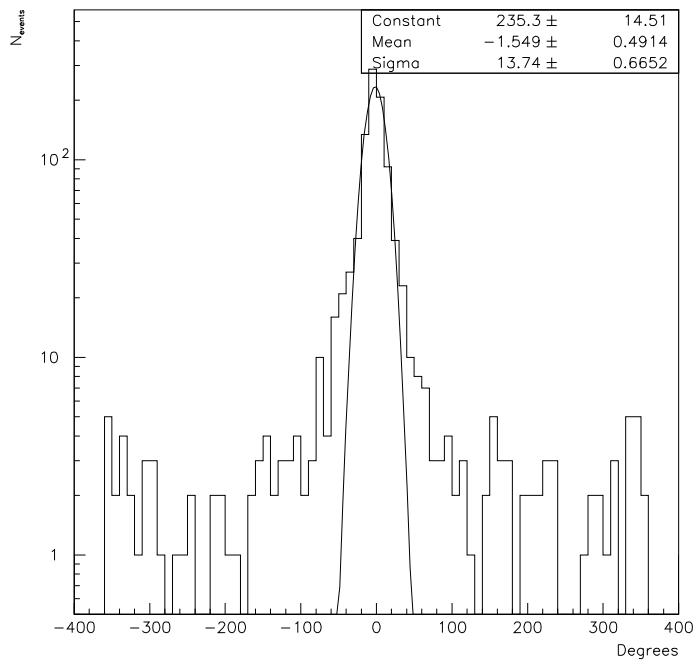


Figure 71: $\phi_{rec} - \phi_{MC}$ for STREC-reconstructed atmospheric Monte Carlo simulated muons with at least five residuals in the interval [-15;15] ns

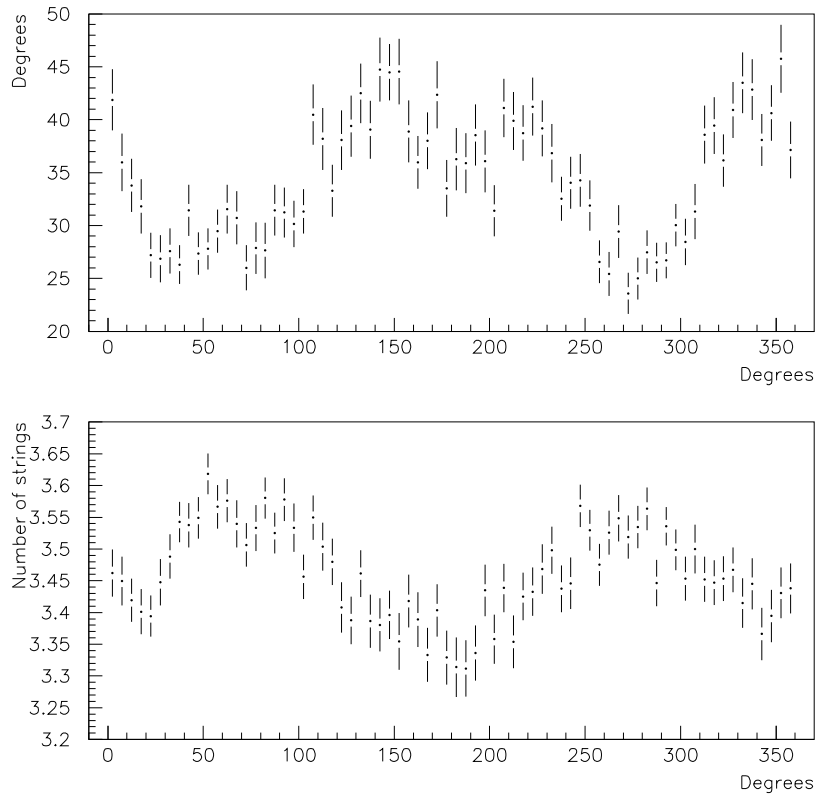


Figure 72: Top: $|\phi_{rec} - \phi_{MC}|$ vs. ϕ for STREC-reconstructed atmospheric Monte Carlo simulated muons with at least two residuals in the interval $[-15;15]$ ns. Bottom: mean number of strings hit for the same events. Note the anticorrelation.

9.2.2 SPASE coincidences

The SPASE (South Pole Air Shower Array) detector is located in the vicinity of AMANDA (see Fig. 73) and has proved to be a useful tool for the debugging of the detector.

SPASE-1, which consists of 16 detectors spread out over a 30 meters grid enclosing an area of 6200 m², was deployed in 1987-88. Each one of the 16 detectors includes a 1.0 square meter scintillator viewed by a 3-inch EMI photomultiplier tube.

Closer to AMANDA, SPASE-2 was added in 1994-95 and completed in 1995-96. It consists of 120 similar scintillator modules equipped with Hamamatsu or EMI PMs, which are spread out over an area of roughly 16000 square meters and grouped in 30 stations disposed on a triangular grid. SPASE aims at detecting primaries with energies $\sim 3 \cdot 10^{15}$ eV, i.e. in the region of the knee [76], [77] and has a dynamical range extending from approximately 100 TeV up to 30 PeV with good efficiency [78]. This detector triggers if at least one module from each of several of the 30 stations registers a particle in a one microsecond window.

The data is collected using equipment similar to AMANDA's, i.e. CAMAC modules controlled by a Jorway73-A crate-controller and read out by a DAQ written with Kmax. In the same way as for AMANDA, a Hytec list-processor (LP1341) is used to speed up the system.

The SPASE-AMANDA coincidences are providing information about the muon content of showers, useful to study primary composition, since heavy primaries generate more muons than light primaries of the same energy per nucleus [76] [7]. SPASE-2 (together with the VULCAN Cherenkov array) is measuring the shower size and height and the Cherenkov intensity far from the core.

This is the closest one can come to a beam in this kind of experiment: a fair amount of muons that have triggered either of the two SPASE detectors can be seen in coincidence by AMANDA, and SPASE can provide accurate information about the direction of the primary particle.

The range of a coincident muon has to exceed the ~ 1500 meters between the detectors, putting a threshold of ~ 400 GeV on its energy at the surface. Each time SPASE sees an air shower, a trigger signal is sent to AMANDA and all PM signals are read out over a period of several microseconds. The trigger rate is thus increased by 14%. Further conditions can thereafter be imposed off-line to select interesting events. SPASE is also reporting coincidences in a similar way to AMANDA-A.

The declination angle of SPASE-1 in the AMANDA coordinate system is $\sim 26^\circ$ and for SPASE-2 it is around 12° (see Fig. 74). Due to the distance between the detectors, tracks actually passing through both of the detectors cannot deviate from these directions by more than $\sim 5^\circ$ degrees.

Unfortunately, during the year 1996, most of the time the ADC values were not recorded for SPASE-1—AMANDA-B coincidences, making proper time correction (see section 6.1) and thus track reconstruction impossible. This problem did not occur for SPASE-2 coincidences, which is however located at the steeper mean angle of 12° . The acceptance for these events is 32 m²sr and the coincidence rate is 14 hr⁻¹ ($3.9 \cdot 10^{-3}$ Hz) [76] for events triggering AMANDA-B4 as well.

The coincidences were extracted from the two data-sets using the SPAMLINKER program to find events with matching GPS times and were then reconstructed with both STREC and the SPASE analysis tool.

A comparison between reconstruction results for data collected during 80 days is shown in Fig. 75. The long tail in the θ -distribution reconstructed by SPASE-2 shows that the selection criteria were very loose. Applying a simple cut on the number of residuals N_{direct} lying between

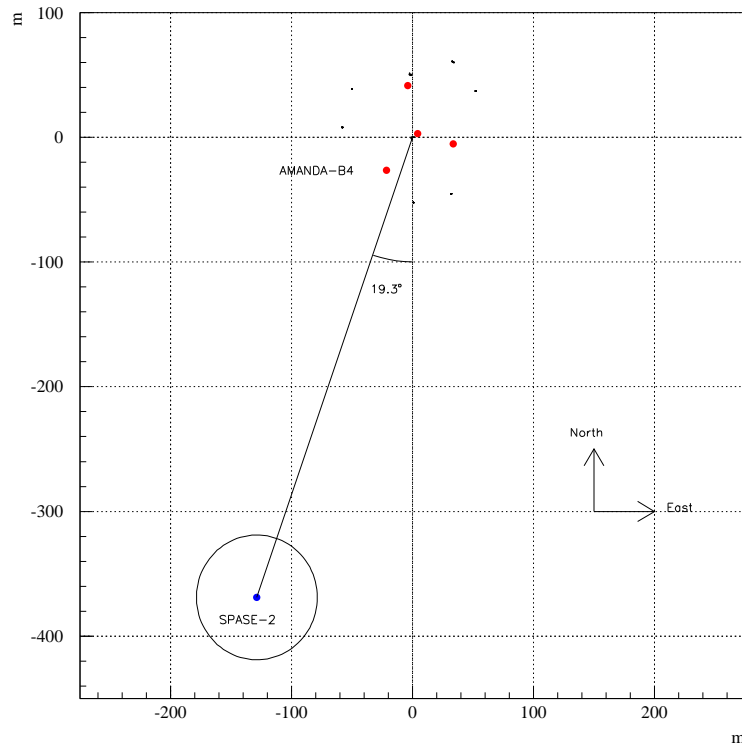


Figure 73: SPASE-2 and AMANDA-B4 seen from above in the AMANDA reference frame where the x-axis is in the North direction, taken as the Greenwich meridian.

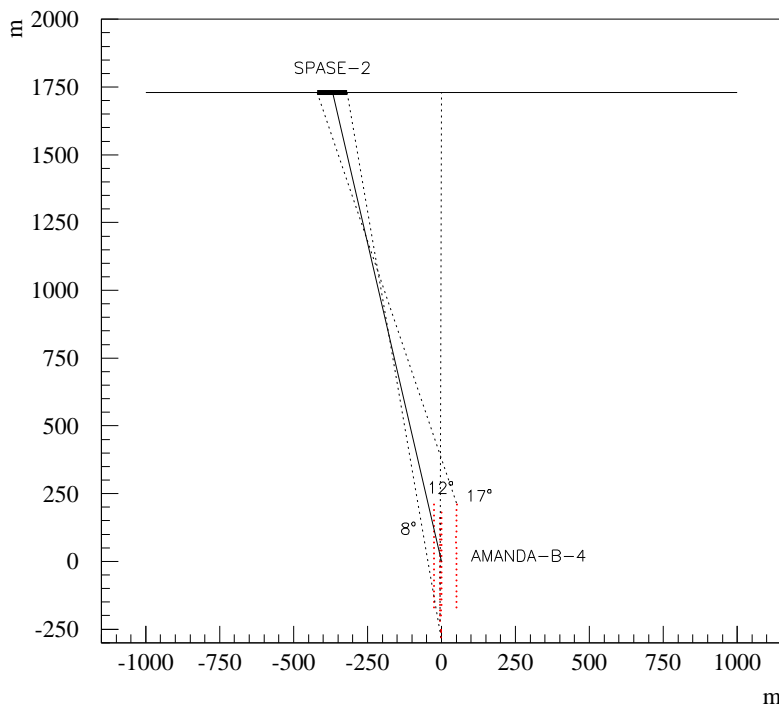


Figure 74: Side view of SPASE-2 and AMANDA-B4 in the AMANDA reference frame. North is in the direction of positive abscissa.

-15 and 15 ns after the STREC reconstruction removes many misreconstructed events in both the AMANDA and the SPASE θ distributions. The mean and width of the two distributions become comparable, with a small difference between the average values that can be assigned to the fact that no further cuts were applied on the SPASE reconstructions. Considering that several of these events are multi-muons coming from the least favorable direction for unscattered photon hits, the agreement in results is very good.

Furthermore, a simple cut of five or more direct hits was enough to get rid of all misreconstructions from below, hinting that steep atmospheric muons (SPASE is at 12° declination) might not be the worst background contribution after reconstruction. Instead, single cascades and muons coming in from the horizon might be contributing more to fakes.

Fig. 76 shows the polar angle difference ($\theta_{rec} - \theta_{MC}$) between real data and simulated atmospheric muons selected in a solid angle around the direction of SPASE, both reconstructed with STREC. Also shown is ($\theta_{rec} - \theta_{SPASE}$), for a comparison with the SPASE reconstruction. All events are subjected to a cut of $N_{direct} \geq 5$. These histograms show that differences between reconstructed coincidences from data and Monte Carlo simulated muons are compatible with differences between independent STREC and SPASE event reconstructions. Given that the angular distribution of the simulated muons is very rough, the agreement in shapes and average values of the histograms is satisfying.

The survival rate to the cut on direct hits is in good agreement with results yielded by LOLITA, as can be read out from Fig. 61, yielding a Monte Carlo simulation efficiency of 3.4% for a muon angle of 168° , 2.6% for the shallowest tracks and 3.7% for the steepest tracks passing through both detectors. The proportion of real data (3.6%) that survive the cut used in Fig. 75 is thus compatible with the expectation from Monte Carlo simulations at a fixed θ , especially when considering that the simulated events are all single muons and the muon bundles actually passing through both detectors are 10 to 20 meters wide. Both data and simulation events were subjected to the trigger condition that at least eight OMs should be hit and distributed over at least two strings ('8/2' trigger).

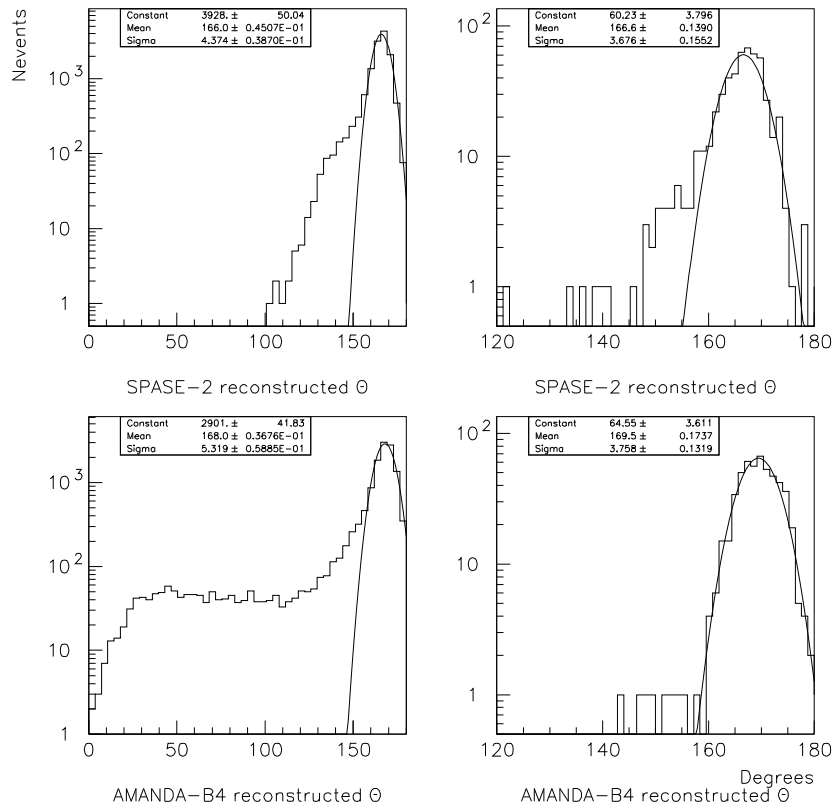


Figure 75: Comparison between coincidence-events reconstructed with the SPASE-2 reconstruction program and with STREC: on the left the θ distribution is shown subjected to the condition that at least two strings should be hit); on the right, a cut demanding that there should be at least five direct hits has been applied on both the SPASE and the STREC-reconstructed events.

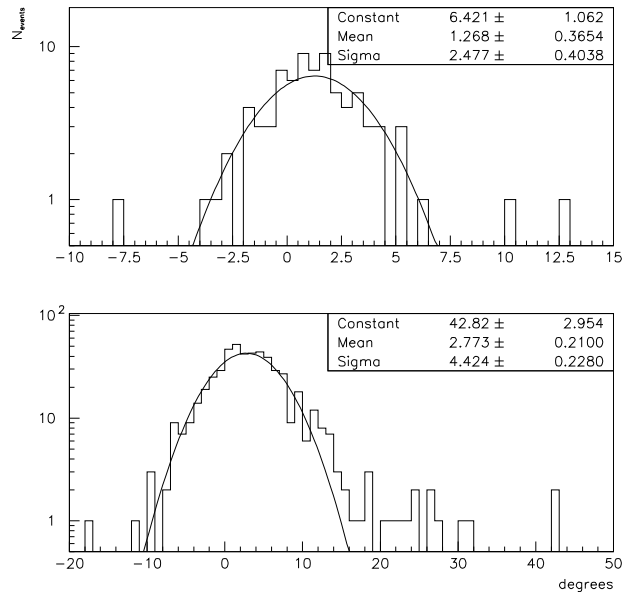


Figure 76: Top: $\theta_{rec} - \theta_{MC}$ for simulated atmospheric muons subjected to the following conditions: at least five residuals in the interval $[-15;15]$ ns, $163^\circ < \theta_{MC} < 172^\circ$, $20^\circ < \phi_{MC} < 110^\circ$. Bottom: $\theta_{rec} - \theta_{SPASE}$ with at least five residuals in the interval $[-15;15]$ ns

9.3 Search for atmospheric neutrinos

In this section, we will investigate what the data taken during six months in 1996 at the South Pole can be expected to yield with respect to atmospheric neutrinos. Atmospheric neutrinos are completely indistinguishable from point sources, but are interesting from the point of view of calibrating the detector. This can be done by comparing the observed upward-going events with a Monte Carlo simulation prediction.

For that purpose, input events to LOLITA were simulated using NUTOMU [79], a program producing the muon distribution resulting from a given flux of neutrinos, taking into account their scattering and absorption through the Earth. The atmospheric neutrino flux used in this study (see Fig. 77) was the one calculated by Lipari [11] and the neutrino-nucleon cross-section model was taken from Ritz et al. [80].

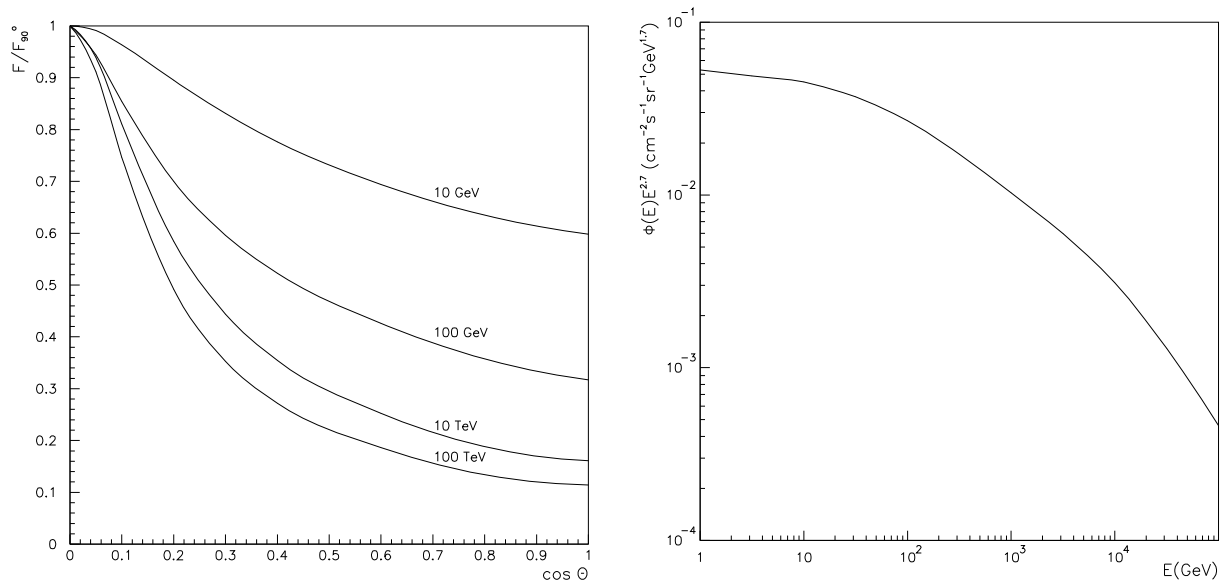


Figure 77: Left: Differential muon neutrino flux at sea level for several energies for up-going particles, normalized to the flux from the horizon. θ is the neutrino momentum's polar angle. Right: Differential flux at the horizon as function of energy.

Both the actual data and the simulated events were passed through the pre-filter, the chief purpose of this operation being to reduce the amount of events considerably in order to make the data more manageable, since in six months worth of data represents $4 \cdot 10^8$ events, which can hardly be reconstructed in a reasonable amount of time, let alone be simulated. Even so, this pre-filter was letting through too many events to be handled by STREC and harder cuts had to be applied.

Because of the thin and elongated geometry of the AMANDA-B4 array, true up-going events should have a time sequence of OM-hits going essentially in the positive z -direction. By making a simple linear fit of the depth versus time according to: $z = \alpha \cdot t + \beta$, where z is the position of a hit OM and t the time at which it was hit, and looking at the value of α , one should get a pretty good idea of the direction of a track. The parameter α , which has units m/ns can also be identified as the third component of the plane-wave or line-fit in Eq. 76.

As can be seen in Fig. 61, muons with angles $\theta \geq 40^\circ$ have a very low probability of getting well reconstructed anyway. Based on this observation, a cut was then applied on the variable α

in order to single out steep up-going tracks.

The α -distribution for different samples of events is shown for comparison in Fig. 78. For muons produced by atmospheric neutrinos, the whole distribution is shifted towards higher values of α relative to the same distribution for atmospheric muons. This effect is even more marked for muon resulting from the annihilation of neutralinos distributed in the center of the Earth. There are two main reasons for this:

- light from truly up-going muons will hit OMs at the bottom of the detector first and hit OMs located higher up only later. Atmospheric muons will yield a high value of α at random, e.g. in the case where a muon hits the bottom of the detector and another one from another bundle hits the top of a string later. Another possibility to get non-negative α -values is from all kinds of cascades, but those will tend to yield $\alpha \sim 0$ m/ns, since the light they produce propagates roughly isotropically.
- almost all of the OMs are facing down, and are thus getting more direct light from upward-going muons than from down-going ones. This results in more well-defined direction of propagation.

Fig. 78 also shows the cumulatives of the distributions mentioned above. To illustrate the effect of a cut on α , two lines are drawn at 0.15 m/ns and a little bit lower, at 0.1 m/ns. The amount of data that has to be handled is reduced greatly, but the percentage of expected atmospheric neutrino induced events with six direct hits surviving the cut is still quite high (30% for $\alpha \geq 0.15$ m/ns, 55% for $\alpha \geq 0.1$ m/ns).

After reconstruction, the average number of direct hits for the simulated atmospheric neutrino muons is high, but only two events in the data are left with six residuals in the interval $[-15, 15]$ ns. This is illustrated by Fig. 79, where the number of direct hits is histogrammed for both the full data set and the expectation for simulated atmospheric neutrino induced muon events in six months. The two events are displayed in Fig. 82. Both data and simulation were subjected to the following requirements:

- the events were pre-filtered.
- the events were reconstructed as upward-going tracks.
- the log-likelihood (per OM) of the reconstruction was less than 6 (which affected mainly the lower part of the distribution).
- they fulfilled a trigger of at least 8 modules hit, distributed over at least 2 strings
- they yielded $\alpha \geq 0.15$ m/ns

Attempts were made to process a larger amount of data, by lowering the cut on α to 0.1 m/ns prior to reconstruction, but no new events with six direct hits were found. Actually, the Monte Carlo simulation prediction for the number of events is $4.1 \pm 0.8_{(stat.)} \pm 0.9_{(syst.)}$ for $\alpha \geq 0.15$ m/ns whereas it is $5.3 \pm 0.9 \pm 1.2$ when no cut is made on α at all. The efficiency of this analysis for events with $N_{direct} \geq 6$ is 59% of that which would have been attained if no pre-filtering and no cut on α had been made, i.e. if every single event would had been reconstructed. This can be readily computed from table 17.

Studies of AMANDA-A coincidences show that the present uncertainty in the time calibration can induce a systematic average shift of ~ 15 ns for each module.

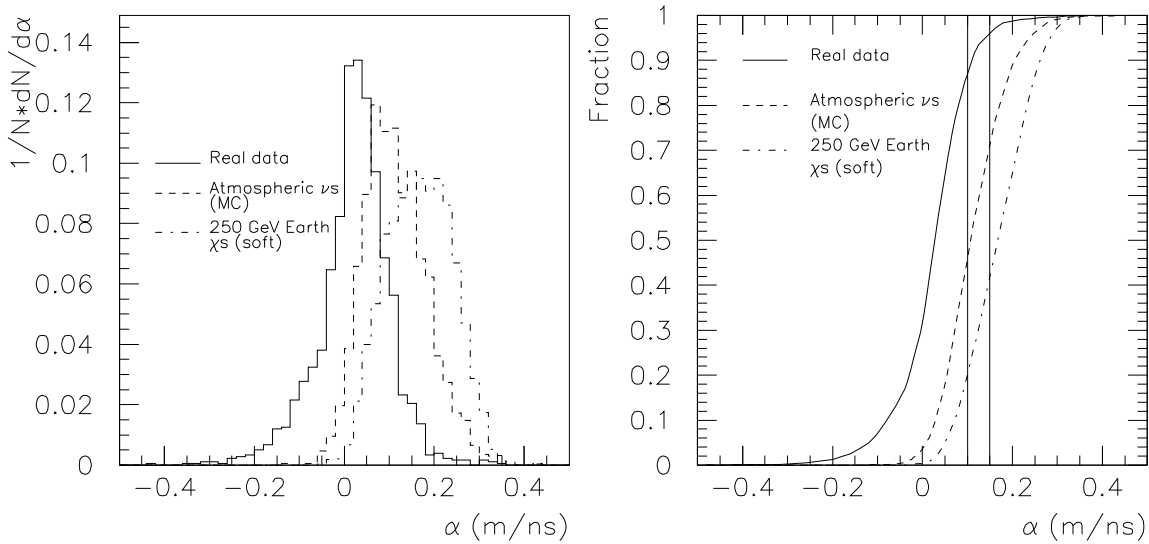


Figure 78: Left: probability distribution function of α for different sources after pre-filtering. Right: probability function of the same. Two lines illustrating the cuts at $\alpha = 0.1$ m/ns and $\alpha = 0.15$ m/ns are also displayed. All events are fulfilling the trigger condition 8/2

These deviations were estimated by making a fit of the hit-times of straight down-going tracks versus the corresponding OM-positions and equating them to the residuals of that fit. There is however no reason to change the estimated time resolution. How does this affect our calculations? We performed a new reconstruction of the simulated events after shifting the times by the deviations estimated above and got a reduction of the expected signal by nearly 50%. This underlines the importance of a careful time-calibration, even though impurities in the ice can induce time delays up to microseconds. However, the efficiency of the pre-filtering and α cut for events with 6 direct hits in this case is 58%, i.e. it remains unchanged.

The situation is summarized in table 17, which shows the predicted number of events together with their statistical and systematic errors. On top of the already mentioned uncertainties, we should keep in mind that the spread in muon-flux due to the differences between models for the atmospheric neutrino flux and the cross-sections is of the order of 40% [79] and that only one specific model was considered in this discussion.

The vast task of simulating enough fake events (i.e. events reconstructed as upward going, although they were really simulated as down going muons or cascades) is needed to estimate the background to the two up-going events found in the data. Note that the version of LOLITA used in this analysis did not include a detailed simulation of the DAQ (realistic pulse shapes, individual OM properties, etc.). However, we can still try to see if there are reasons to rule out the two events by comparing their characteristics with those of the expected signal. Fig. 80 shows

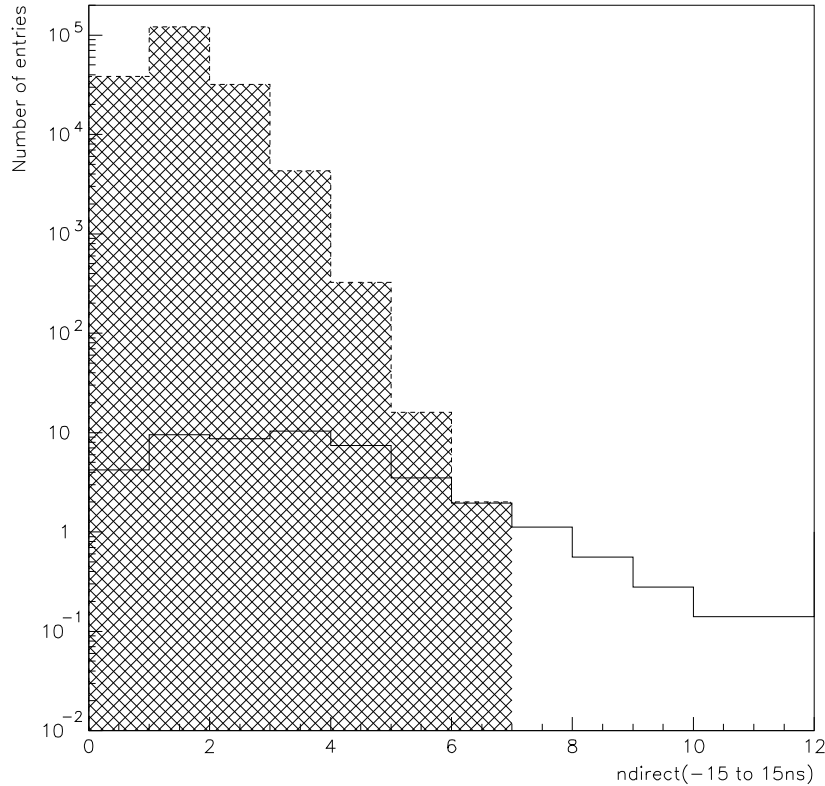


Figure 79: Number of events reconstructed as up-going as a function of the number of residuals in the interval [-15;15] ns (shaded area). Also shown is the corresponding expectation from LOLITA. Both samples contain 6 months worth of events and are subjected to an 8-2 trigger condition.

the following variables for simulated atmospheric neutrino induced muon events:

- the OM multiplicity
- the parameter α
- the number of residuals in the interval [-15;15] ns
- the log-likelihood per OM for the reconstructed track
- the string-multiplicity
- the track length

The events in the distributions displayed fulfill a cut $\alpha \geq 0.15$ m/ns and have at least six residuals in the interval [-15;15] ns. For comparison, table 18 can be consulted, listing the characteristics of the two candidate up-going events with 6 such direct hits. On no point the up-going candidates can be said to deviate from the expected main behaviour. Furthermore, the first event (#8427905) displays very large amplitude in most OMs, but no hits can be found in neighboring

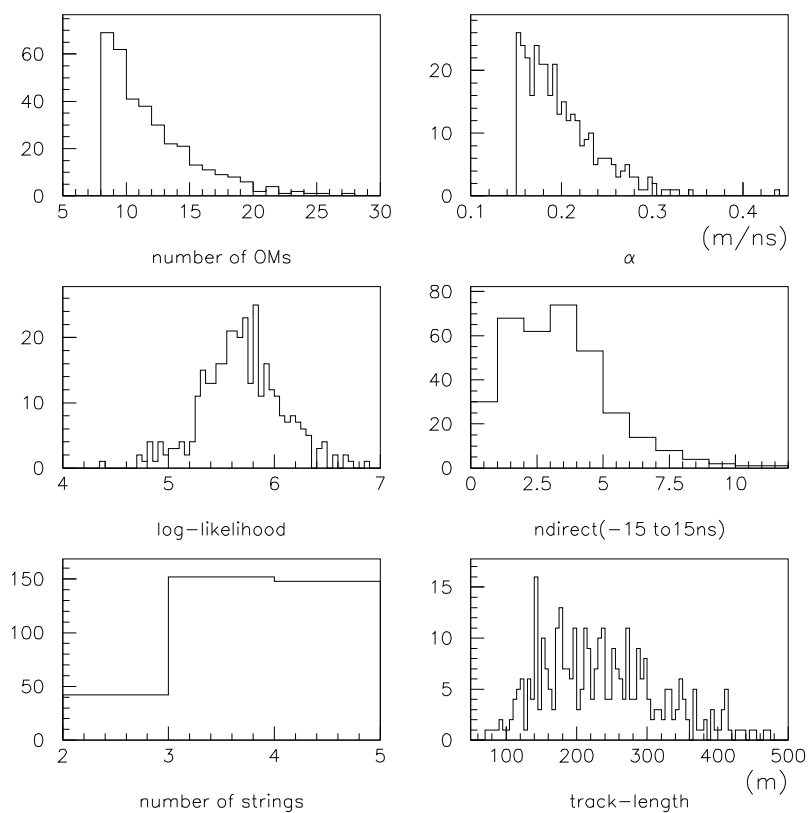


Figure 80: Distributions of several variables for muons produced by simulated atmospheric neutrinos.

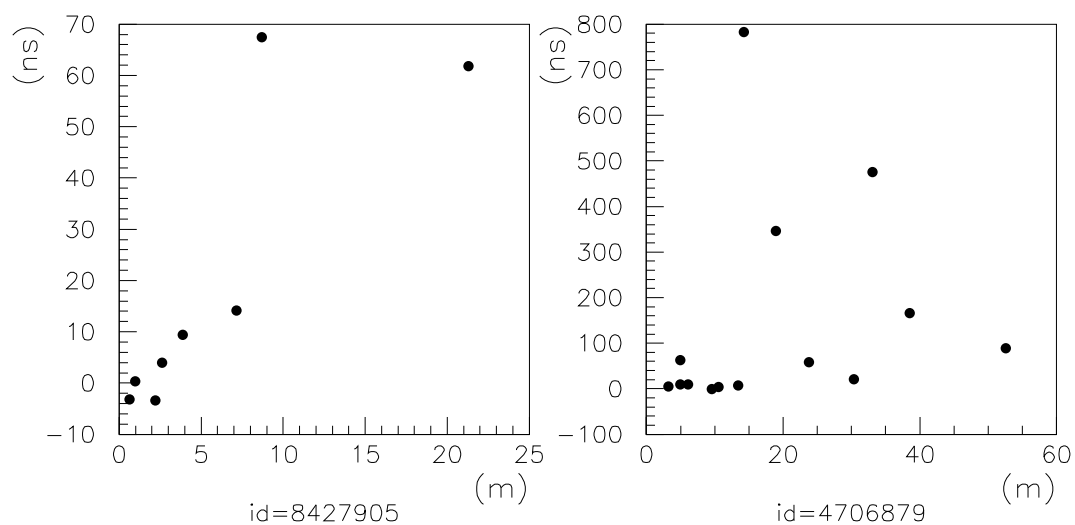


Figure 81: Time residuals versus the distance from the fitted track to the hit OMs for the two data events reconstructed as up-going muons.

Number of up-going atmospheric neutrino induced muons in 6 months				
Event sample	Pre-filter		No pre-filter	
	$\alpha \geq 0.15$ m/ns	$\alpha \geq 0.1$ m/ns	no α -cut	
LOLITA	$4.1 \pm 0.8 \pm 0.9$	$4.8 \pm 0.8 \pm 1.1$	$5.3 \pm 0.9 \pm 1.2$	$8.1 \pm 1.1 \pm 1.8$
LOLITA (smeared)	$2.8 \pm 0.6 \pm 0.6$	$2.9 \pm 0.6 \pm 0.6$	$3.2 \pm 0.7 \pm 0.7$	$5.0 \pm 0.8 \pm 1.1$
Data	2	2	-	-

Table 17: Comparison of the number events found in the data with 6 or more residuals in the interval $[-15.,15.]$ ns with Monte Carlo simulation expectations from LOLITA. In the second row, (smeared) indicates that the cable corrections used in the reconstruction were slightly different from those used in the simulation. Further conditions imposed on these pre-filtered events are that they should be reconstructed as up-going tracks with a likelihood/OM ≤ 6 and fulfill a trigger of 8-2

strings at the same depths. This would be very uncharacteristic for a point-like cascade sending out light isotropically. It is also not obvious to see how a down-going track could fake such a time sequence and give so high amplitudes. It is not unlikely for a neutrino-induced muon to start inside the detector, as this one seems to do: according to simulations [79], 7% of the tracks start inside the detector [81]. The second event (#4796879) exhibits smaller amplitudes, but passes through the whole detector and has a good residual vs. distance to OMs plot as well (see Fig 81).

Event ID#	4706879	8427905
α [m/ns]	0.19	0.37
Length [m]	295	182
Closest approach [m]	2.53	1.23
θ_{rec} [°]	14.1	4.6
ϕ_{rec} [°]	92.0	348.7
Likelihood/OM	5.9	4.2
OM multiplicity	14	8
String multiplicity	4	2

Table 18: Characteristics of the two events reconstructed as up-going muons.

9.4 Search for neutralinos from the center of the Earth

In this section we will take advantage of the AMANDA-B4 detector's relatively good efficiency for straight up-going tracks (see Fig. 61) in an attempt to put limits on the muon flux caused by neutralino annihilations in the center of the Earth.

An upper limit on the muon flux from neutralino annihilation at a 90% confidence level can be calculated as:

$$\phi_{\mu} = \frac{N_{90\%c.l.}}{A_{eff} \cdot T \cdot \eta} \quad (78)$$

where T is the 6 months of data taking, A_{eff} is the effective area and η is the fraction of events left after pre-filtering, a cut on $\alpha \geq 0.1$ m/ns and $N_{direct} \geq 6$.

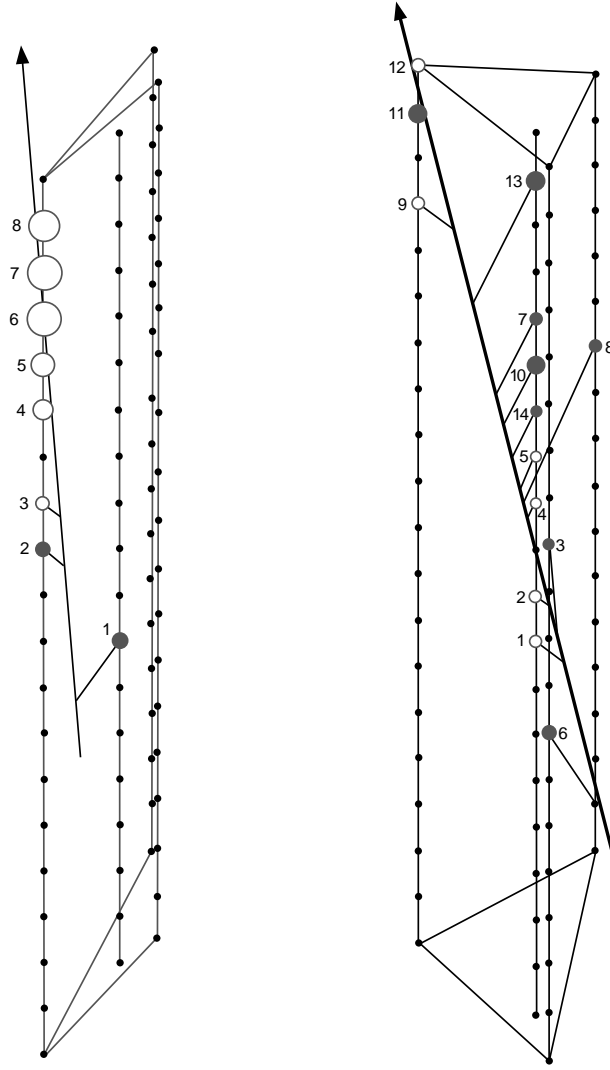


Figure 82: The two data events (left: ID#8427905, right: ID#4706879) reconstructed as up-going muons. The numbering of the modules refers to the time order in which they are hit and the white modules are those yielding a residual within $[-15,15]$ ns.

In order to calculate $N_{90\%c.l.}$ [8], we used the 2 observed events and the expected number of up-going muons produced by atmospheric neutrinos (see table 17) as an estimate of the background.

For the determination of η and A_{eff} , a neutrino-induced muon flux was simulated, resulting from neutralino annihilation at four different masses (50, 100, 250 and 500 GeV/c^2). The lightest neutralino (χ) in the minimal supersymmetric model was considered and two extreme cases of annihilation spectra were simulated using MUFLUX [82]: $\chi\chi \rightarrow b\bar{b}$ and $\chi\chi \rightarrow W^+W^-$. The first is referred to as the 'soft' channel, yielding neutrinos carrying away a small fraction of the neutralino mass, the second is called 'hard' and gives more energetic neutrinos. In the case where the neutralino mass m_χ is smaller than the W -boson mass, $\tau^+\tau^-$ was used instead of W^+W^- . Samples of 10^6 muons were simulated inside a large volume centered on the detector for each neutralino mass. They were all contained inside a cone with a half-opening angle of 15° [83].

The detector response to these muons was then simulated with LOLITA and the resulting

Event	String#	OM#	Distance [m]	Residual [ns]	Number of p.e.'s
4706879	1	1	3.2	4.7	1.5
	1	2	5.0	63.0	1.6
	1	4	13.4	8.0	1.2
	2	7	52.5	89.2	1.0
	3	9	30.4	19.1	1.3
	3	13	33.1	475.2	1.5
	4	2	38.5	165.8	2.3
	4	5	23.9	59.2	1.5
	4	6	19.0	347.5	1.6
	4	7	14.3	782.6	1.0
	4	8	9.5	-2.4	1.5
	4	9	5.0	8.3	1.2
	4	11	6.0	8.1	1.0
	4	12	10.7	3.2	1.1
8427905	3	2	2.6	4.0	8.5
	3	3	1.0	0.4	10.7
	3	4	0.6	-3.2	12.2
	3	5	2.2	-3.3	4.8
	3	6	3.9	10.0	3.2
	3	8	7.1	14.0	1.3
	3	9	8.8	67.5	1.3
	4	12	21.3	61.8	0.7

Table 19: Reconstruction details on an OM basis of the two filtered events reconstructed as up-going.

events reconstructed after pre-filtering and imposing firstly that they should satisfy a 8-2 trigger and secondly that they should yield $\alpha \geq 0.1$ m/ns. Demanding that each event should have at least 6 residuals in the interval $[-15;15]$ ns lead to a further reduction of the amount of simulated data (see table 20). The exposure is defined as $A_{eff} \cdot T \cdot \eta$.

The results are summarized for different neutralino masses and for the soft and hard annihilation channels in table 20. The strong dependence of the effective volume on the neutralino mass is reflected in the muon flux limits obtained. The pre-filter and filter vary also strongly with the assumed neutralino mass. Since the direction of the muons from neutralino annihilation is close to vertical, we divided the effective volume by the muon's mean range to estimate the effective areas.

The muon flux limits yielded are of the order of $1.8 \cdot 10^{-14}$ to $10^{-13} \text{cm}^{-2} \cdot \text{s}^{-1}$ for neutralino masses between 150 and 500 GeV/c^2 and increase greatly for neutralino masses lower than 150 GeV/c^2 , see Fig. 83.

For comparison, we mention the upper limits obtained by BAIKAL [84] ($10^{-13} \text{cm}^{-2} \text{s}^{-1}$), BAKSAN [85] ($5 - 9 \cdot 10^{-15} \text{cm}^{-2} \text{s}^{-1}$ for $m_\chi \geq 100 \text{ GeV}$), MACRO [86] ($6.0 \cdot 10^{-15} - 2.7 \cdot 10^{-14} \text{cm}^{-2} \text{s}^{-1}$ in a window of $5 - 30^\circ$ for $m_\chi \geq 1.5 \text{ GeV}$) and Kamiokande [87] ($4 \cdot 10^{-14} \text{cm}^{-2} \text{s}^{-1}$).

The limit of $10^{-13} \text{cm}^{-2} \text{s}^{-1}$ is exceeded in the soft channel for neutralino masses below $\sim 150 \text{ GeV}/c^2$, corresponding to a mean muon energy of about 50 GeV, which can be taken as our

threshold for an AMANDA-B4 search of this kind.

However, as it was mentioned in section 9.3, we have an uncertainty in the time-calibration of the detector. Using the corrections estimated from A-B coincidences, we find the new limits shown in table 21 and Fig. 83. The performance is degraded by about a factor 2.5 for the high neutralino masses. The previously observed dependences on energy are still there. Even so, the limits reached with only 6 months worth of live time data are competitive.

There is good hope though, that calibration results can be assessed better in the future, allowing us to re-gain a possible loss in efficiency. The data analyzed so far has been increased in 1997 with the events collected by AMANDA-B10. The conditions were very different and so it is difficult to make an estimate of how the limits will be improved by putting together present results with those from an anticipated analysis. The main difference is that the trigger in 1997 was set to 16/1, which would raise the threshold to higher energies for strings 1–4, whereas the remaining ones should yield an effective area/string comparable to that achieved in the 1996 data. This is because the later was taken with a trigger of 8/1 and a spacing of 20 m between OMs in a same string and the six added strings have a spacing of only 10 m.

Better results could yet be achieved by designing a dedicated sub-trigger with lower multiplicity, but requiring that the time order between several neighbours in one string should be up-going. Such a study is underway.

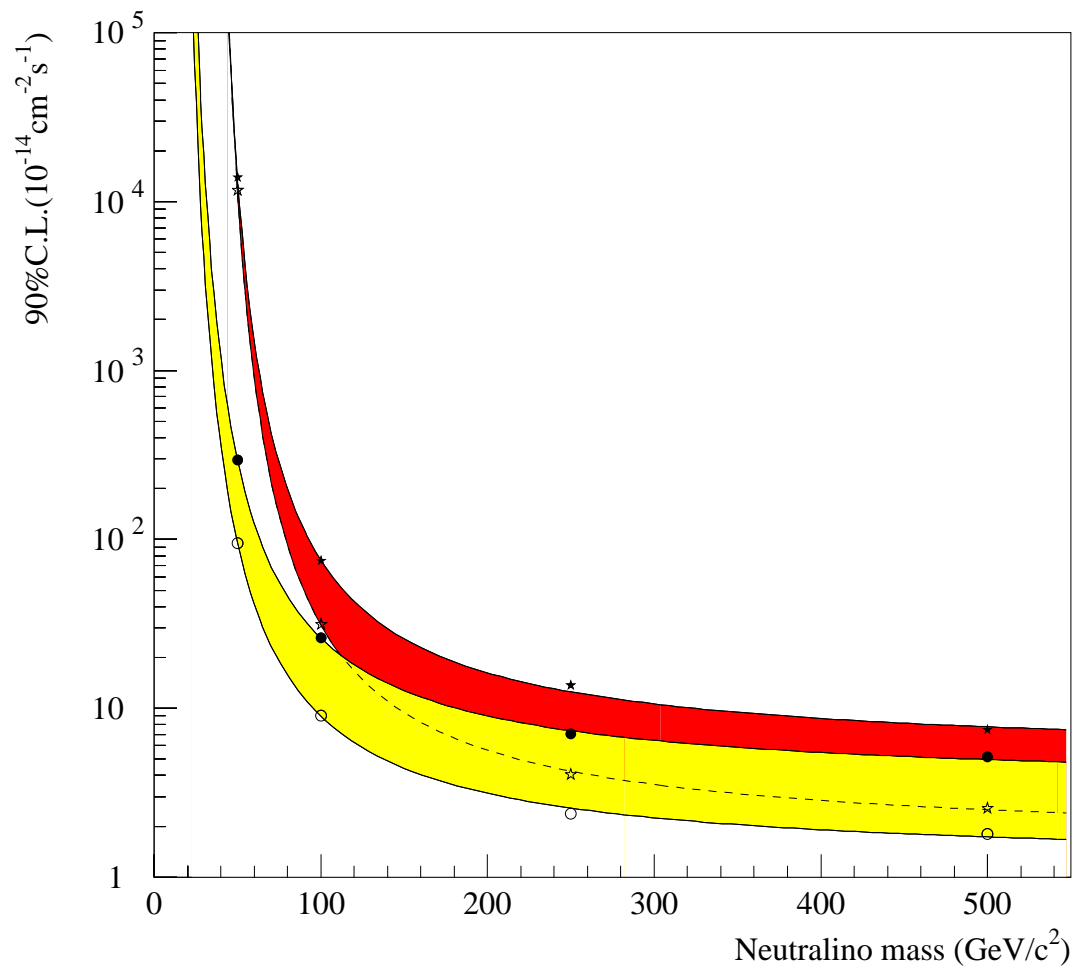


Figure 83: Upper limit at the 90% confidence level on the muon flux from the center of the Earth as a function of the neutralino mass. The light colored band represents the hard annihilation channel and the dark one represents the soft annihilation channel. Assuming that the detector is correctly time-calibrated yields the limits set by the bottom edge of each band. Time smearing the calibrated t_0 values by ~ 15 ns yields the top edge.

Neutralino mass [GeV/c ²]	50		100		250		500	
Type of spectrum	Soft	Hard	Soft	Hard	Soft	Hard	Soft	Hard
Generated volume [m ³]	200 *200 *1000	200 *200 *1000	500 *500 *1000	500 *500 *1000	500 *500 *1000	500 *500 *1000	800 *800 *2000	800 *800 *2000
Triggers	710	1970	499	2026	4315	14424	1853	5849
Effective volume [10 ⁶ · m ³]	0.0284	0.0788	0.125	0.506	1.08	3.61	2.37	7.49
Mean muon energy [GeV]	18.3	25.9	31.5	47.31	60.0	127.6	100.7	255.6
$\langle \cos\theta \rangle$	0.9948	0.9953	0.9965	0.9970	0.9979	0.9986	0.9987	0.9993
Percentage of pre-filtered events left	35	44	48	59	66	52	65	69
Percentage with at least 6 direct hits and $\alpha \geq 0.1$ m/ns	1.7	8	17	18	21	29	26	28
90% CL upper limit on the volumetric muon flux [10 ⁻¹³ · m ⁻³ s ⁻¹]	12760	732	198.51	37.74	13.62	3.73	5.07	1.40
90% CL upper limit on the muon flux [10 ⁻¹⁴ · cm ⁻² s ⁻¹]	11651	95.18	31.26	9.03	4.06	2.38	2.55	1.8
Detector exposure [m ² · year]	1.4	11	32	113	249	427	398	567

Table 20: Summing up of the conditions of simulations and results. All simulations were made with 10⁶ muons. Also shown are the effects of the successive filters and cuts on the number of events and the resulting upper limit on the muon fluxes at a 90% confidence level.

Neutralino mass [GeV/c ²]	50		100		250		500	
Type of spectrum	Soft	Hard	Soft	Hard	Soft	Hard	Soft	Hard
Generated volume [m ³]	200 *200 *1000	200 *200 *1000	500 *500 *1000	500 *500 *1000	500 *500 *1000	500 *500 *1000	800 *800 *2000	800 *800 *2000
Triggers	710	1970	499	2026	4315	14424	1853	5849
Effective volume [10 ⁶ · m ³]	0.0284	0.0788	0.125	0.506	1.08	3.61	2.37	7.49
Mean muon energy [GeV]	18.3	25.9	31.5	47.31	60.0	127.6	100.7	255.6
$\langle \cos\theta \rangle$	0.9948	0.9953	0.9965	0.9970	0.9979	0.9986	0.9987	0.9993
Percentage of pre-filtered events left	35	44	48	59	66	52	65	69
Percentage with at least 6 direct hits and $\alpha \geq 0.1$ m/ns	1.6	2.8	8	7	7	12	10	11
90% CL upper limit on the volumetric muon flux [10 ⁻¹³ · m ⁻³ s ⁻¹]	15251	2272	477.23	109.85	45.69	10.15	14.86	4.02
90% CL upper limit on the muon flux [10 ⁻¹⁴ · cm ⁻² s ⁻¹]	13926	295	74.77	26.12	13.71	7.06	7.47	5.14
Detector exposure [m ² · year]	1.3	4	15	44	83	177	153	223

Table 21: Summing up of the conditions of simulations and results. All simulations were made with 10^6 muons. Also shown are the effects of the successive filters and cuts on the number of events and the resulting upper limit on the muon fluxes at a 90% confidence level. In this table, the times obtained from the Monte Carlo simulations have been shifted according to our present estimates of the errors in the calibrated t_0 values.

10 Conclusions

A position calibration of the four string AMANDA detector has been made, using laser data, and verified against drill-logging data. The combined results give the detector geometry with an accuracy of 2 m over 2 km depth.

A muon track reconstruction program, STREC, has been developed as an essential analysis tool and used on the data collected during 1996. A good agreement with the SPASE-2 reconstruction of down-going atmospheric muons was found, providing confidence about the resolution of the detector (a few degrees, depending on the declination angle).

The shape of the AMANDA-B4 detector geometry had been optimized for probing the ice quality in a wide range of depths, making it efficient essentially for straight up-going muons. This made it possible to exploit it to a large fraction of its full capacity by strongly filtering out down-going tracks. A series of such filters was used in order to discriminate against the large background of atmospheric muons, prior to reconstructing the events.

A search for up-going neutrinos yielded two events. The expectation value given by a similar analysis made on Monte Carlo simulated events lies between $2.9 \pm 0.6 \pm 0.6$ and $4.8 \pm 0.8 \pm 1.1$, depending on the systematic errors in the time calibration of the optical modules.

Limits were calculated for the neutrino induced muon flux, produced by annihilations in the center of the Earth of the lightest neutralino in the MSSM. Upper limits at the 90% confidence level on the resulting muon flux were calculated using our current estimate (15 ns) of the systematic error in the time calibration. The limit in this case is $5.14 \cdot 10^{-14} - 2.6 \cdot 10^{-13} \text{ cm}^{-2} \text{ s}^{-1}$ for $150 \text{ GeV}/c^2 < m_\chi < 500 \text{ GeV}/c^2$. An improved detector time calibration is underway, which could bring this limit down to $1.8 - 9 \cdot 10^{-14} \text{ cm}^{-2} \text{ s}^{-1}$ which is our result for a negligible error on the time measurements. These limits correspond to the annihilation channel yielding the highest neutrino energies (see section 9 for the treatment of a channel resulting in lower energies).

Acknowledgments

I express my gratitude to my supervisor Prof. Per Olof Hulth who has encouraged and supported this work, as well as engaged in long and fruitful discussions with me. Many thanks also to Prof. Sven-Olof Holmgren who has provided me with support and advice over the years.

This work owes much to Eduardo Andres for his help with the data handling and with the Monte Carlo simulations.

I would like to extend my gratitude to Eva Dalberg, Dr. Ariel Goobar and Dr. Joakim Edsjö for their help and assistance with essential parts of the analysis.

I also thank Dr. Christian Walck, for helping me with the understanding of statistics in physics. Many thanks also to Lars Thollander, Dr. Staffan Carius and Dr. Allan Hallgren for their help with hardware issues.

I greatly benefited from my contacts with the non-Swedish part of the collaboration, especially from the experience and patience of Dr. Serap Tilav, Dr. Rodin Porrata and S. Hundertmark.

I would also like to thank Dr. Carlos Perez de los Heros for the time spent correcting this thesis and for his kind and numerous suggestions for improvement.

I am greatly indebted to my collaborators and to the funding agencies for their support in building and operating the AMANDA detector, and to all people working at the Scott-Amundsen base for the excellent quality of their work.

References

- [1] E. Andrés, P. Askebjerg and C. Pérez de los Heros, *LOLITA, a simulation program for AMANDA* Stockholm University internal report (1997)
- [2] P. K. F. Grieder et al., *The DUMAND stage II detector and its capabilities*, Adelaide 1990, Proceedings, Cosmic ray, vol. **4** (1990) 357-360.
- [3] R. J. Wilkes, *DUMAND and AMANDA: high-energy neutrino astrophysics*, Proceedings of 22nd Annual SLAC Summer Institute on Particle Physics: Particle Physics, Astrophysics and Cosmology (1994).
- [4] I. Sokalski and Ch. Spiering (eds.), *The BAIKAL neutrino telescope NT-200, project description*, BAIKAL note 92-03.
- [5] F. Blanc et al., *Towards a large scale high-energy cosmic neutrino undersea detector*, CPPM-97-02, (May 1997).
- [6] L. K. Resvanis (ed.), *in*, Proceedings of the NESTOR workshop, Pylos 1992 and 1993, university of Athens, 1993/94.
- [7] T. K. Gaisser, *Cosmic rays and particle physics*, Cambridge University Press, 1992.
- [8] Particle data group, *Review of particle properties*, Phys. Rev. **D50** (1994) 3.
- [9] M. Thunman, *A Monte Carlo calculation of muon and neutrino fluxes from atmospheric cosmic ray interactions*, Licenciat thesis, Uppsala University, The Svedberg laboratory and department of radiation sciences, TSL/ISV-94-0097, (May 1994)
- [10] T. K. Gaisser, F. Halzen and T. Stanev, *Particle astrophysics with high energy neutrinos*, Physics Reports, **258** (1995) 175-236.
- [11] P. Lipari, *lepton spectra in the Earth's atmosphere*, Astropart. Phys. **1** (1993) 195-227.
- [12] R. Becker-Szendy et al., *The electron-neutrino and muon-neutrino content of the atmospheric flux*. Phys. Rev. **D 46** (1992) 3720–3724.
- [13] W. W. M. Allison et al., Phys. Lett. **B 391** (1997) 491–500.
- [14] Y. Fukuda et al., *Atmospheric muon-neutrino/ electron-neutrino ratio in the multi-GeV energy range*. Phys. Lett. **B 335** (1994) 237–245.
- [15] M. Aglietta et al., *Experimental study of atmospheric neutrino flux in the NUSEX experiment*. Europhysics Letters **8** (1989) 611; Physics Letters **B 280** (1992) 146.
- [16] K. Daum et al. *Determination of the atmospheric neutrino spectra with the Frejus detector*. Z. Phys. **C 66** (1995) 417-428.
- [17] T. C. Weekes et al., *Observation of TeV gamma rays from the Crab Nebula using the atmospheric Cherenkov imaging technique*, Astrophys. J. **342** (1989) 379–395.
- [18] F. W. Stecker and M. H. Salamon, *High-energy neutrinos from active galactic nuclei*, Phys.Rev.Lett. **66** (1991) 2697-2700, Erratum-ibid. **69** (1992) 2738.
- [19] W. Bednarek and R. J. Protheroe, *Gamma-rays and neutrinos from relativistic protons accelerated by magnetic reconnection on an AGN accretion disk*, Proceedings of the 25th International Conference on Cosmic Rays, Durban, South Africa, July 30 – August 6, (1997), OG 4.4.3., vol.3, 313.
- [20] A. Biron et al., *Upgrade of AMANDA-B towards AMANDA-II*, Submitted to the Physics Research Committee, DESY, PRC 97/05, (June 1997).
- [21] M. Punch et al., *Detection of TeV photons from the active galaxy Markarian 421*, Nature **358** (1992) 477.
- [22] F. W. Stecker, *Extragalactic high energy neutrino and gamma-ray astronomy in Particle astrophysics (Fourth "Rencontres de Blois")*, edited by G. Fontaine and J. Trân Tranh Vân, Editions Frontières (1993) 111–122.
- [23] R. Porrata, *The energy spectrum of point-like events in AMANDA-A*, Ph. D. Thesis, University of California, Irvine (1997).

- [24] S. L. Glashow, *Resonant scattering of antineutrinos*, Phys. Rev. **118** (1960) 316.
- [25] L. Bergström, J. Edsjö and P. Gondolo, *Indirect neutralino detection rates in neutrino telescopes*, Phys. Rev. **D 55** (1997) 1765.
- [26] C. H. Wiebusch, *The detection of faint light in deep underwater neutrino telescopes*, Ph. D. Thesis, PITH 95/37, Physics Institute RWTH Aachen (December 1995).
- [27] P. Antonioli, C. Ghetti, E. B. Korolkova, V. A. Kudyavtsev and G. Sartorelli *A three-dimensional code for muon propagation through the rock: MUSIC*, Astropart. Phys. **7** (1997) 357-368.
- [28] R. Gandhi, C. Quigg, M. H. Reno and I. Sarcevic, *Ultra-high-energy neutrino interaction*, Phys. Rev. Lett. **66** (1991) 2697-2700.
- [29] T. Ferbel, *Experimental techniques in high energy physics*, Frontiers in physics – Addison-Wesley, 1987.
- [30] R. K. Bock, H. Grote, D. Notz and M. Regler, *Data analysis techniques for high-energy physics experiments*, Cambridge University Press, 1990.
- [31] Q. Sun, *The electromagnetic shower library for the Stockholm AMANDA Monte Carlo program*, USIP-96-05, Stockholm University (May 1996).
- [32] K. Kleinknecht, *Detectors for particle radiation*, Cambridge University Press, 1986.
- [33] D. H. Perkins, *Introduction to high energy physics*, Addison-Wesley publishing company, 1982.
- [34] G. M. Frichter et al., *Toward radio detection of PeV neutrinos on the cubic kilometer scale*, Proc. of the 7th Int. Workshop on Neutrino Telescopes, Venice, Italy, February 27 – March 1, (1996).
- [35] A. Richards, Presented at the AMANDA collaboration meeting in Zeuthen, June 1996.
- [36] L. Thollander, Private communication.
- [37] S. Carius, Private communication.
- [38] J. Öhrmalm, *Effects of the magnetic field on the AMANDA optical module and pulse-height and time-over-threshold distributions of the PMT signal for 1pe, 2pe and 3pe events*, Diploma thesis, Uppsala University, The Svedberg laboratory and department of radiation sciences, TSL/ISV-97-0174, (April 1997).
- [39] A. Goobar, Private communication.
- [40] C. H. Wiebusch, *Preliminary results on the angular response of the AMANDA optical module*, Internal AMANDA report (March 1996).
- [41] C. Spiering, *Improvement of photomultiplier sensitivities to Cherenkov light*, PHE84-05, Zeuthen (1984).
- [42] J. Klug, *Enhancement of the up/down signal ratio and cross-talk studies in AMANDA*, Diploma thesis, Uppsala University, The Svedberg laboratory and department of radiation sciences, ISV-9/1997, (October 1997).
- [43] L. Gustafsson, P. Marciniewski and A. Zernov, *MADD – a fast multiplicity trigger system*, Nucl. Inst. and Meth. **A 379** (1996) 335-340.
- [44] S. N. Bosiev et al., INR-Preprint P-0630 (1989).
- [45] W. Lohmann, R. Kopp and R. Voss, *Energy loss of muons in the energy range 1-10000 GeV*, Yellow report CERN 85-03 (March 1985).
- [46] S. Hundertmark, *AMASIM, Simulation tool for AMANDA*, <http://www.ifh.de/hundert/amanda/amasim/amasim.html>.
- [47] S. Hundertmark, *Simulation des AMANDA-Detektors und Auswertung der Myonendaten*, Ph. D Thesis, to be presented in 1998.
- [48] P. B. Price, *Kinetics of conversion of air hydrate crystals in Antarctic ice*, Science **267** (1995) 1802–1804.
- [49] N. I. Barkov and V. Ya. Lipenkoy, Mater. Glyatsiolog. Issled. **51** (1985) 178.

- [50] A. J. Gow and T. Williamson, *J. Geophys. Res.* **80** (1975) 5101.
- [51] T. Miller et al., Proceedings of the 23rd International Conference on Cosmic Rays, Calgary, Canada, 19-30 July 1993, D. A. Leahy et al. (Eds.), Vol 4, World Scientific, Singapore (1993) 557.
- [52] S. Chandrasekhar, *Stochastic problems in physics and astronomy*, *Rev. Mod. Phys.* **15** (1942) 1.
- [53] A. Ishimaru, *Diffusion of a particle in densely distributed scatterers*, *J. Opt. Soc. Am.* **68** (1978) 1045.
- [54] P. Askebjerg et al., *Optical properties of the South Pole ice at depths between 0.8 and 1 kilometer*, *Science* **267** (1995) 1147.
- [55] D. J. Pine et al., *Dynamical correlations of multiply scattered light*, in *Scattering and localization of classical waves in random media*, edited by Ping Sheng, Singapore, Teaneck, NJ, World Scientific (1990) 312-370.
- [56] P. Askebjerg et al., *UV and optical light transmission properties in deep ice at the South Pole*, *Geophys. Res. Lett.* **24** (1997) 1355-1358.
- [57] S. Tilav et al., *Indirect evidence for long absorption lengths in Antarctica ice*, Proceedings of the 24th International Cosmic Ray Conference, Rome, Vol. **1** (1995) 1011.
- [58] T. C. Grenfell and D. K. Perovich, *Radiation absorption coefficients of polycrystalline ice from 400-1400 nm*, *J. Geophys. Res.* **86** (1981) 7447.
- [59] D. K. Perovich and J. W. Govoni, *Absorption coefficients of ice from 250-400 nm*, *J. Geophys. Res.* **18** (1991) 1233.
- [60] A. G. Frodesen, O. Skjeggstad and H. Tøfte, *Probability and statistics in particle physics*, Universitetsforlaget, 1979.
- [61] R. Porrata, for the AMANDA collaboration, *Analysis of cascades in AMANDA-A*, Proceedings of the 25th International Conference on Cosmic Rays, Durban, South Africa, July 30 – August 6, (1997), HE 4.1.4, vol.7, 9.
- [62] S. Tilav, for the AMANDA collaboration, *First look at AMANDA-B data*, Proceedings of the 25th International Conference on Cosmic Rays, Durban, South Africa, July 30 – August 6, (1997), HE 4.1.2, vol.7, 5.
- [63] A. Richards and K. Woschnagg, *South Pole deep ice properties at $\lambda = 337$ nm*. AMANDA internal report (1997).
- [64] D. M. Lowder, *Attenuation studies using AMANDA calibration sources*. AMANDA internal report (1996).
- [65] S. G. Warren, *Optical constants of ice from the UV to the microwave*, *Applied Optics* **23** (1984) 1206.
- [66] M. Carlson et al., *A position calibration of the AMANDA-B detector using drill data*, Internal AMANDA report (1996).
- [67] A. Bouchta, *A preliminary position calibration of the AMANDA-B detector*, USIP Report 97-02 (1997).
- [68] S. Tilav, *Some facts about the AMANDA-B muon data*, Internal AMANDA report (June 1996).
Astropart. Phys. **7** (1997) 109-124.
- [69] C. H. Wiebusch, for the AMANDA collaboration, *Muon reconstruction with AMANDA-B*, Proceedings of the 25th International Conference on Cosmic Rays, Durban, South Africa, July 30 – August 6, (1997), HE 4.1.5, vol.7, 13-16.
- [70] W. H. Press, S. A. Teukolsky, W. A. Vetterling and B. P. Flannery, *Numerical recipes in FORTRAN: the art of scientific computing, second edition*, Cambridge University Press, 1992.
- [71] G. Dahlquist and A. Björck, *Numerical methods*, Prentice-Hall series in automatic computation, 1974.
- [72] D. Cvijović and J. Klinowski, *Taboo search: an approach to the multiple minima problem*, *Science* **267** (1995) 664.
- [73] V. J. Stenger. *Track fitting for the DUMAND II octagon array*. University of Hawaii, HDC-1-90.

- [74] J. E. Jacobsen, *Simulating the detection of muons and neutrinos in deep Antarctic ice*, Ph. D. Thesis, University of Wisconsin (1996).
- [75] M. Ambrosio et al., *Seasonal variations in the underground muon intensity as seen by MACRO*,
- [76] T. C. Miller for the SPASE collaboration and the AMANDA collaboration, *Analysis of SPASE-AMANDA coincidence events*, Proceedings of the 25th International Conference on Cosmic Rays, Durban, South Africa, July 30–August 6, (1997), HE 10.4.9, vol. 5, 237–240.
- [77] T. K. Gaisser et al., *The new South Pole air shower experiment – SPASE 2*, Proceedings of the 24th International Conference on Cosmic Rays, Rome, Italy, 28 August - 8 September, (1995), HE 7.1.7, p. 938.
- [78] J. E. Dickinson, *The performance of SPASE-2*, Proceedings of the 25th International Conference on Cosmic Rays, Durban, South Africa, July 30 – August 6 1997, OG 10.4.8, vol. 5, p. 233.
- [79] E. Dalberg, *A Monte-Carlo study of atmospheric muon-neutrinos in AMANDA*, Licenciat thesis, USIP Report 98-02, Stockholm University, Fysikum, (December 1997).
- [80] S. Ritz and D. Seckel, *Detailed neutrino spectra from cold dark matter annihilations in the Sun*, Nucl. Phys. **B 304** (1988) 877-908.
- [81] E. Dalberg, Private communication.
- [82] *MUFLUX code written by J. Edsjö, implemented as an event generator by A. Goobar*; see also L. Bergström, J. Edsjö and P. Gondolo, *Indirect neutralino detection rates in neutrino telescopes*, Phys. Rev. **D 55** (1997) 1765.
- [83] J. Edsjö, *Aspects of neutrino detection of neutralino dark matter* Ph. D. Thesis, Uppsala University (1997)
- [84] L. Kuzmichev for the BAIKAL collaboration, *Search for neutrinos from the core of the Earth with the BAIKAL underwater detector NT-36*, Proceedings of the 25th International Conference on Cosmic Rays, Durban, South Africa, July 30– August 6 1997, HE 5.2.3.
- [85] O. Suvorova et al., *Baksan neutralino search* Presented at the first international workshop on non-accelerator new physics (NANP97), Dubna, Russia, July 7-12, (1997)
- [86] T. Montaruli for the MACRO collaboration, *Indirect search for WIMPs with the MACRO detector*, Proceedings of the 25th International Conference on Cosmic Rays, Durban, South Africa, July 30– August 6 1997, HE 5.3.2..
- [87] M. Mori et al., *Search for neutralino dark matter heavier than the W boson at Kamiokande*, Phys. Rev. **D48** (1993) 5505.

Appendix

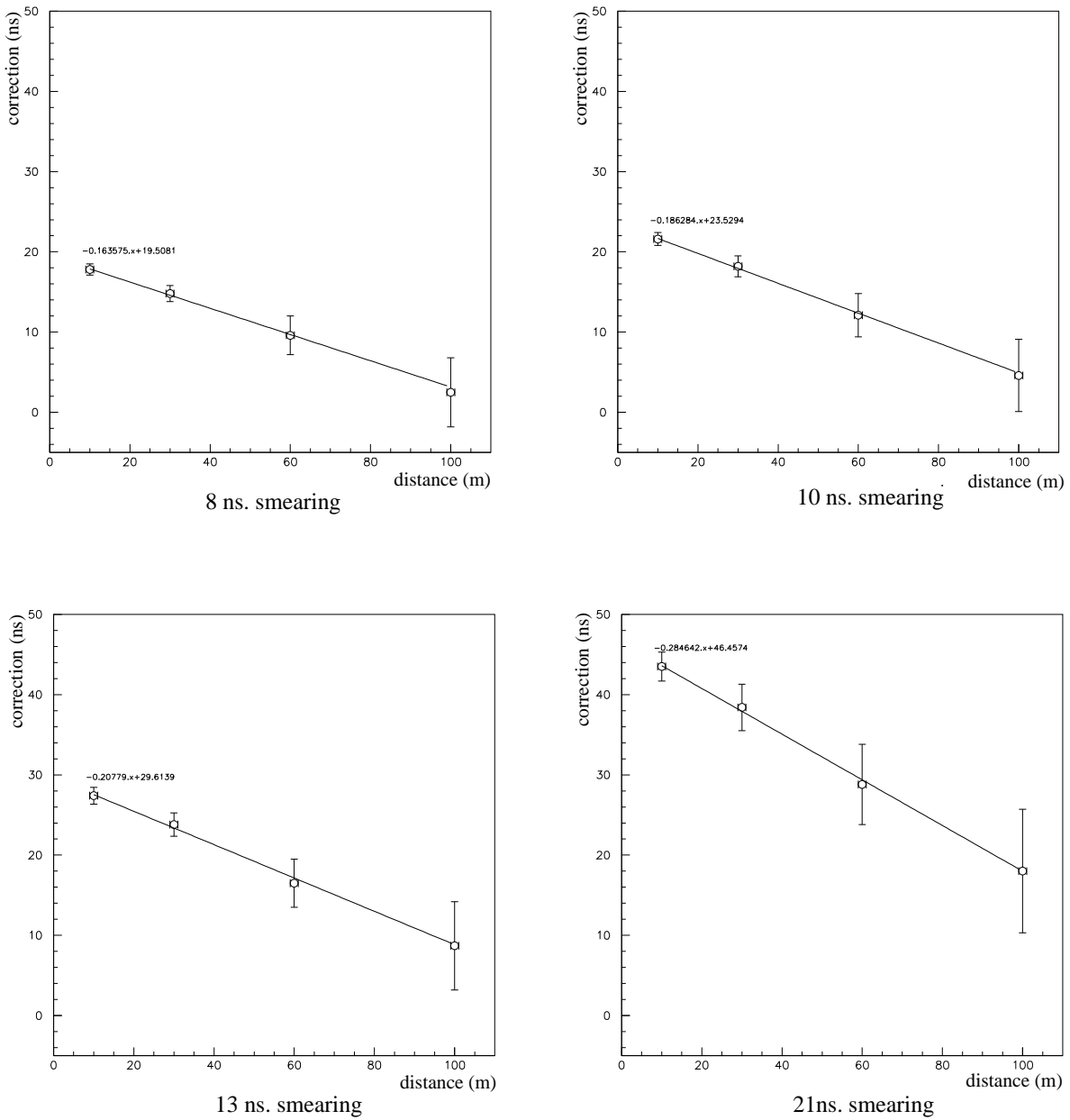


Figure 84: Time corrections for different time smearings with statistical errors. The Monte-Carlo batches used contained 1000 events each.

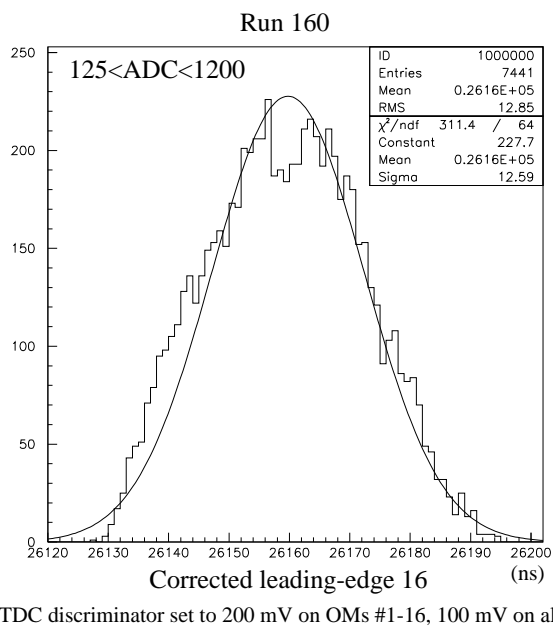
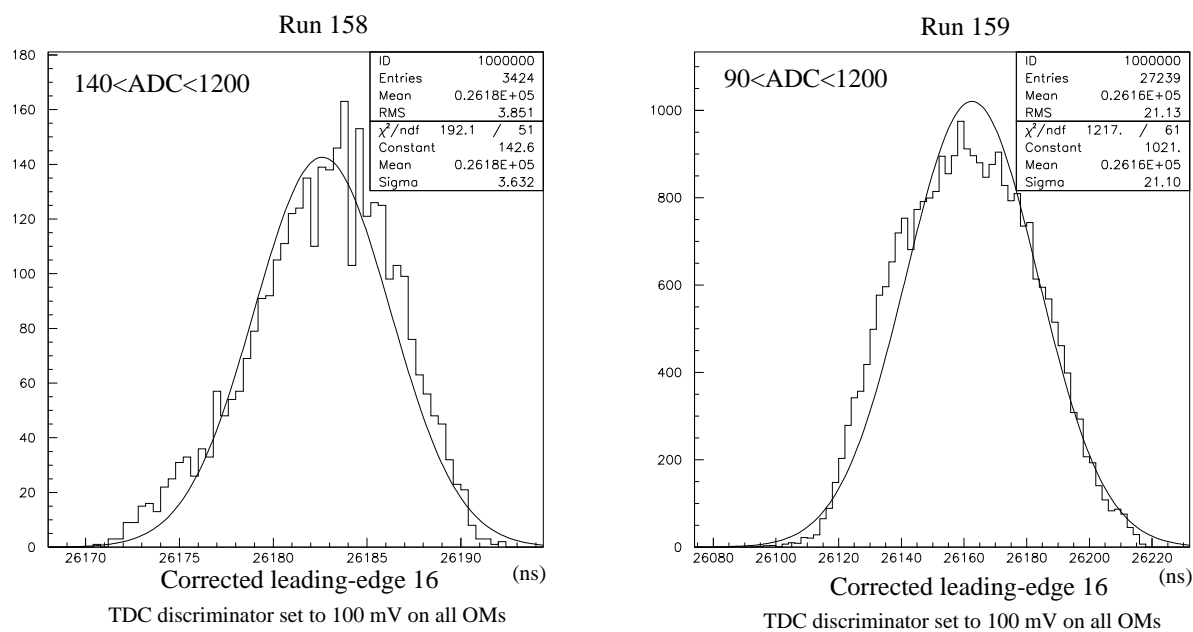


Figure 85: Time smearing of OM16 in three different laser runs

Em. string	Em. module	Rec. string	Rec. module	Distance [m]	Nominal distance [m]
1	16	1	11	115.8	110.0
1	16	1	12	92.6	90.0
1	16	1	20	77.0	70.0
1	16	2	10	165.3	147.6
1	16	2	11	141.0	130.3
1	16	2	13	106.6	98.9
1	16	2	14	92.9	85.9
1	16	2	15	83.7	76.0
1	16	2	16	81.0	70.6
1	16	2	17	80.3	70.6
1	16	2	18	85.2	76.0
1	16	3	11	91.1	84.8
1	16	3	14	67.9	59.9
1	16	3	15	71.5	63.2
1	16	3	16	80.2	72.1
1	16	3	18	112.8	100.0
1	16	3	19	128.0	116.6
1	16	3	20	152.1	134.1
1	16	4	10	113.6	107.7
1	16	4	11	96.7	89.4
1	16	4	15	50.0	40.0
1	16	4	16	59.6	44.7
1	16	4	17	66.9	56.6

Table 22: Corrected measurements for run 158

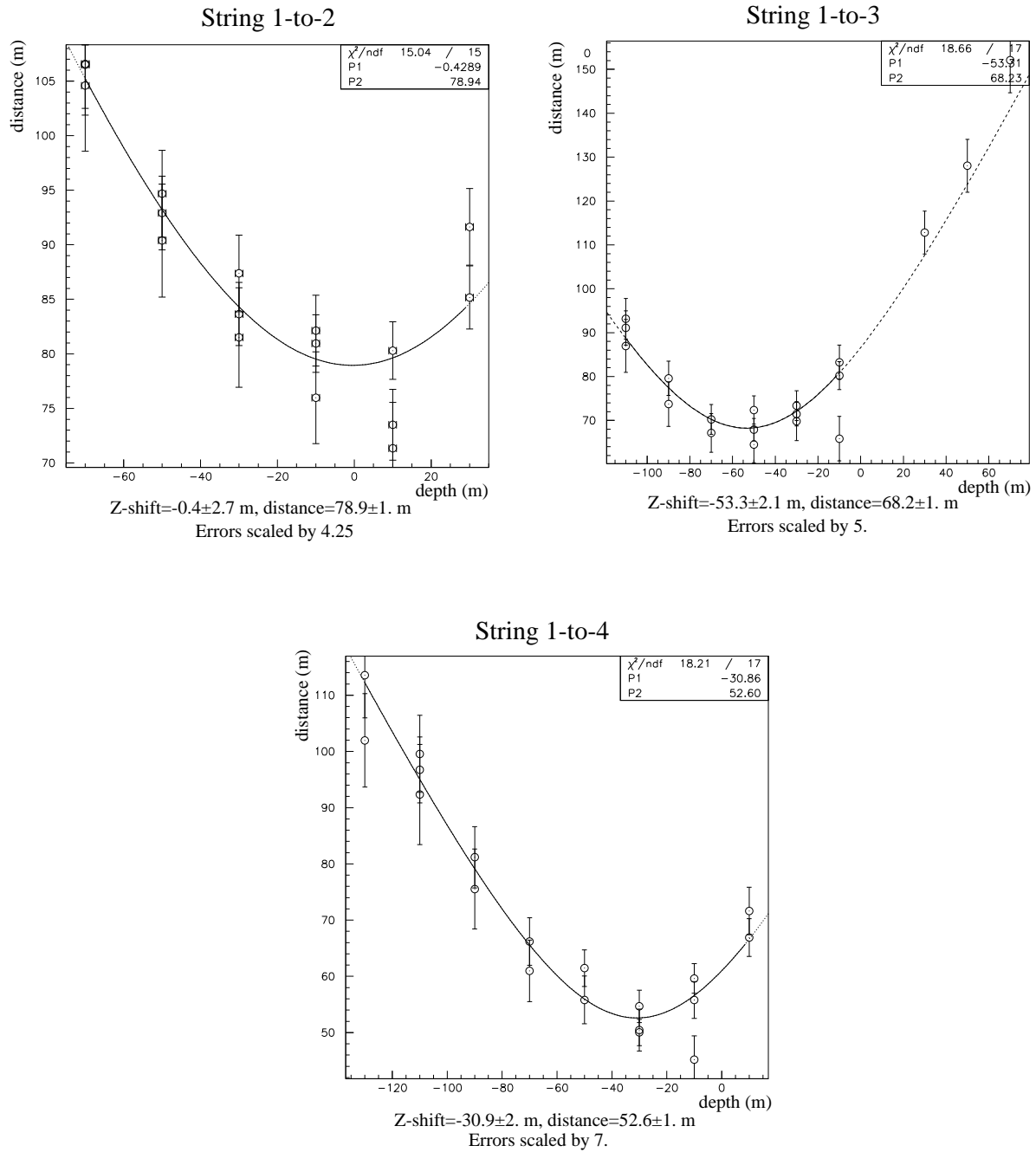


Figure 86: Fit of inter-string distances and depths using laser module data

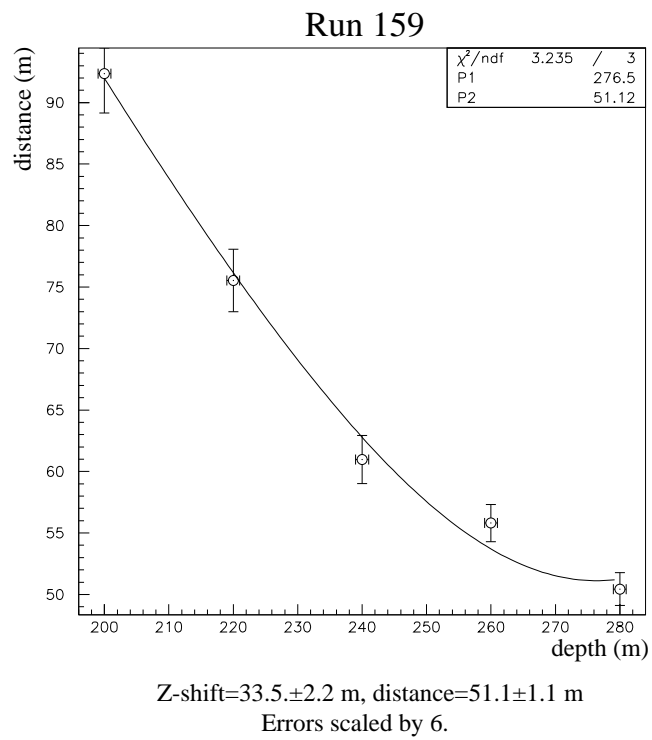


Figure 87: A fit made with all data-points on one side of the valley (laser run 159)

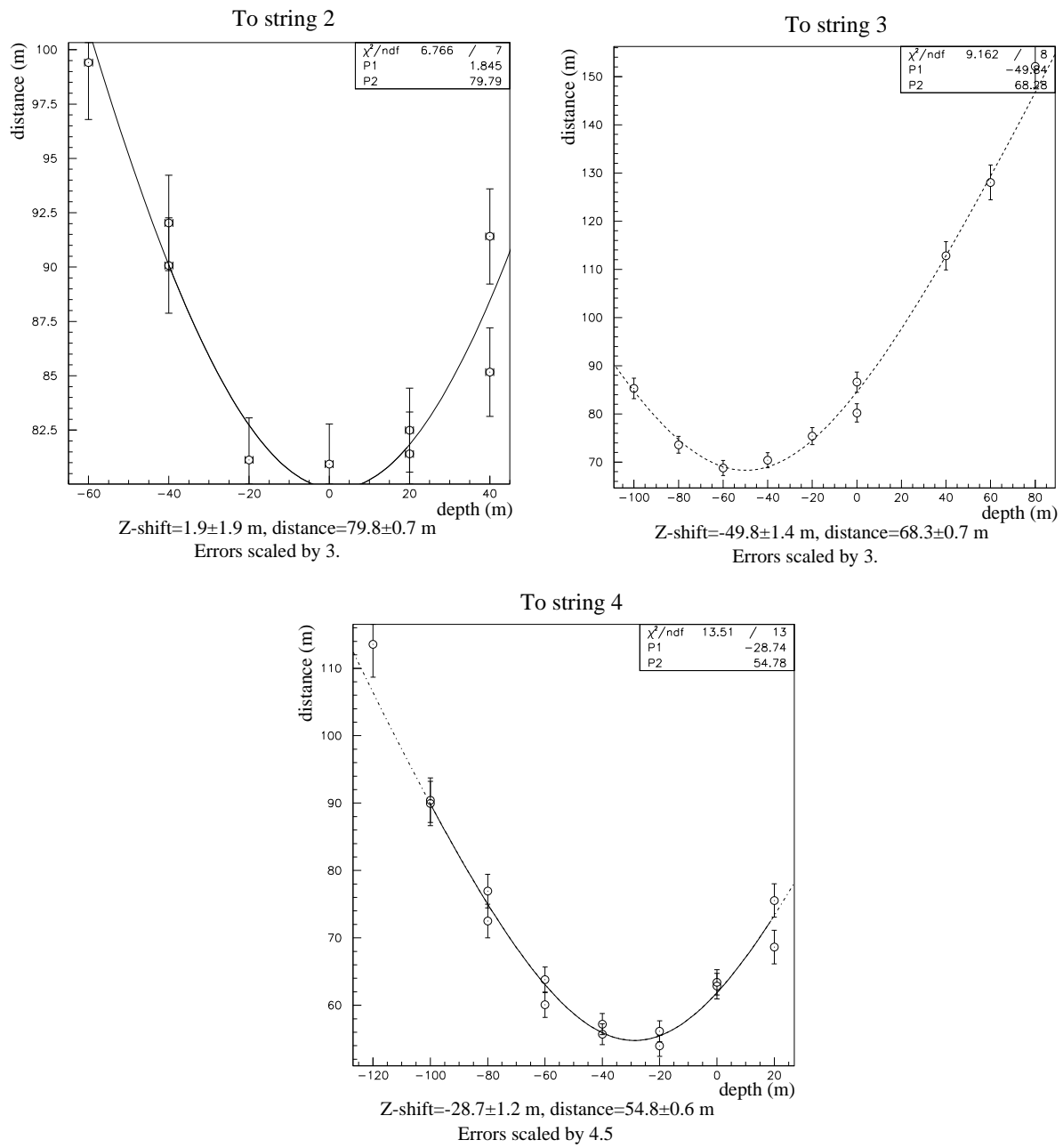


Figure 88: Fit of inter-string distances and depths using YAG data with emitters located in string 1

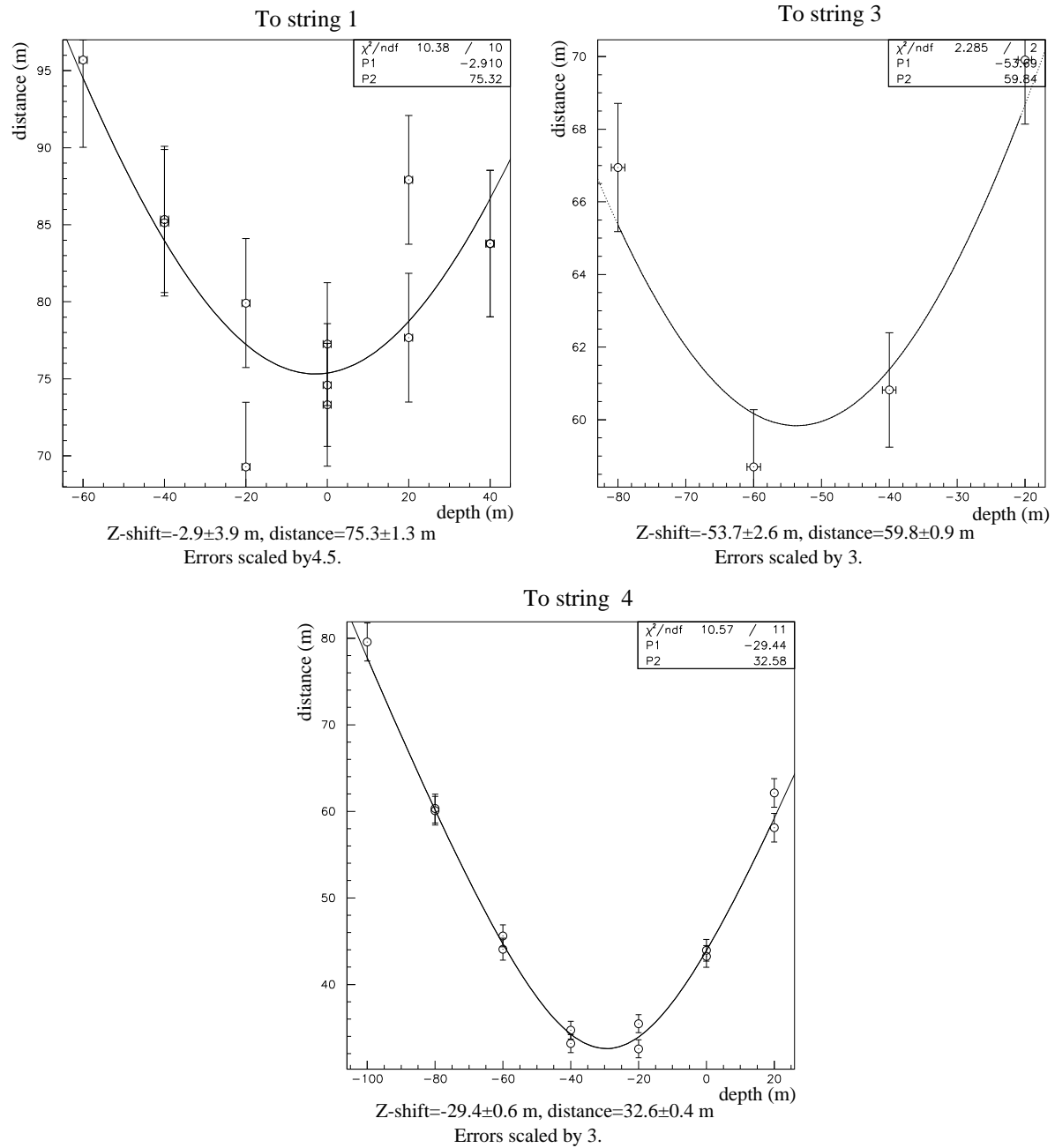


Figure 89: Fit of inter-string distances and depths using YAG data with emitters located in string 2

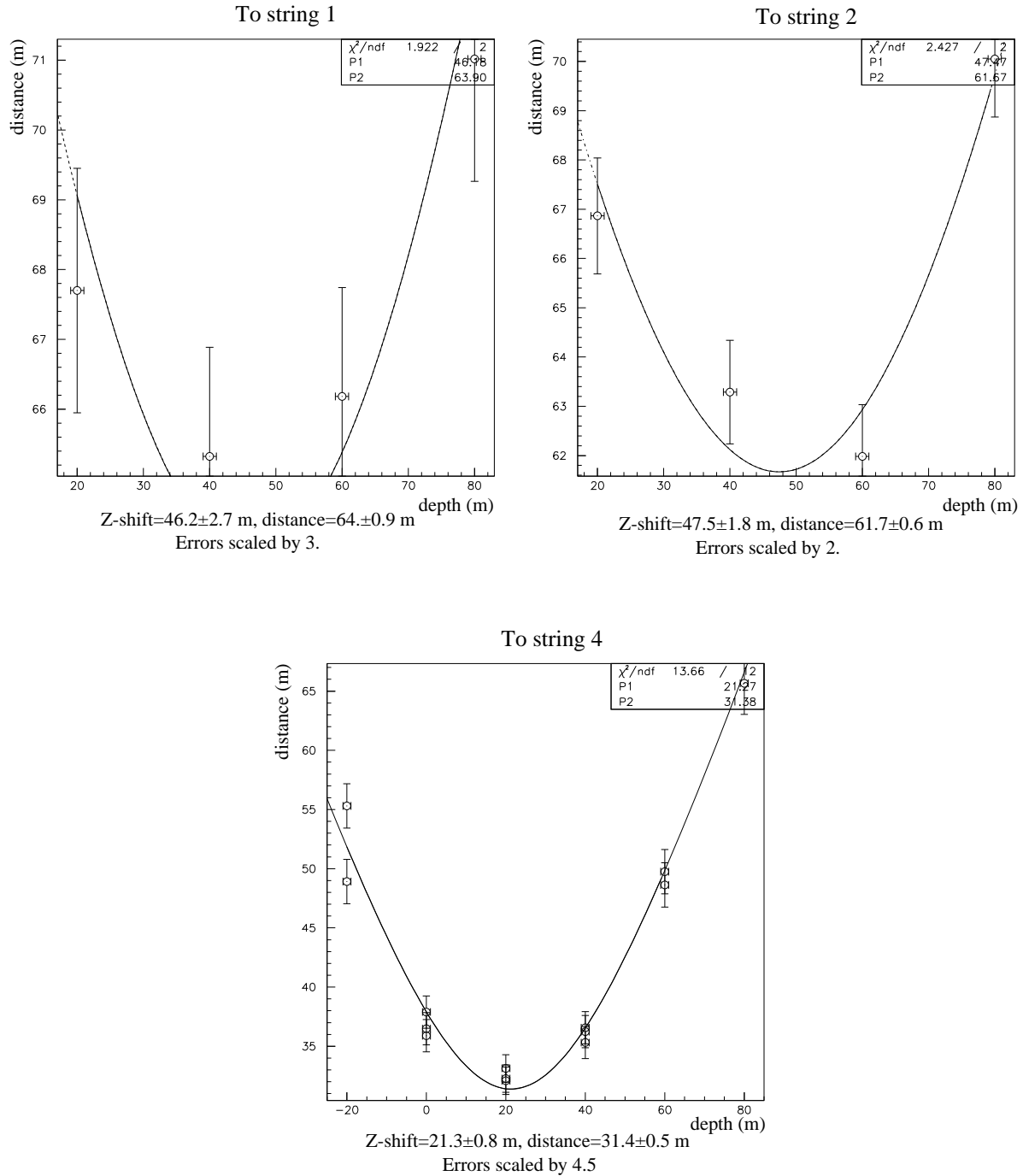


Figure 90: Fit of inter-string distances and depths using YAG data with emitters located in string 3

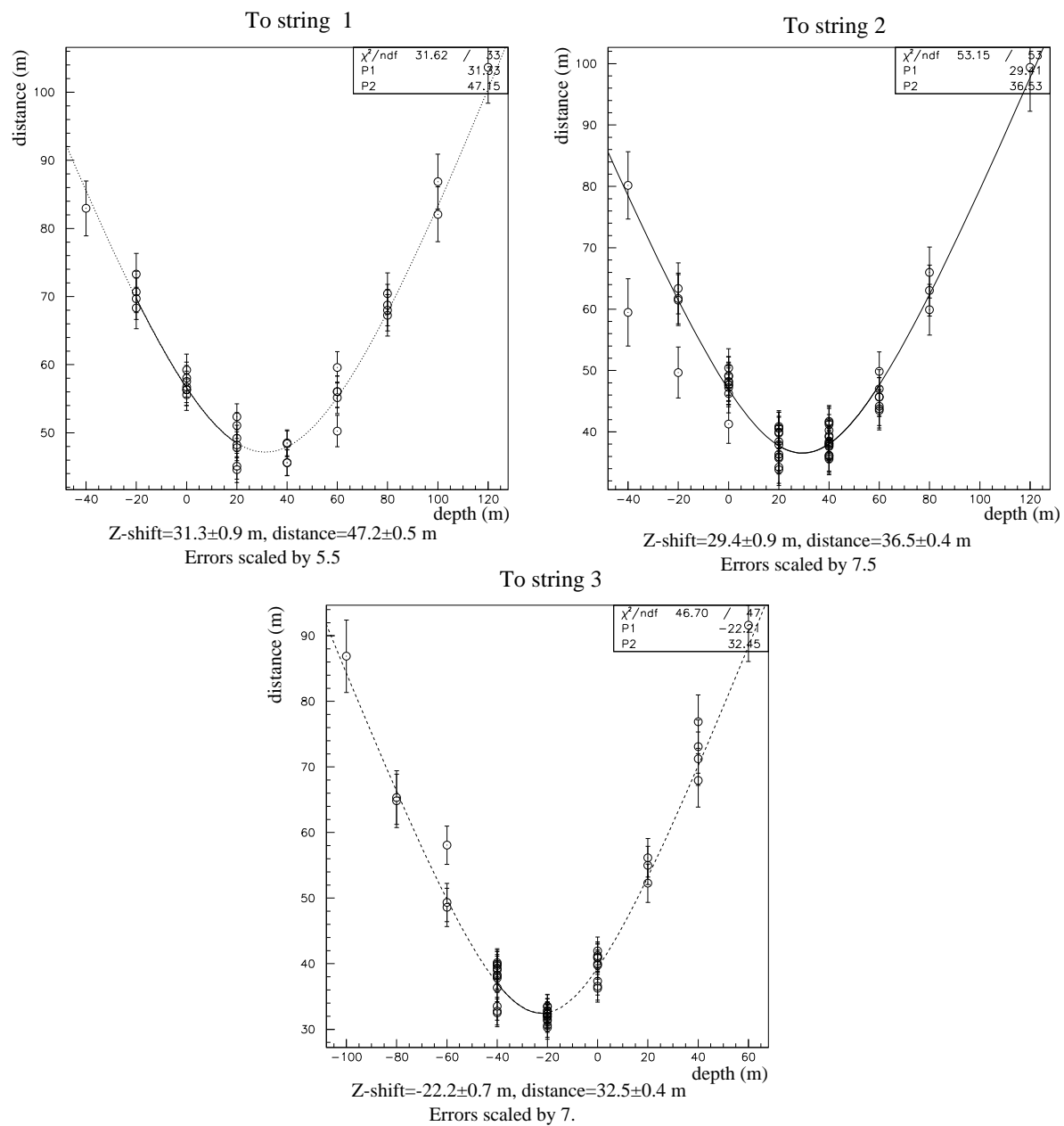
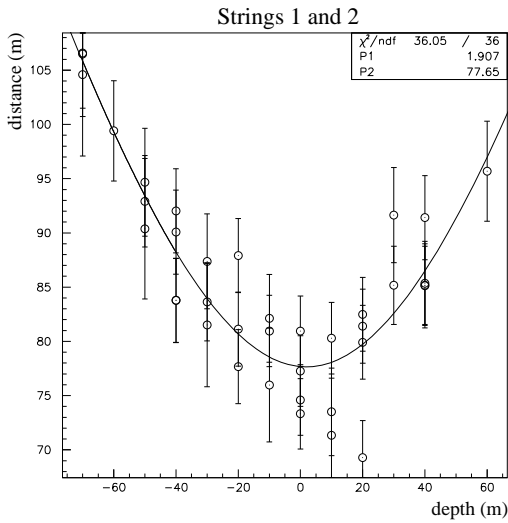
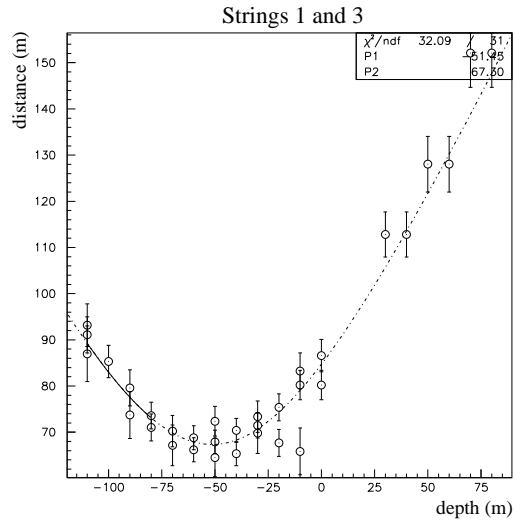


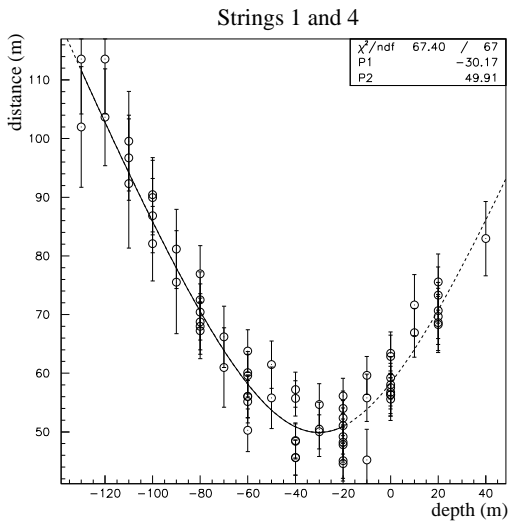
Figure 91: Fit of inter-string distances and depths using YAG data with emitters located in string 4



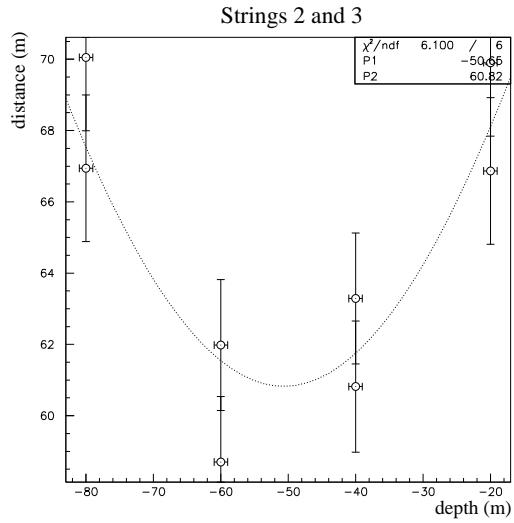
Z-shift= 1.9 ± 1.8 m, distance= 77.6 ± 0.7 m
Errors scaled by 5



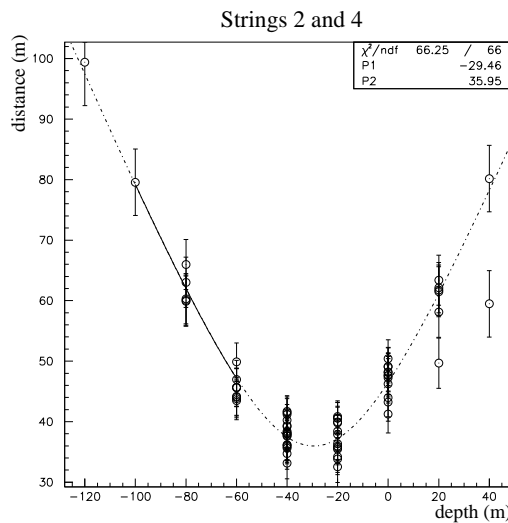
Z-shift= -51.5 ± 1.5 m, distance= 67.3 ± 0.7 m
Errors scaled by 5



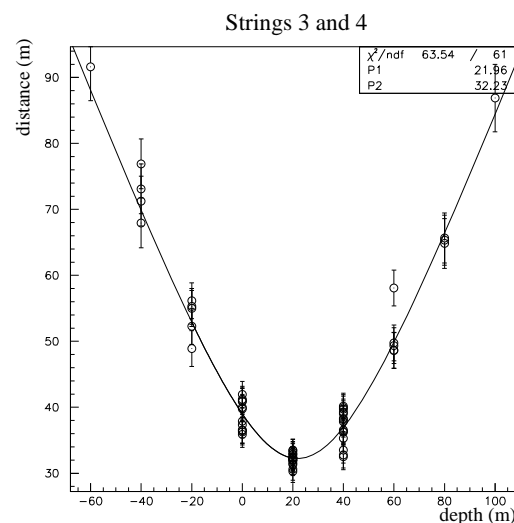
Z-shift= -30.1 ± 1 m, distance= 50 ± 0.5 m
Errors scaled by 8.5



Z-shift= -51 ± 2 m, distance= 61 ± 0.7 m
Errors scaled by 3.5



Z-shift= -29.5 ± 0.8 m, distance= 36 ± 0.4 m
Errors scaled by 7.5



Z-shift= 22 ± 0.6 m, distance= 32.2 ± 0.3 m
Errors scaled by 6.5

Figure 92: Fits made with YAG + laser module measurements gathered

$$\begin{aligned}
\nabla f &= \left[\frac{\partial f}{\partial \eta_1}, \frac{\partial f}{\partial \eta_2}, \frac{\partial f}{\partial \eta_3}, \frac{\partial f}{\partial \eta_4}, \frac{\partial f}{\partial \eta_5}, \frac{\partial f}{\partial \eta_6} \right] = \\
&= \left[\frac{x_4(x_1 - x_2)}{\eta_1^2} - x_3 \left(\frac{\left(\frac{x_1^2}{\eta_1^2} - 2x_1 \right)}{\sqrt{4\eta_1^2\eta_3^2 - x_1^2}} - \frac{\left(\frac{x_2^2}{\eta_1^2} - 2x_2 \right)}{\sqrt{4\eta_1^2\eta_2^2 - x_2^2}} \right), \right. \\
&\quad 2\frac{x_4\eta_2}{\eta_1} + \frac{x_3 \left(4 - \frac{2x_2}{\eta_1^2} \right)}{\sqrt{4 - \frac{x_2^2}{\eta_1^2\eta_2^2}}}, \\
&\quad -2\frac{x_4\eta_3}{\eta_1} - \frac{x_3 \left(4 - \frac{2x_1}{\eta_1^2} \right)}{\sqrt{4 - \frac{x_1^2}{\eta_1^2\eta_2^2}}}, \\
&\quad -\frac{2\eta_4}{\eta_1} \left(x_4 - \frac{x_2x_3}{\sqrt{4\eta_1^2\eta_2^2 - x_2^2}} \right), \\
&\quad \left. \frac{2\eta_5}{\eta_1} \left(x_4 - \frac{x_1x_3}{\sqrt{4\eta_1^2\eta_3^2 - x_1^2}} \right), \right. \\
&\quad \left. 2\eta_6 \right]
\end{aligned}$$

where :

$$x_1 = \eta_1^2 + \eta_3^2 - \eta_5^2$$

$$x_2 = \eta_1^2 + \eta_2^2 - \eta_4^2$$

$$x_3 = \frac{1}{2}\eta_3 \sqrt{4 - \frac{x_1^2}{\eta_1^2\eta_3^2}} - \frac{1}{2}\eta_2 \sqrt{4 - \frac{x_2^2}{\eta_1^2\eta_2^2}}$$

$$x_4 = \frac{x_1 - x_2}{2\eta_1}$$

Figure 93: Constrained fit's equations(contd.)

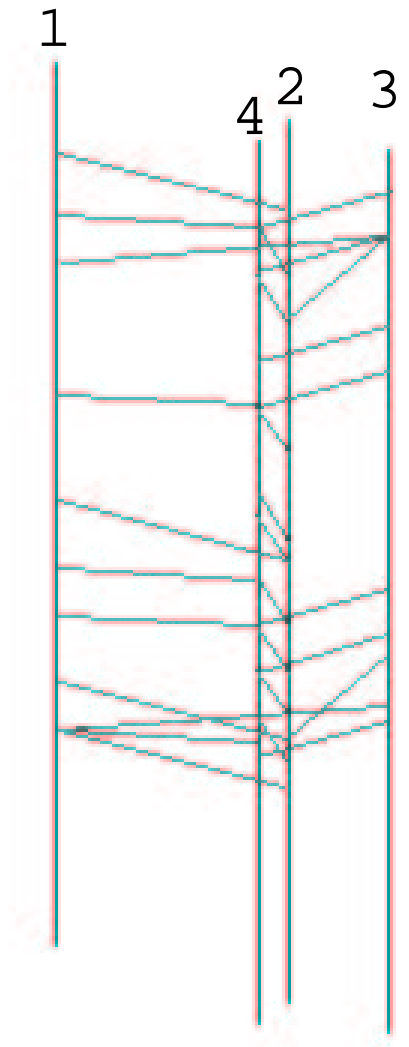


Figure 94: These are the inter-string levels where there is enough data to measure distances

Em. string	Em. module	Rec. string	Rec. module	Distance [m]	Nominal distance [m]
1	16	1	11	95.6	110.0
1	16	1	12	94.2	90.0
1	16	1	13	71.5	70.0
1	16	1	14	43.8	50.0
1	16	1	15	29.8	30.0
1	16	1	20	62.0	70.0
1	16	2	13	104.6	98.9
1	16	2	14	90.4	85.9
1	16	2	15	81.5	76.0
1	16	2	16	76.0	70.6
1	16	2	17	71.4	70.6
1	16	3	11	87.0	84.8
1	16	3	12	73.7	72.1
1	16	3	13	67.2	63.2
1	16	3	14	64.5	59.9
1	16	3	15	69.8	63.2
1	16	3	16	65.8	72.1
1	16	4	11	92.5	89.5
1	16	4	12	75.5	72.1
1	16	4	13	61.0	56.6
1	16	4	14	55.8	44.7
1	16	4	15	50.4	40.0
1	16	4	16	45.2	44.7

Table 23: Corrected measurements for run 159

Em. string	Em. module	Rec. string	Rec. module	Distance [m]	Nominal distance [m]
1	16	1	11	114.1	110.0
1	16	1	12	93.6	90.0
1	16	1	13	70.7	70.0
1	16	1	14	44.5	50.0
1	16	1	15	31.0	30.0
1	16	1	17	11.9	10.0
1	16	1	20	73.8	70.0
1	16	2	13	106.5	98.9
1	16	2	14	94.7	85.9
1	16	2	15	87.4	76.
1	16	2	16	82.1	70.6
1	16	2	17	73.5	70.6
1	16	2	18	91.6	76.0
1	16	3	11	93.2	84.8
1	16	3	12	79.6	72.1
1	16	3	13	70.2	63.2
1	16	3	14	72.4	59.9
1	16	3	15	73.4	63.2
1	16	3	16	83.2	72.1
1	16	4	10	102.0	107.7
1	16	4	11	99.6	89.5
1	16	4	12	81.2	72.1
1	16	4	13	66.2	56.6
1	16	4	14	61.5	44.7
1	16	4	15	54.7	40.0
1	16	4	16	55.8	44.7
1	16	4	17	71.6	56.6

Table 24: Corrected measurements for run 160